SUBJECT-SPECIFIC MODELING IN COMPUTATIONAL CARDIAC ELECTROPHYSIOLOGY

by

Darrell Swenson

A dissertation submitted to the faculty of
The University of Utah
in partial fulfillment of the requirements for the degree of

Doctor of Philosophy

Department of Bioengineering

The University of Utah

August 2013

The University of Utah Graduate School

STATEMENT OF DISSERTATION APPROVAL

The dissertation of Darrell Swenson

has been approved by the following supervisory committee members:

Rob MacLeod, Chair — August 9, 2012
Date Approved

Chris Johnson, Member — July 2, 2012
Date Approved

Ed Hsu, Member — July 2, 2012
Date Approved

Ross Whitaker, Member — July 2, 2012
Date Approved

Sarang Joshi, Member — July 2, 2012
Date Approved

and by Patrick Tresco, Chair of

the Department of Biomedical Engineering

and by Donna M. White, Interim Dean of The Graduate School.

ABSTRACT

Computational simulation has become an indispensable tool in the study of both basic mechanisms and pathophysiology of all forms of cardiac electrical activity. Because the heart is comprised of approximately 4 billion electrically active cells, it is not possible to geometrically model or computationally simulate each individual cell. As a result computational models of the heart are, of necessity, abstractions that approximate electrical behavior at the cell, tissue, and whole body level. The goal of this PhD dissertation was to evaluate several aspects of these abstractions by exploring a set of modeling approaches in the field of cardiac electrophysiology and to develop means to evaluate both the amplitude of these errors from a purely technical perspective as well as the impacts of those errors in terms of physiological parameters.

The first project used subject specific models and experiments with acute myocardial ischemia to show that one common simplification used to model myocardial ischemia—the simplest form of the border zone between healthy and ischemic tissue—was not supported by the experimental results. We propose a alternative approximation of the border zone that better simulates the experimental results.

The second study examined the impact of simplifications in geometric models on simulations of cardiac electrophysiology. Such models consist of a connected mesh of polygonal elements and must often capture complex external and internal boundaries. A conforming mesh contains elements that follow closely the shapes of boundaries; nonconforming meshes fit the boundaries only approximately and are easier to construct but their impact on simulation accuracy has, to our knowledge, remained unknown. We evaluated the impact of this simplification on a set of three different forms of bioelectric field simulations.

The third project evaluated the impact of an additional geometric modeling error; positional uncertainty of the heart in simulations of the ECG. We applied a relatively novel and highly efficient statistical approach, the *generalized Polynomial Chaos-Stochastic Collocation method* (gPC-SC), to a boundary element formulation of the electrocardiographic forward problem to carry out the necessary comprehensive sensitivity analysis. We found variations large enough to mask or to mimic signs of ischemia in the ECG.

For my family.

CONTENTS

CHAPTERS

LIST OF TABLES

LIST OF FIGURES

ACKNOWLEDGEMENTS

I would like to thank all those who have assisted me in this work, in particular my advisor Rob MacLeod. He has provided excellent mentorship and opportunities for me to grow. Not only has he provided technical guidance for my many projects, but he has helped me grow as a teacher, writer, presenter, leader, and in numerous other ways. To him I offer my sincere thanks. In addition, the students and post docs in our research lab, Josh Blauer, Jess Tate, Brett Burton, Kedar Aras, and Jeroen Stinstra have been enormously generous with their time to advise and share technical expertise, for which I am very grateful.

In addition I would like to thank the professors who have served on my PhD. committee: Dr. MacLeod, Dr. Whitaker, Dr. Johnson, Dr. Joshi, and Dr. Hsu. They have provided excellent guidance and suggestions for this work. Also, the staff and resources of the Scientific Computing and Imaging Institute have been absolutely necessary to carry out computational studies of this type. In particular I would like to thank Ayla Kahn, Tom Fogal, Ross Whitaker, and Chris Johnson as members of the CIBC, who have helped design and support software used in this work.

This work would not be possible without the expert assistance of several other groups. I would like to thank the staff at CVRTI (Jayne Davis, Nancy Allen, Alicja Booth, Bruce Steadman, Phil Ershler) who were instrumental in the experimental ischemia studies. In addition, we relied heavily on the expertise of the Small Animal Scanning Group (Ed Hsu, Lindsey Healy, Osama Abdullah) for our CT, MRI, and DTI scans. Thanks also to Mike Kirby and Sarah Geneser for their assistance learning and utilizing the gPC-SC method.

Most importantly, I would like to thank my family, especially my wife Ashley, for their patient support and constant encouragement.

CHAPTER 1

INTRODUCTION

One of the fundamental goals of science and engineering is to understand the behavior of complex systems well enough that one can capture it in a quantitative model that replicates known behaviors and ideally even predicts unknown behaviors. Economists try (largely unsuccessfully) to predict changes to the world's markets, climatologists try to predict the effects of pollutants on climate, and engineers try to predict how a new part or design will perform before it is manufactured. These models allow us to optimize a process so that it can improve the final outcome. One example of the highly successful use of simulation in biomedicine is the Nobel Prize winning research of Hodgkin and Huxley, who developed a numerical model that encompassed a newfound understanding of the mechanisms of the action potential in neurons [1, 2, 3]. The fact that this model generated realistic action potentials that responded with fidelity to changes in parameters, *e.g.,* variations in ion concentrations, achieved more than to validate the numerical accuracy of the model. It provided supporting evidence for the qualitative assumptions of the then unknown structure of ion channels that were the real intellectual contribution of these investigators. Subsequent breakthroughs in measurement were required to provide the complete proof for these ideas [4].

The medical field employs its own form of modeling; physicians want to predict the impact of a procedure before administering it to a patient. The basis for such modeling and predictions are statistical models derived from clinical trials combined with personal experience to select the cure that has the best chance of succeeding for each individual patient. In recent years a new idea of what has become known as "personalized medicine" has emerged, in which the prevention, diagnosis, and treatment of disease are customized to individual genes, proteins, cellular environment, or tissue structure. Rather than grouping patients into categories in order to determine the correct procedure, personalized medicine customizes the procedure for the individual. One emerging branch of personalized medicine, and the overall context of this dissertation, uses a traditional engineering approach of computational modeling to customize medical diagnosis and treatment for an individual.

The result, known as "patient specific modeling" or, more generally, as "subject specific modeling," represents a powerful convergence of engineering technology, physiology, and medical information. This dissertation represents an example of this convergence as it applies to the specific field of cardiac electrophysiology.

While such patient specific models have great potential to improve medical care, their use in clinical settings is still emerging. It remains technically challenging and time consuming to create precise, subject specific models and they often still lack the accuracy and/or validation to be trusted in critical situations. While, at least from an engineering perspective, it seems that improving simulation accuracy and decreasing construction and simulation times are at odds with one another, one of our goals has been to propose technical solutions that can achieve both objectives. Thus, this dissertation focuses on using subject specific models to answer clinically compelling questions about cardiac electrophysiology in a computationally efficient and practical manner.

There is also a larger technical context for this specific application of subject specific modeling. It represents an example of the broader topic of image based computational modeling and simulation, which has spawned its own generalized technical framework and an associated set of computational tools. One novel initiate, known as the "Physiome," seeks through international collaborations to create a framework for multiscale and multiphysics models of the entire organism[5, 6, 7, 8]. Our specific, medical goals from cardiac bioelectricity will both benefit from access to these broader algorithms and tools, just as they will also hopefully contribute to this larger initiative and motivate new developments that are of general utility.

1.1 Background

Cardiovascular disease is the leading cause of death in the world accounting for 31.5% of all deaths in women and 26.8% in men [9]. While the heart is a mechanical pump, its ultimate failure, both acutely and in the final phases of prolonged disease, is most frequently caused by problems in electrical conduction. Over the last 50 years, enormous investments in research have resulted in dramatic advancements in understanding the electrical currents and potentials that control the heart and its behavior. Researchers such as Hodgkins and Huxley pioneered the field of cellular electrophysiology of the nervous system using the giant squid to study the flow of ions in and out of cells [1]. Out of their Nobel Prize winning insights has come a formalism still used today, to describe mechanistically and to simulate numerically the biophysics of ion channels and cells across all the electrically active organs of the body. While a great deal is known about the cell and even cell-to-cell interactions in the heart, many of the mechanistic explanations of whole-heart behavior such as electrical conduction abnormalities, clinically known as “arrhythmias,” remain controversial or unknown. Such whole-heart electrical conduction disorders are difficult to study experimentally because they are complex, containing a large number of uncontrolled parameters that act simultaneously and heterogeneously over a three-dimensional structure that changes electrically and mechanically over several different time scales. To capture this complexity, many researchers are turning to computational models to assist in understanding the basic mechanisms of heart pathologies. These models not only answer fundamental questions about cardiovascular disease, but have potential to be used as a diagnostic or procedure planning tool in clinical settings.

The primary goal of this dissertation is to better understand the application, utility, and limitations of computational modeling in the specific setting of subject specific, whole organ and whole organism cardiac electrophysiology. Some of the approaches have even broader utility as they relate to simulations based on subject specific anatomical models using fairly common numerical methods for solving partial differential equations. Overall, this study fits into a context of generalized image based modeling and multiscale simulation. Such computational models are deterministic, that is, they can provide a very subject and situation specific basis for interpretation of clinical signals and parameters that originates in explicit mechanisms rather than statistical correlations. Other benefits of computational modeling and simulation include their ability to explore scenarios noninvasively with complete control of all included parameters, and to integrate levels of structural and physiological complexity that are beyond the unaided ability of any single person or even single laboratory [10, 11, 12].

The technical requirements for useful computational models can prove a daunting obstacle, especially in the clinical setting. The creation of such models is very labor intensive and requires a unique skill set that is not always available in a biomedical research or clinical setting. In many instances, the time it takes to create and execute a model is too long for realistic use as a diagnostic tool. Also, computational models often rely on detailed and subject-specific mathematical descriptions of anatomy and tissue properties that may be difficult or impossible to obtain, especially in a clinical setting, thus necessitating very broad approximations. The resulting inaccuracies may reduce the quality of the simulation results to the point that the simulation is no longer useful as a clinical tool.

However, recent technical and computational advances are now enabling new progress in automating and accelerating the modeling and simulation of patient specific data. In the context of modeling the heart, advances in medical imaging, image processing, geometric mesh generation, and computational acceleration have led to image based modeling techniques that support the creation of highly detailed subject-specific and physiologically accurate models that can be compared directly to experimental results [10, 12, 11, 13]. While the complete capabilities to carry out such computational studies exist only in a relatively small number of laboratories, several groups, including ours, have made progress in making the programs, data, and knowledge available to others [14, 15, 13, 16, 17, 18, 19, 20], thus increasing the opportunities for validation and use of these approaches to broad areas of biomedicine.

The research in this thesis consists of a series of projects seeking to advance the state of image based modeling in cardiac electrophysiology by taking advantage of both recent breakthroughs in computational science and access to unique validation data specific to myocardial ischemia. We have compared our subject specific simulations directly to experimental data. Such comparisons allowed us to refine physiological assumptions about the underlying pathology, evaluate the appropriateness of geometric modeling simplifications, and explore stochastic approaches to account for parameters that are not available in clinical settings. The focus of the applications of this simulations research has been on early stages of myocardial ischemia, which is a reflection of both availability of highly detailed data from experiments and the importance of this pathophysiology in medicine, which is described in detail in Chapter 2. The study of myocardial ischemia is also well matched to simulation across scales because it has cellular and even subcellular origins whose consequences alter whole-heart behavior and are reflected in electrical signals acquired from the body surface.

Out of this intersection of mathematical, computational, physiological, and medical domains, we have pursued three specific aims, each of which has advanced the state of knowledge and contributed to both technical and biomedical science.

Aim 1: The first aim of this research was specific to the challenges of modeling myocardial ischemia at the scale of the whole heart. Such models are multiscale in that they must include aspects of cellular and tissue electrophysiology and pathophysiology but must also approximate and simplify their details in order to achieve a tractable formulation at the level of the whole heart. It is obviously not feasible to carry out simulations in subject specific geometric models of the heart and torso by combining a cellular model for every cell in the relevant organs of the body. The general approach to such multiscale modeling is then to find approximations for each scale of behavior that capture the details and the key control parameters of the finer level scale below. Thus our first specific aim was to identify viable and acceptably accurate approximations of the bioelectric fields that arise in the heart during acute myocardial ischemia and thus provide an organ scale model of a behavior that has already been the topic of intense scrutiny at the cellular and subcellular scales. The approach of most previous models of ischemia has been to alter concentrations of ions based on experimental observations [21, 22] and then generate abnormal action potentials from cardiac membrane models [23, 24]. Our previous approach has been to simplify the bioelectric sources during ischemia into a border zone between healthy and ischemic tissues in which the sources reside [25, 26]. In this study, we set out to examine those assumptions using both more detailed simulations than would be clinically useful as well as direct measurements from ischemic hearts.

Our findings suggest that the modeling assumptions about the ischemic border zones used in many previous studies are overly simplified and that they do not reproduce key features of the electric potentials that we were able to measure in the heart. We also suggest new approximations of the border zone that produce more accurate simulation results and that are supported by experiment data.

Aim 2: The second aim of this thesis was to address another assumption of the typical computer simulations of ischemia and other electrophysiological behaviors—the formulation of the polygonal meshes used to carry out the simulations. Simulations of realistic tissue include not only assumptions about the electrophysiology but also about the anatomy (or geometry in the technical context). In particular, most heart models contain multiple regions of different tissue types or tissues in different states, *e.g.,* ischemic versus healthy. The precise shape of the interfaces between these regions can be very difficult to capture in a geometric model even when they are known from imaging. In many cases, researchers create polygonal mesh models that only approximate the boundaries instead of fitting them to any level of detail. To evaluate the consequences of such simplifications, we compared the impact of meshing algorithms on several different settings of modeling cardiac electrophysiology.

The main finding of this study was that geometric approximations that resulted in jagged, inaccurate surfaces between materials generated errors large enough to change the simulation results and their physiological interpretation. By comparison, meshes that followed actual boundaries more precisely, “boundary conforming,” produced more accurate results at much lower resolution than the non-boundary conforming meshes.

Aim 3: The third and final aim of this thesis was to evaluate the role of coarse scale geometric error on the projection of electrical currents from the heart onto the body surface. With change in posture, the heart can shift, rotate, and swing in a variety of directions within the thorax. The consequences of such changes in position of the heart on the electrocardiogram have been observed [27, 28] but never comprehensively quantified, a task well suited to simulation approaches. The goal of Aim 3 was thus to quantify the sensitivity of body surface potentials to realistic heart motion for which we used stochastic methods.

The findings from this study confirmed that heart motion due to changes in posture or respiration can be large enough to mask and mimic myocardial ischemia as detected from the body surface. It also indicated types of motion that are not likely to be significant sources of error in the ECG recordings. One practical consequence of these findings is that the statistical approaches provide a means of creating compensatory algorithms to remove the errors due only to heart and body position from the interpretation of ECGs.

In summary, the three aims of this dissertation were to:

1. Evaluate the current approximation of transmembrane potentials of acute myocardial ischemia used in static bidomain simulations specifically the configuration of the ischemic border zone between healthy and ischemic myocardium.
2. Quantify the magnitude of errors introduced into cardiac bioelectric models using nonboundary conforming meshes to represent diseased regions of the heart.
3. Statistically quantify the effect of natural variations in heart position on the electrocardiographic forward problems providing clinically relevant statistics about the effect of heart position on ECG recordings.

All these aims share the common goal of improving subject specific modeling, particularly in the case of myocardial ischemia. The results and conclusions serve to explore the accuracy—both physiologically and computationally—of the fundamental understanding of the electrical consequences of myocardial ischemia and they also expand the general framework needed to incorporate unknown parameters that are commonly found in clinical settings of image based analysis. While there are always many more details to validate and explore, these findings provide an important step towards establishing the feasibility and reliability of clinically relevant, patient specific simulations.

1.2 Organization of the Dissertation

This dissertation is broken into seven chapters. Chapter 2 summarizes the background electrophysiology and computational methods necessary to appreciate the subsequent chapters. Chapter 3 provides an overview of the image based modeling pipeline from a general context, but also offers some insights into specific challenges unique to cardiac modeling. Chapter 4 is a journal paper in preparation for the Journal of Cardiac Electrophysiology that deals with the electrical border zone assumption between ischemic and nonischemic tissue. Chapter 5 is a paper at the International Meshing Roundtable 2013 that deals with boundary conforming meshes in computational electrophysiology simulations. Chapter 6 is a reprint of a published paper in the Annals of Biomedical Engineering [29]. It deals with using the general Polynomial Chaos Stochastic Collocation (gPC-SC) method to quantify the effects of heart motion on the detection of myocardial ischemia with ECG. Chapter 7 concludes the manuscript by discussing the implications of the results presented and outlining future directions for this research.

CHAPTER 2

CARDIAC ELECTROPHYSIOLOGY OVERVIEW

The heart is a pump that moves blood throughout the body in order to deliver oxygen and nutrients to all of the living tissues and remove metabolic waste products. However, the heart also depends on electrical conduction to stimulate and coordinate the contraction of the myocardium (heart muscle). To understand the complex electrical activity of the heart, excitation and conduction mechanisms must be evaluated at multiple scales: cellular, tissue, and whole body.

2.1 Cellular Electrophysiology

Within the body there are two types of electrical conduction, passive and active. Passive conduction of electrical currents arises when ions flow throughout the tissues of the body. In contrast, some cells such as neurons and muscle cells are considered active electrical conductors, *i.e.,* they are capable of generating currents and maintaining electric potentials at the cost of metabolic energy. The source of electrical currents within the tissues is ions, typically potassium (K^+), calcium (Ca^{2+}), sodium (Na^+), and chloride (Cl^-), rather than the electrons that flow in other conductors [30]. The driving force for the flow of ions across the membranes of active cells is the potential difference between the intracellular to extracellular spaces, known as the "transmembrane potential," which is primarily controlled by the concentration gradients of ions and the conductivity of the cell membrane [31]. Because active conduction through cardiac muscle tissue (myocardium) is the mechanism that controls both normal heart behavior and is involved in virtually all cardiac pathologies, the following discussion will focus on the basic mechanisms that control this process.

2.1.1 Cell Membranes

The cell membrane (sarcolemma) of a cardiac myocyte is mainly comprised of phospholipids, cholesterol, glycolipids, and membrane proteins. However, for the basic understanding of conduction only the phospholipids and membrane proteins are necessary. The cell membrane separates the cell interior from the extracellular fluid with a phospholipid bilayer, *i.e.,* a double layer of molecules. Phospholipids are a molecule comprised of a hydrophilic head group and a hydrophobic tail group. As a result of these different levels of attraction to water, hydrophilic head groups point towards the aqueous solution, intracellular and extracellular, while the lipid tails assemble in the middle of the membrane away from the aqueous solutions. The resulting bilayer forms a film around the cell preventing molecules such as water and ions from entering or leaving the cell. Ions and certain small molecules can, however, cross the membrane through specialized proteins that are embedded throughout the bilayer. These proteins span the membrane and contain small pore-like structures that are known as “ion channels” and function as highly selective gates as seen in Figure 2.1 that can regulate the exchange of molecules in and out of the cell [32]. Ion channels are not the only proteins embedded in the cell membrane and other types can form energy consuming pumps, ion exchangers, and co-transporters, each with their own selectivity and regulatory behavior.

Ion channels open in complex voltage, time, and chemically gated manners to allow specific ions to cross the cell membrane, *i.e.,* they are typically highly selective and also highly sensitive to local conditions. However, they do not provide or consume energy and rely upon electrical or chemical gradients to move the ions. The specialized membrane proteins provide for the complex maintenance of ion concentrations and for the movement of ions that generates active electrical currents. Ion pumps, in contrast, consume energy from adenosine triphosphate (ATP) to move ions across the membrane even against electrical

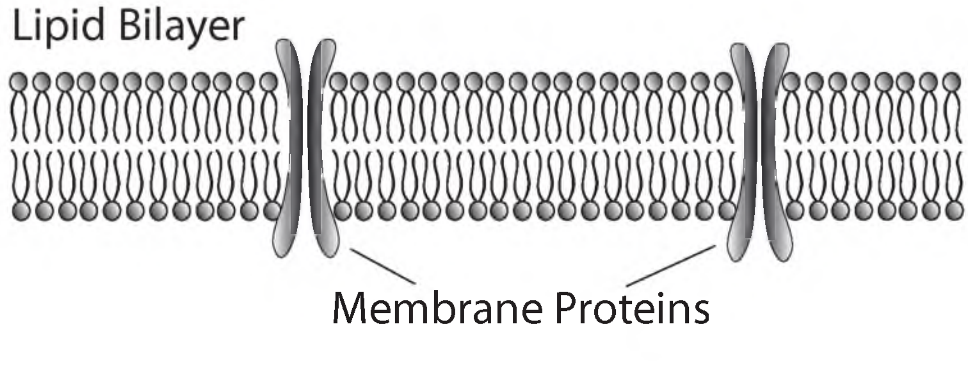

Figure 2.1: Lipid bilayer with membrane proteins. This figure illustrates the lipid bilayer formed by the phospholipids in which the hydrophobic tail groups are insulated against the aqueous solution. Specialized membrane proteins embedded in the membrane act as the means of transporting ions and small molecules across the membrane.

or chemical gradients. Ion exchangers move one type of ion in or out of the cell with minimal or no direct ATP consumption by utilizing the exchange of a second ion type that has a favorable electrochemical gradient [33]. Ion pumps and exchangers are critical to active conduction because they maintain the concentration gradients of Na^+, Ca^{2+}, and K^+ across the cell membrane which are necessary to produce action potentials.

A central concept in the electrophysiology of the cell is the overall driving force that each ion experiences when the associated ion channel is open. This driving force stems from the selective permeability of the membrane; under quiescent conditions, the cell membrane is relatively highly permeable to potassium ions (K^+) compared to all other ions. These ions seek an equilibrium in which differences in their concentration are perfectly balanced by an electric potential difference so that there is no net flow of ions. At equilibrium, the chemical and electrical gradients are balanced and there is no net driving force. The value of the associated electric potential is known as the Nernst potential [34] as follows:

$$\Phi_k = \Phi_i - \Phi_e = -\frac{RT}{z_k F} ln \frac{[k]_i}{[k]_e}, \tag{2.1}$$

where k is the ion type, the $[k]$'s are the concentrations of this ion, Φ is the electric potential, and the subscripts specify intracellular or extracellular. R is the gas constant, T is the absolute temperature, F is Faraday's constant, and z_k is valence.

As the subscript k in Equation 2.1 suggests, the Nernst potential for each ion depends solely on that concentration gradient of that ion. The driving force felt by an ion therefore depends on the difference between the prevailing transmembrane potential, which is the same for all ions, and the respective Nernst (or equilibrium) potential for each ion species. When for any ion, the membrane potential Φ_m diverges from the Nernst potential, there is a driving force expressed by the equation

$$\Phi_{Dk} = (\Phi_M - \Phi_k), \tag{2.2}$$

where Φ_{Dk} is the driving force on an ion of type k and Φ_M is the membrane potential.

Under physiological conditions, concentrations of different ions are regulated at levels that result in a range of quite divergent equilibrium potentials. The actual resting potential of a cell then becomes a function of the concentrations of all the charged ions weighted by their respective permeabilities, a relationship described by the Goldman-Hodgkin-Katz equation:

$$E = \frac{RT}{F} \ln \frac{P_{Na}[Na]_0 + P_{Ca^{2+}}[Ca^{2+}]_0 + P_K[K]_0 + P_{Cl}[Cl]_i}{P_{Na}[Na]_i + P_{Ca^{2+}}[Ca^{2+}]_i + P_K[K]_i + P_{Cl}[Cl]_o} \tag{2.3}$$

where the P's are the permeabilities of the different ions indicated by the subscript. For mammalian cardiac cells, intracellular K^+ is high and Na^+ and Ca^{2+} are low (In the case of Ca^{2+}, three orders of magnitude lower!) compared to their extracellular values and the resulting resting transmembrane potential is approximately -80 mV. At this resting membrane potential, thus any opening of ion channels will change the permeability of the membrane and allow ions to flow according to their respective driving forces.

2.1.2 Action Potentials

When the membrane potential of a cell depolarizes (becomes less negative) to the point of exceeding a threshold, the result is a complex sequence of ion channel openings and closings that results in what is known as an "action potential." An action potential is the behavior of a cell that characterizes it as an active generator. It consists of both a depolarization phase, increasing transmembrane potential, and repolarization phase, transmembrane potential returning to a resting state. An action potential is elicited when the cell is stimulated—typically from adjacent, already depolarized cells—and the resting membrane potential becomes more positive than an ion-channel specific threshold, opening voltage gated ion channels, first the Na^+ and then Ca^{2+} [35, 36]. This sequence of openings results in a rapid influx of positively charged ions into the cell, leading to further depolarization in a positive feedback action. The end of this positive feedback occurs when, after a few milliseconds, Na^+ channels quickly inactivate and K^+ channels open, which results in the flow of K^+ out of the cell, balancing the effect of the ongoing influx of Ca^{2+} to produce a relatively stable "plateau" phase of the action potential. Eventually the Ca^{2+} current also inactivates and is overwhelmed by the K^+ currents, thus restoring the membrane potential. The active ion pumps and exchangers then work to return the Na^+, Ca^{2+}, and K^+ concentrations to their original states. A typical cardiac action potential is illustrated in Figure 2.2.

2.1.3 Tissue Electrophysiology

At the tissue level, electrical activation spreads across the myocardium like a wave. The mechanisms that control the spread of this activation wave are tied to the electrical properties of the underlying myocytes and their electrical connectivities. When healthy and fully recovered from a previous excitation, each myocyte in the heart is capable of producing an action potential when stimulated. An excited myocyte provides the stimulus for neighboring myocytes, causing a chain reaction of activation from one myocyte to the next. This cell to cell stimulation is possible due to the fact that the intracellular space of a myocyte is connected to the intracellular space of neighboring myocytes through highly conductive membrane proteins called gap junctions [37, 34]. When a single cell is stimulated,

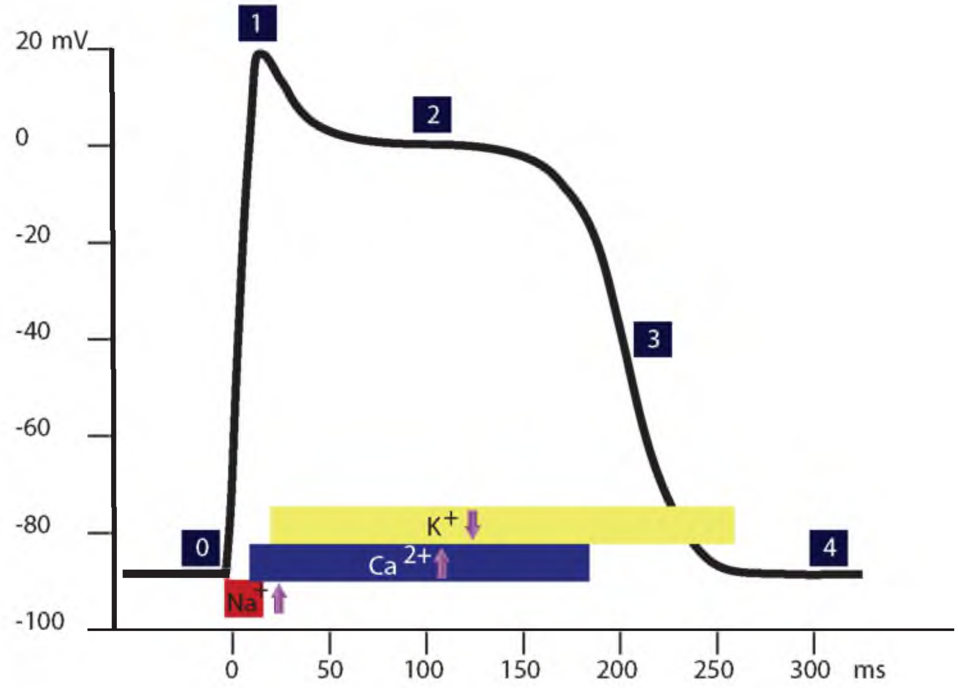

Figure 2.2: The schematic representation of the action potential produced by a human cardiac myocyte. The figure shows the traditional shape and duration of an action potential along with an indication of the ionic currents that contribute to the depolarization and repolarization of the cell. In addition, the phases of the action potential are indicated by the numbers in the black boxes.

ions rush into that cell, elevating the intracellular potential. At the same time, some of the positively charged ions will flow across gap junctions into unstimulated cells that are at lower intracellular potentials. This movement of charge increases the transmembrane potential of neighboring cells causing them to excite and produce their own action potentials. The myocytes remain activated until repolarization occurs. The cells are not able to be stimulated again over a short period of time known as the refractory period during which the ion channels and concentrations return to their resting states.

Tissue structure and the shape of the individual cardiac myocytes play an important role in the electrical conduction of the heart. Myocytes are elongated brick shaped cells that connect end to end with other myocytes via gap junctions [37], creating functional fibers composed of cells with similar orientation. Because of this structure, the intracellular conductivity along the myocyte, or fiber, is much larger than transverse to the fiber direction. This anisotropy of conductivity is also present in the extracellular space but to a lesser extent. The net result for cardiac tissue is highly anisotropic spread of activation, with higher propagation speeds along the fiber direction than across it [38].

2.2 Whole Heart Electrophysiology and the ECG

The properties outlined above describe the behavior of myocardium throughout the heart. However, they do not explain the initiation of the heart beat nor the fine control of timing and synchronization that results in forceful expulsion of blood. The initial stimulus for excitation in the heart comes from specialized autorythmic or pacemaker cells that periodically produce action potentials without external stimulation. Additional specialized cells, known collectively as the “conduction system,” are responsible for the subsequent timing and synchrony of the spread of excitation through the heart. Summarized, these specialized conduction fibers distribute excitation first through the atria, then through the atrio-ventricular (AV) node, with some delay, to the ventricles. The Purkinje network of very rapidly conducting fibers then spreads excitation along much of the septum that separates the left and right ventricles to the lower tip (apex) of the heart. As a result of the actions of the conduction system, excitation of the working ventricles occurs over a relatively short time, passing from the apex toward the base of the heart and from the endocardial (inner) to the epicardial (outer) surfaces of the ventricles. A more detailed description can be found elsewhere [39, 30, 34].

The electrical conduction in the whole heart can be sensed on the body surface in the form of the electrocardiogram (ECG). The electrical currents generated in the extracellular space of the heart conduct passively through the tissues in the torso until they reach the body surface, producing an attenuated and spatially averaged distribution of potentials. A schematic of one cardiac cycle of an idealized ECG is shown in Figure 2.3, in which each distinct waveform is labeled as P, Q, R, S, or T. Each waveform relates to the activation or repolarization of some part of the heart. The P wave is caused by the spreading activation over the atria, while the Q, R, and S waves are caused by the activation of the ventricles. The T wave is a result of the repolarization of the ventricles [30].

The information contained in the waveforms of an ECG makes it a valuable and extremely widespread tool for clinicians to diagnose electrical conduction problems in the heart. However, while the ECG is inexpensive and noninvasive, its diagnostic utility varies dramatically for different abnormalities. In particular, the diagnosis of early cardiac ischemia is challenging because the resulting changes in the ECG can be very subtle. Moreover, the same changes may also arise from both serious maladies and harmless irregularities,*i.e.,* specificity of diagnosis can be limited. A further source of uncertainty are the recent findings from our group and others suggesting that many previous mechanistic assumptions are incomplete or incorrect [40, 41, 42, 43]. This persistent uncertainty of ECG based diagnosis and the enormous clinical impact of myocardial ischemia (the physiology of

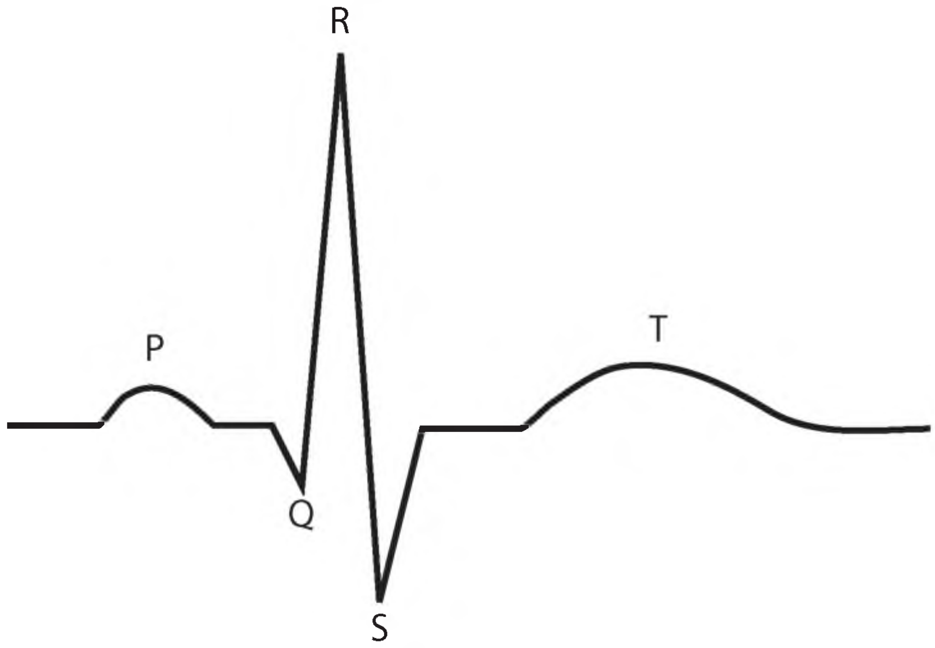

Figure 2.3: The schematic representation of a human ECG recorded on the body surface. The figure indicates the individual waveforms and their associated names.

a heart attack) provide strong motivation for much of the technical research carried out for this dissertation. Most of the examples used in subsequent simulation and modeling studies described below come from experimental and clinical studies of ischemia, which we describe in more detail in the next section.

2.3 Myocardial Ischemia

While myocardial ischemia has many definitions [44] and a complex and only incompletely understood etiology, it reflects fundamentally an imbalance of energy supply and demand in the heart and is responsible for an enormous proportion of heart disease and death. The heart relies on high-energy phosphates (HEP) to meet the metabolic demand of a continuously contracting myocardium [37]. To provide such energy, a steady supply of oxygen is needed for respiration in cell organelles called mitochondria that produce HEP through oxidative phosphorylation. When the supply of oxygen is insufficient, the myocardium still produces small amounts of HEP through anaerobic glycolysis along with the byproduct lactate. This reduction of HEP and the accumulation of metabolic products then alter the electrical conduction in the heart and reduce contractile function. Blood supplied through the coronary arteries carries this oxygen to the tissues of the heart and also provides a means of removal of metabolic byproducts and thus maintains healthy homeostasis. A useful definition of myocardial ischemia is a condition in which the metabolic demand of cardiac myocytes exceeds the supply of nutrients and oxygen received from the blood supply. Ischemia arises because of substantially ($> 80\%$) or fully occluded coronary arteries and in most Western countries myocardial ischemic disease is the leading cause of death and places significant strain on the hospital systems [9]. Heart tissue that is subject to complete ischemia (a full occlusion of a coronary artery or “myocardial infarction”) for extended amounts of time eventually dies and becomes necrotic and then scarred and prone to ventricular arrhythmias [45]. The limited ability of myocardial cells to survive without adequate blood flow makes the disease not only deadly, but also very time sensitive, driving the need for rapid detection techniques.

Even though the last century has seen many advances in detecting and locating regions of myocardial ischemia, rapid diagnosis of this condition remains unsatisfactory. Many of the techniques, such as blood tests and angiograms, provide reliable diagnostic capabilities of myocardial damage or compromised vessel lumen, respectively. However, they cannot localize the ischemia with precision and require considerable time and expense. Moreover, due to the time sensitive nature of ischemia, techniques that provide rapid feedback and minimal invasiveness are necessary. ECG signals, in particular what are known as "ST-segment elevations and depressions," have become important indicators of myocardial ischemia, despite an incomplete understanding of their physiological mechanisms and clinical interpretations [46]. Using ECG morphologies to diagnose ischemia has been insufficient in many instances and has accuracy rates as low as 70% [47].

To appreciate the source of errors in ECG based diagnosis of myocardial ischemia, it is necessary to first review the putative mechanistic link between metabolic imbalance at the tissue/cell levels and the resulting changes in body surface potentials. The ST segment of the ECG corresponds to a time interval during the cardiac cycle in which the ventricles have completely depolarized and all of the myocytes are in the plateau phase of their action potentials. This interval is visible in the ECG as the time between the end of the QRS complex and the start of the T wave and during this time there are only small differences in transmembrane potential between cells and thus no driving force between intracellular spaces of neighboring cell and very little current flowing through the heart. The consequences in the ECG are very small amplitude voltages during this time. However, in ischemic regions, the action potentials of cells display elevated (more positive) resting membrane potentials as well as decreased (less positive) peak potentials. Thus, during the plateau phase, there is a significant difference in potential between the ischemic cells and healthy cells. This potential difference causes currents, sometimes referred to as "injury currents," to flow between the healthy and ischemic regions [48, 40, 49, 50] as seen in Figure 2.4. Because both the healthy tissue and ischemic region are at two different potentials but relatively homogenous within each region, the boundary between the two regions is where the injury currents are formed. This is known as the electrical border zone and will be the topic of detailed study in Chapter 4 of this thesis. These injury currents propagate through the rest of the body and when they are directed away from a measurement electrode, that electrode records a negative potential or depression. In contrast, when the current flows towards an electrode, the electrode records a positive potential or elevation. In this context, an ST-elevation/depression indicates the direction of current flow and can sometimes be mechanistically tied to a pathophysiology. However, such interpretations are plagued by difficulty and ambiguity, in part because the ischemic regions may form isolated islands within the myocardium and are also quite dynamic in time [51]. As a result, the rate of errors in the detection of especially transient and exercise induced ischemia remain high [52, 53]. There have been several proposed mechanisms for ST-depressions supported by computational models, yet none of these have been adequately

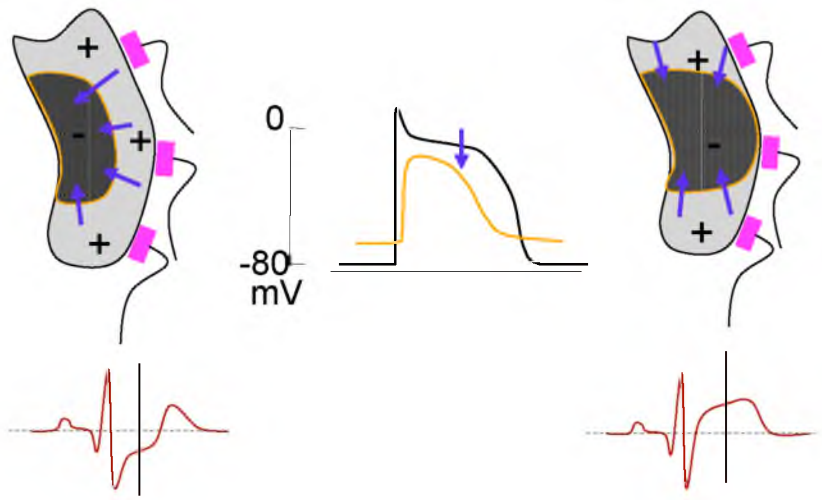

Figure 2.4: The schematic representation of the injury currents that arise during nontransmural and transmural ischemic episodes. The schemata on the left indicates a nontransmural ischemic region that results in ST-segment depression, while the schematic at right shows a transmural ischemic region that results in ST-elevation. The action potentials in the center indicate the typical action potential from ischemic tissue.

confirmed experimentally [50, 54, 49, 55, 56, 40, 57].

Despite the incomplete mechanistic understanding, ECG based methods are still widely used to identify ischemia. The rate of success in detecting ischemia is higher in the case of what is known as ST-segment elevated myocardial infarctions, STEMI [58], which correlate clinically with completely occluded arteries leading to ischemia and eventually infarction that is "transmural," *i.e.,* throughout the full thickness of the heart wall. Detection is significantly more difficult in the earlier stages or transient forms of ischemia, which often express themselves as non-STEMI or NSTEMI [59]. Transient ischemia can be due to partial occlusion of the coronary vasculature that cannot keep up with increased demand due to stresses such as exercise or during surgery. It can also be a result of transient occlusions of arteries due to vasospasms. ST-segment depressions are a frequent clinical marker of NSTEMI but they are rather unreliable and a poor basis for localizing the ischemic zone [60]. Though STEMI and NSTEMI are thought to share similar pathophysiology, they have been shown to respond differently to therapy, though the reason for this difference is unclear [32].

The generally unsatisfying diagnostic precision of ST-segment based detection of ischemia along with the poor mechanistic understanding of the relationship between injury currents and the resulting elevations and depressions in the ECG, underscores the need for subject specific computational models. Simulation generally provides the quantitative test bed to evaluate the entire set of features that are thought to contribute to the ischemic ECG. Subject-specific models capture the specific anatomy and structure of the heart and torso of each subject thereby reducing the role of geometric uncertainty in the simulations based on these models.

2.4 Computational Electrophysiology - Cellular Level

Closely linked to the experimental discovery of the electrophysiology of the cells and tissues of the heart is a series of mathematical, numerical, and computational models for the behavior of the heart across all scales. We begin a brief overview of cardiac simulation with models of the cell and then progress through myocardial tissue models to simulations of the whole heart.

The membranes of electrically active cells can be modeled as relatively simple parallel circuits consisting of resistive and capacitive components. The lipid bilayer of the membrane acts as a capacitor and the ion channels are represented as highly nonlinear resistive elements. The equilibrium (Nernst) potential associated with each ion species is represented as a battery. The challenge of such models lies in describing the nonlinear behavior of the ions channels and their complex voltage, time, and chemical dependence. Hodgkin and Huxley were the first to formulate this approach based on measurements from the squid giant axon and pioneered the field of computational electrophysiology [1]. This formalism is often expressed as an equivalent circuit (Figure 2.5). The basic structure of this circuit has served as the dominant formalism for membrane biophysics for the past half century and has been expanded with additional elements to capture more complex structure and behaviors but never abandoned. Even the most contemporary models of cardiac membranes owe their origins to this basic approach.

Using this equivalent circuit models the total membrane current can be written as

$$I_m^{\Phi_m,t} = C_m \frac{d\Phi_m^t}{dt} + (\Phi_m^t - \Phi_{Na})G_{Na}^{\Phi_m,t} + (\Phi_m^t - \Phi_k)G_k^{\Phi_m,t} + (\Phi_m^t - \Phi_L)G_L, \tag{2.4}$$

where Φ_m is the transmembrane potential, the Φ_{ion}'s are the Nernst potentials of the various ions and the G_{ion}'s are the membrane conductances; I_m is the total membrane

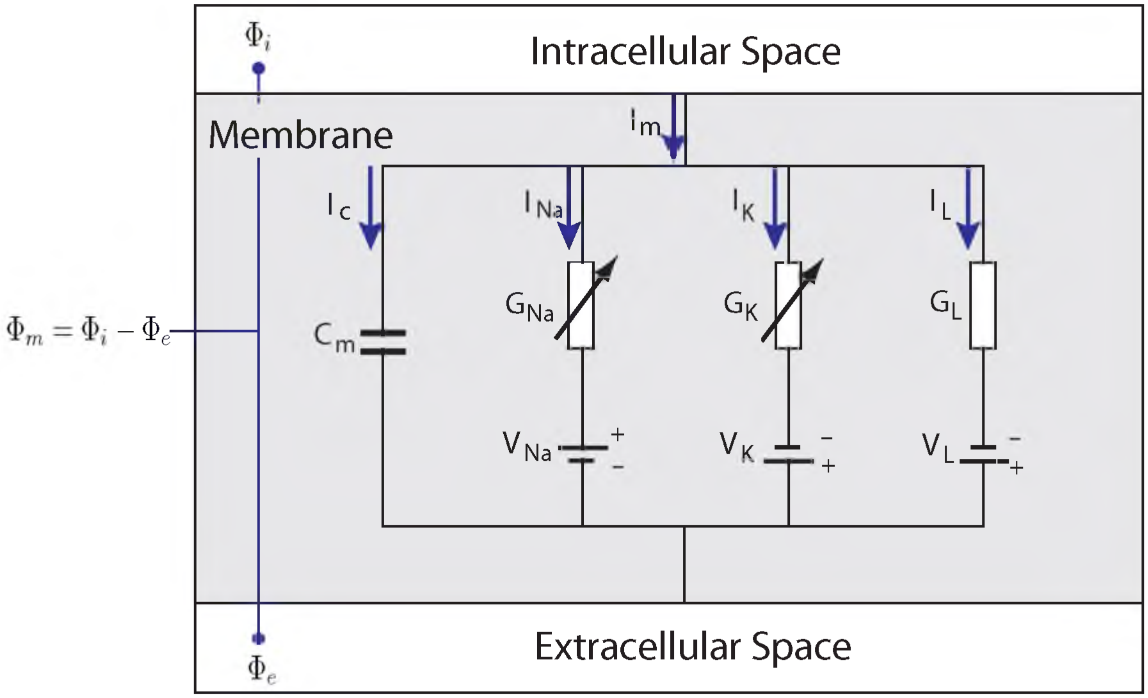

Figure 2.5: Hodgkin-Huxley equivalent circuit diagram of a squid giant axon. The diagram shows the initial model that included ionic channels with gating variables for Na^+ and K^+ to model the cellular dynamics of an action potential. The third arm represents the cumulative conductivity of various “leakage” currents in the membrane.

current. In the original formulation, the conductivities were modeled as simple first order kinetic equations of state (each ion channel transitions between its open and closed state with transition probabilities that capture the dependencies on time, voltage, and chemical environment). The voltage and time dependencies are established by fitting experimental results to appropriate differential equations. In more modern formulations, the channel opening and closing probabilities can be described in more detail as having multiple open and closed states, with transitions between states determined by stochastic probabilities. Numerically, such behavior can be captured with Markov models [61]. For example, an ion channel with two states, open and closed, would have a Markov model as shown in Figure 2.6. This formulation results in the following differential equation for the probability L that the ion channel will be in that conformational state.

$$\frac{dL}{dt} = \alpha_L(1-L) - \beta_L L \tag{2.5}$$

The rate constants α_L and β_L are derived from experimental data that describe the rate at which ion channels open and close as a function of voltage, time, or even ionic concentration.

In the Hodgkin-Huxley formalism [62], the membrane conductances G_{ion} are functions of the state variables m, h and n as seen in Eqns 2.6-2.8.

$$G_{Na}(\Phi_m, t) = \bar{G}_{Na\ max} m^3 h \tag{2.6}$$

$$G_K(\Phi_m, t) = \bar{G}_{K\ max} n^4 \tag{2.7}$$

$$G_L = const \tag{2.8}$$

The state variables can be defined by the Markov models in Eqns 2.9-2.11.

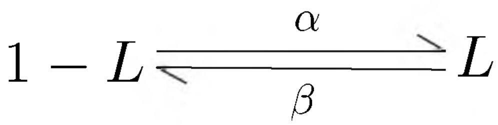

$$1 - L \underset{\beta}{\overset{\alpha}{\rightleftharpoons}} L$$

Figure 2.6: Markov model with two states. The schematic represents an ion channel with an open and closed state along with the rate constants α and β.

$$\frac{dm}{dt} = \alpha_m(1-m) - \beta_m m \tag{2.9}$$

$$\frac{dh}{dt} = \alpha_h(1-h) - \beta_h h \tag{2.10}$$

$$\frac{dn}{dt} = \alpha_n(1-n) - \beta_n n \tag{2.11}$$

The rate constants can then be curve fitted to experimental data, from which come Eqns 2.9 and 2.10, which show the rate constants for the gating variable m.

$$\alpha_m = \frac{0.1(25-V')}{e^{0.125-V'}}\frac{1}{ms} \tag{2.12}$$

$$\beta_m = \frac{4}{e^{V'/18}}\frac{1}{ms} \tag{2.13}$$

Contemporary cell membrane models include dozens of ion channels rather than just three and these models also include ion exchangers and calcium handling descriptions. The gating variables are not just functions of voltage, but they also may be functions of time and ion concentration. New models are still being created for different cell types and pathologies and many of them are described in a database known as cellML, in which the models are freely available to the scientific community. Common mammalian cardiac models include the TenTusscher model [63], the Luo-Rudy dynamic model [64], and the Faber-Rudy model [65] shown in Figure 2.7.

2.5 Computational Electrophysiology - Tissue Level

The cellular models discussed above are frequently used to study the electrical behavior of single cells or small groups of connected cells. However, there are approximately 4 billion cardiac myocytes in the heart [66]. If each cell were modeled with dozens of ion channels, each containing two to three state variables, the problem would be well out of range of any existing computational resources. For this reason, scientists have used the mathematical concept of homogenization to describe tissue as a continuum rather then a discrete set of individual cells and create new abstractions for tissue level modeling. The method most relevant to this dissertation and considered by computational electrophysiologists the best compromise between physiological and anatomical fidelity and computational resources is the “bidomain” model.

2.5.1 Bidomain Modeling

To go beyond a single small segment of membrane to a whole axon (the nervous system equivalent of a myocardial fiber), Hodgkin and Huxley [62] proposed what was the equivalent of an electrical cable model to simulate action potential propagation along a nerve. The equivalent in cardiac tissue are models of single or multiple, connected cables to simulate two- and three-dimensional behavior in cardiac tissue [67, 68]. This formulation can be further extended by completely integrating the extracellular and intracellular spaces of the tissue into what is known as the bidomain approximation [69]. The bidomain assumes two continuous domains that are fully overlapping in space, but coupled together through membrane currents as illustrated in Figure. 2.8.

In the bidomain, the intracellular and extracellular spaces are modeled as two continuously conductive domains and described by the following forms of Poisson's equations:

$$\nabla \cdot \sigma_i \nabla \Phi_i^t = \beta I_m^t \tag{2.14}$$

and

$$\nabla \cdot \sigma_e \nabla \Phi_e^t = -\beta I_m^t, \tag{2.15}$$

where the subscript i and e denote the intracellular and extracellular domains and β is the surface to volume ratio. The two domains are coupled such that current, βI_m leaving one domain must enter into the other domain. The difference in potential between the two domains is the transmembrane potential and is defined as

$$\Phi_m^t = \Phi_i^t - \Phi_e^t \tag{2.16}$$

The current flowing through the membrane is the same as described above for cell membranes, *i.e.,*

$$I_m^{\Phi_m,t} = C_m \frac{\partial \Phi_m^t}{\partial t} + I_{ion}^t + I_{stim}^t, \tag{2.17}$$

which contains a capacitance term, C_m, along with the current from membrane ion channels, I_{ion}, and stimulus current I_{stim}, which is either externally applied or from neighboring cells.

Combining Eqns. 2.14-2.16, we can rearrange the terms to solve for the extracellular potential, Φ_e, in terms of the transmembrane potential, Φ_m, as

$$\nabla \cdot (\sigma_i + \sigma_e) \nabla \Phi_e^t = -\nabla \cdot \sigma_i \nabla \Phi_m^t \tag{2.18}$$

The term Φ_m depends on time and must be solved over an entire cardiac cycle; however, in many instances it is possible to approximate the transmembrane potentials for different

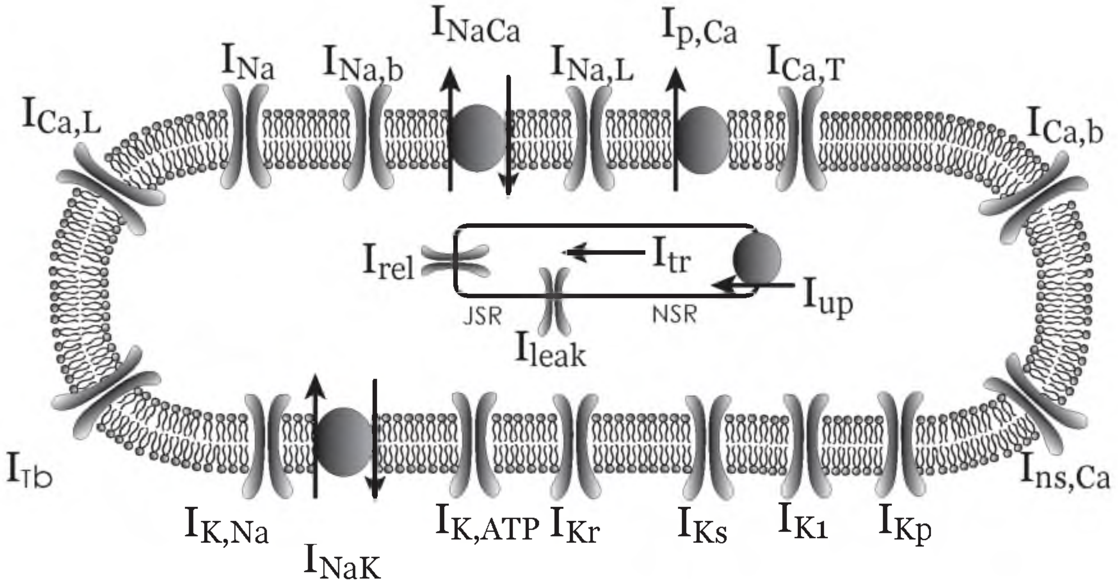

Figure 2.7: A schematic diagram adapted from the cellML repository of the Faber-Rudy cardiac cell model. The diagram depicts the ion channels and exchanges mathematically included in this model. The model is freely available to the scientific community in the cellML database.

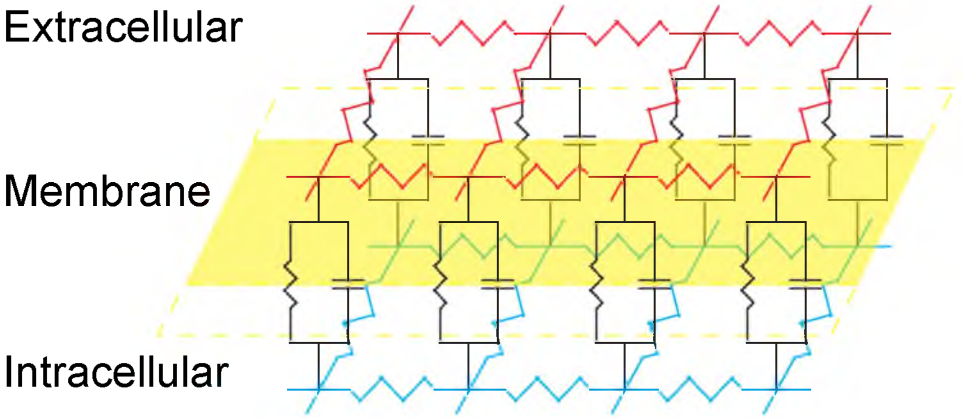

Figure 2.8: Schematic of the bidomain formulation. The bidomain can be pictured as a continuous representation of both intracellular and extracellular spaces as resistor network coupled by an approximation for membrane currents. Adapted from Roth (1992)

disease states at a single instance in time based on experimentally derived data. When the transmembrane potential represents a single instance in time, the result is called the “static bidomain” or a “single time point bidomain.” This approximation is best suited to time instances in which the transmembrane potentials are not changing rapidly or approximate steady state conditions. During activation there are two intervals that are considered steady state or close to steady state such that these approximations are appropriate. True steady state conditions occur between cardiac cycles. However, the ST segment is the time point that corresponds to the plateau phase of the ventricular myocytes and during this phase, the transmembrane potentials change very slowly, approximating a steady state. Over this interval, all of the ventricular myocytes have activated, but have not yet begun to repolarize.

The resulting simplification of the full bidomain equations above leads to an elliptical equation that requires solving a Laplace’s equation over a complex spatial domain, *e.g.,* the heart. Solving over anything but the simplest domains requires numerical methods, either the boundary element method (BEM) or the finite element method (FEM) [70]. The FEM has an advantage over other approaches in that it allows for the anisotropy of the myocardial fibers to be included in the model. Anisotropy is accounted for in both domains by varying the conductivities relative to the muscle fiber orientation. The FEM approach requires a geometric representation of the entire volume of the solution domain and any surrounding tissues [71] and constructs what is known as a stiffness matrix using a fairly standard approximation known as the Galerkin method [70]. Once the stiffness matrix has been created, the system of equations can then be solved using iterative Krylov-subspace-based solvers [72] such as the conjugate gradient (CG) and the minimal residual (MINRES) methods [73].

Without a static approximation of the membrane potential, it is necessary to solve a more complete form of the bidomain equations that include a cellular model to calculate the current crossing the cell membrane, I_m:

$$\nabla \cdot \sigma_i \nabla \Phi_m^t = -\nabla \cdot \sigma_i \nabla \Phi_e^t + \beta I_m^{\Phi_m,t} \tag{2.19}$$

This form of the equations leads to a parabolic problem and requires initial conditions such that it can be solved over time. Numerical integration schemes, such as the Forward-Euler method, are used to iteratively solve for the transmembrane potential through time [74, 75], where the membrane currents are calculated from a cellular model as follows:

$$\Phi_m^{t+\delta t} = \Phi_m^t + \frac{\delta t}{\beta C_m}(-\nabla \cdot \sigma_i \nabla(\Phi_m^t + \Phi_e^t)) - \beta(I_{ion}^t + I_s^t) \tag{2.20}$$

The extracellular potential is then solved as a separate step and plugged back into the Eqn. 2.20 for subsequent iterations as follows:

$$\nabla \cdot (\sigma_i + \sigma_e)\nabla_m^{t+\delta t} = -\nabla \cdot \sigma_i \nabla \Phi_m^{t+\delta t} \tag{2.21}$$

2.6 Computational Electrophysiology - Whole Body Level

To extend the simulations of cells and then tissues to generate body-surface potentials requires a further level of homogenization and simplification into what are known as "volume conductor" problems. In this case, there is a bioelectric source, which are simplifications of the currents generated by the whole heart, and a volume that is electrically conductive. Thus it is necessary to know and represent both the source and the realistic volume conductor, including its shape and (typically inhomogeneous and potentially anisotropic) conductivity, again in a numerical approximation that captures necessary details and remains computationally tractable. The formulation we have just described is a form of "forward problem," *i.e.,* the source the volume conductor are known and the goal is to estimate remote (in this case body-surface) electric potentials. As in many areas of physics, one can also formulate the associated inverse problem that uses remote measurements, such as body-surface electrocardiograms, to locate the electrical current sources from the heart, given knowledge of the volume conductor and the choice of source model formulation.

2.6.1 Electrocardiographic Forward Problems

The biophysical background of the forward problem begins with the generalized version of Ohm's law as follows:

$$J_i = -\sigma_i \nabla \Phi_i, \tag{2.22}$$

where J_i is the current density in region i, σ_i is the conductivity tensor, and $\nabla \Phi_i$ is the potential gradient. Taking the divergence of the both sides of this equation results in the base formulation of the spread of current through a volume conductor described by either Poisson's or Laplace's equation as:

$$\nabla \cdot (\sigma \nabla \Phi) = -i_v = \nabla \cdot \vec{J^i} \tag{2.23}$$

and

$$\nabla \cdot (\sigma \nabla \Phi) = 0, \tag{2.24}$$

respectively.

Eqn. 2.24, Laplace's equation, describes a condition in which there are no sources or sinks within the volume. The boundary conditions for this model are derived from the physiology of the problem. Ischemia produces current sources within the heart which can be modeled as Dirichlet boundary conditions, *i.e.,* known potentials on the heart surface.

Any boundary with air, a nonconductor, leads to Neumann boundary conditions,

$$(\sigma \nabla \Phi) \cdot \mathbf{n} = 0 \tag{2.25}$$

in which no current flows out of (or into) the body.

When the heart is a source embedded within the volume conductor, the conditions at its boundary can be described as:

$$(\sigma_i \nabla \Phi_i) \cdot \mathbf{n}_i = (\sigma_j \nabla \Phi_j) \cdot \mathbf{n}_j \tag{2.26}$$

i.e., the normal component of the current at the boundary is conserved.

There are many different volume conductor models based on these simple equations, each employing a different cardiac source model formulation. Perhaps most complete but also most computationally challenging is a formulation that couples the bidomain model of the heart within the torso volume conductor and solves the entire problem as one large, coupled system.

2.6.2 Inverse Problems

The purpose of the inverse problem in electrocardiography is to locate the electrical source that corresponds to a physiological event based on body-surface electrical potentials. The components of the inverse problem are the source description, geometry of the volume conductor, conduction tensors, forward solution, and inversion method or regularization. Although every inverse problem is based in some way on a forward problem, the focus of this research is entirely on refining a forward problem so that further discussion of this inverse problem is well outside the scope. For more details, see, *e.g.,* [76, 77].

CHAPTER 3

IMAGE BASED MODELING PIPELINE

While there is rich variety in the diversity of applications of computational modeling, for example, aerospace, climatology, and biomedicine [78, 11, 79], there is also a common set of specific technical techniques or steps that many modeling applications share. In particular, many simulations rely on structure or anatomy and the ability to mathematically represent the three dimensional shape of the object being simulated. For example, to simulate the stress produced in a beam when placed under loading conditions, one must first mathematically represent the shape of the beam in order to solve the equations that model stress; an I-beam produces a very different stress profile from a rectangular beam. Early models used geometry based on simple shapes such as rectangular boxes, cones, and spheres to approximate more complex objects. This approximation not only makes for simple representations of shape, but also allows the physics based equations to be solved analytically rather than numerically. However, this method is limited to fairly simple geometries and is not sufficient in many domains. For such situations, it is necessary to create more complex geometric models and to employ numerical approximations of the underlying equations. Numerical methods such as finite elements (FE), finite differences (FD), and the boundary element method (BEM) are approaches that allow engineers to simulate over much more complex geometries [80, 70]. However, this flexibility also comes at a cost; numerical approximations such as these rely on tessellating or tiling complex surfaces by representing them as many small, simple polygons such as triangles and quadrilaterals for surfaces and tetrahedra, hexahedra, and prisms for volumes. Thus a real, continuous or smoothly shaped object becomes approximated by the union of many small elements and the resulting geometric model is generally referred to as a mesh or a grid. The human torso mesh in Figure 3.1 is an example of such a discretized geometric model. Just as the object or shapes are discretized into many small elements, the equations describing the behavior of interest are also solved many times for each of the elements in the mesh. This general formulation is common across many application domains and is essential for solving realistic problems such as bioelectric activity in the heart and torso.

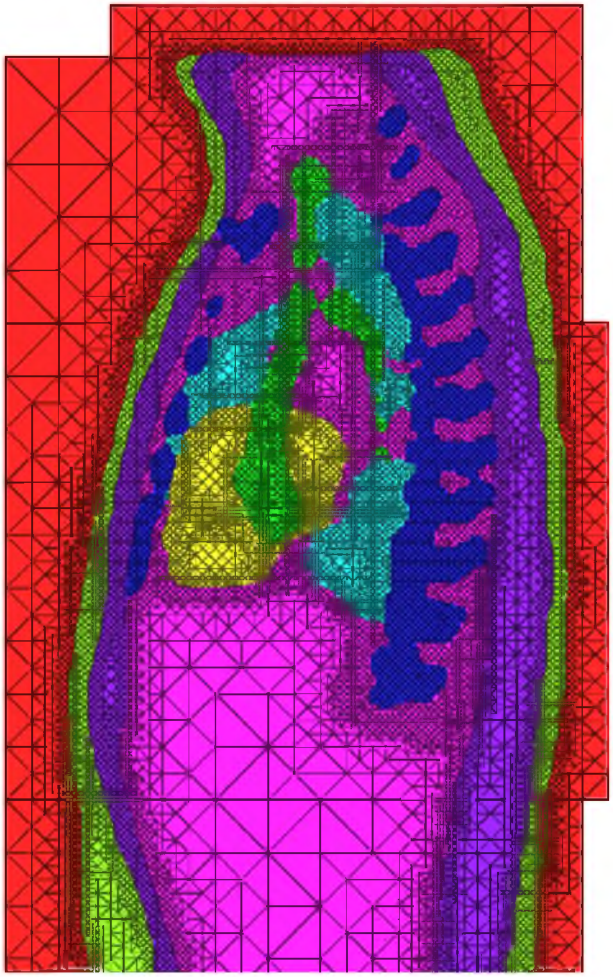

Figure 3.1: A mesh of a human torso with each color representing a different tissue type. The figure is a cross-section of a human torso in which each tissue is tessellated using tetrahedral elements constructed using what is known as a "stenciling" algorithm. The outermost, red region represents space outside the torso, the green represents the skin, the dark purple the subcutaneous fat layer, and the lighter purple the viscera and internal connective tissues. The dark blue regions are from bones, the light blue and green major vessels, and the yellow a region of the heart. (Courtesy of Jonathan Bronson)

There are many ways to mathematically describe geometry from which the tessellation will be created, but there are two general and common approaches. The first is to explicitly build the geometry with a computer aided design (CAD) system that approximates the underlying shapes using bezeir/spline surfaces that are stitched together in order to form complex volumes [81]. The second approach is to capture the geometry using an imaging modality such as magnetic resonance imaging (MRI) or computational tomography (CT) and then carry out segmentation of the regions of interest. Many engineering disciplines rely heavily on geometry from CAD systems. However, in biomedical engineering, image based modeling is much more prevalent [11]. This choice results in part from the availability of image data and imaging facilities used to diagnose and treat patients. More importantly, it is difficult, if not impossible, to obtain measurements of internal tissues and structures in living subjects without using some form of imaging technique. This widespread use of medical imaging has led to the development of tools and techniques that specialize in converting image data into suitable computational models for simulation.

The creation of the geometric model is just one step in a pipeline or workflow that is common to many simulation scenarios, a sequence that we describe as "image based modeling and simulation" and convey schematically in Figure 3.2. The pipeline begins with images and contains all the necessary steps, which we describe below in more detail. While the implementation of each step can be more or less challenging depending on the nature and scale of the specific application, the elements share common features, which also facilitates at least some level of common algorithms and software. Another commonality to many applications is the need for refinement based on specifics of the boundary conditions or initial results, as indicated by the arrows and upstream connections in the figure. The following sections outline the steps of the image based modeling pipeline and discuss some of the considerations in relation to model creation for each step.

3.1 Image Acquisition

There are many factors to consider when designing an imaging protocol for computational modeling. Many of the decisions made at the imaging step affect downstream processing and can greatly limit their efficacy. The type of tissue being imaged, the level of structural detail being captured, and the tolerable dose of radiation are all factors that play a significant role when designing a protocol. While part of the decision depends solely on the anatomy being imaged, a large part is also dependent on the simulation requirements such as the level of spatial detail that is needed to accurately simulate the physics. Below

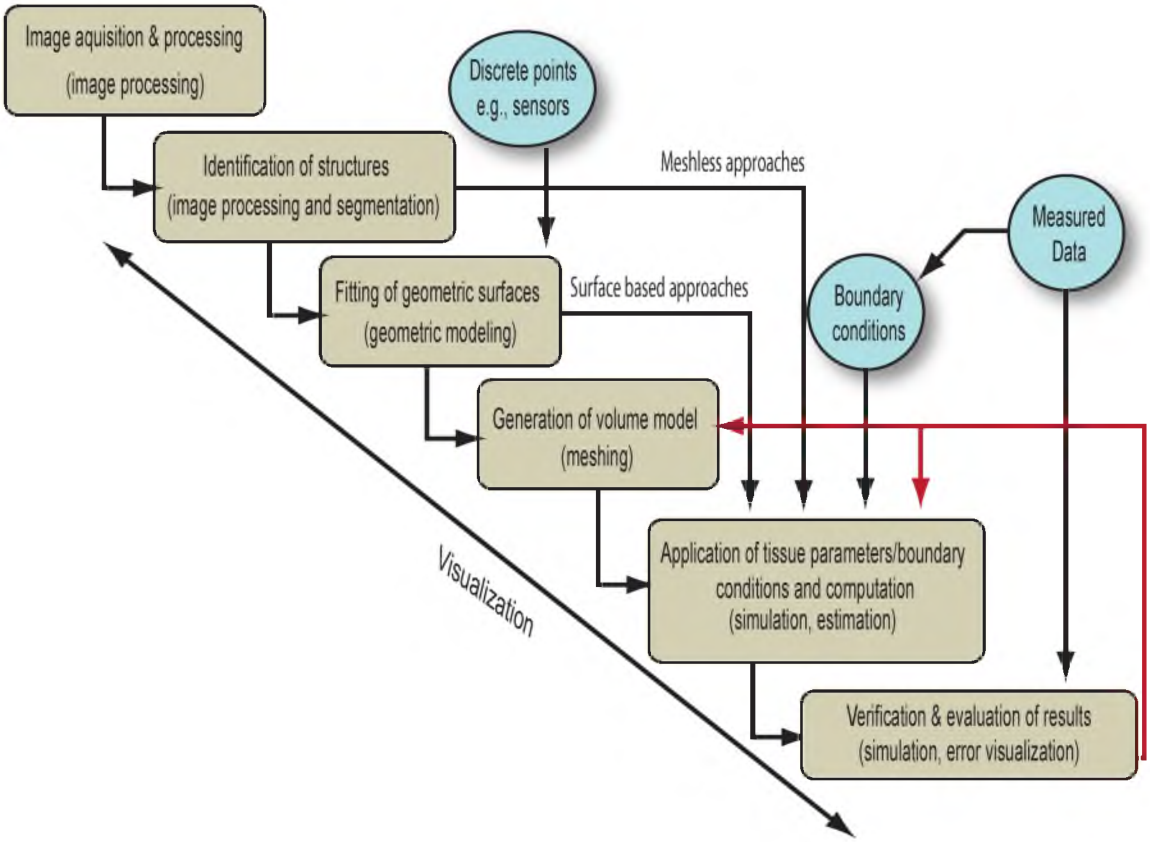

Figure 3.2: Image based modeling and simulation pipeline. The sequence of steps common to many problems in modeling and simulation begins with images, requires the construction of a geometric model, the application of boundary conditions, and the solution of sets of equations by means of numerical approximation and computational solvers. Feedback is a required element as the outcome of some stages can drive refinement of upstream elements of this pipeline. (Courtesy of Rob MacLeod)

we will summarize some of the important imaging parameters that are specific to cardiac electrophysiology as well as outline some of the strengths and weaknesses of different imaging modalities.

One of the greatest limitations of image data is that it stores continuous and often smooth shapes on a discrete grid [82], thus sacrificing some level of detail. Each pixel of the resulting image, or "voxel" of the resulting volume, is assigned an intensity value that depends on the quantity capture by the particular imaging modality. Images that are suitable for creating geometric models must encode in their voxels some form of tissue characteristic, *e.g.,* tissue density for x-ray based images or water content for MRI. As a result, each voxel of the same material has a similar intensity and jumps in voxel intensity signify boundaries between tissue regions (or organs). An important consequence of the limited resolution of any imaging modality occurs at the material boundaries where multiple materials meet. Voxels containing information derived from a mixture of materials have intensities that are a weighted average over all the tissues within the voxel, also known as "partial volume effects" [83]. The result of this discretization error is that sharp boundaries become blurred and that smooth boundaries become discretized or "stair stepped." One consequence of inadequate sampling resolution and partial voluming arises when algorithms that create continuous surfaces cannot follow regions of high curvature and create holes in thin features such as pleural or pericardial linings in the thorax or even the walls of chambers in the heart.

An additional challenge arising from resolution is overlapping intensity ranges between tissue types, *i.e.,* voxels from what are two different tissue types show intensity values that are not clearly separable. Overlap can arise due to noise in the image or from intrinsic limitations or specific settings of the scanning modality [82]. For example, in MRI, inhomogeneities in the magnetic field result in variations in image intensity over the entire field of view, such that one tissue may have a value in the center of the field of view that overlaps with that of another tissue further away from the center [82]. In some cases contrast agents can improve tissue differentiation. However, this is not always possible or may cause unwanted side effects [84]. While optimizing raw image quality is always the best strategy for achieving high quality geometric models, there are also image processing strategies that can facilitate the identification of tissue regions and boundaries, a process known as "segmentation" that we will describe in more detail below.

Imaging the heart has additional challenges because in a living organism it is not fixed in place. With every cardiac beat, the heart rotates and shortens and then returns to its original position. This motion couples with respiratory motion that shifts the heart up and down as much as 2 centimeters during breathing [29]. To account for these types of motion, scans must be taken very rapidly or gated to the cardiac cycle and even respiratory phase. Breath holds are utilized to control respiratory motion for shorter scans whereas longer scans must also be gated to the respiratory and cardiac cycles. Gating the scan can significantly increase the total scan time, which, in turn, enhances the probability of motion artifacts due to postural changes of the patient. Cardiac motion also makes some already lengthy scans, such as diffusion tensor imaging (DTI), so long that they are not currently possible on living subjects [85].

There are many imaging modalities used clinically, though CT and MRI, as seen in Figure 3.3, are preferred for constructing geometric models because of their high resolution, consistent registration, and generally high image quality. In contrast, ultrasound based imaging has a very poor signal to noise ratio while nuclear medicine has very poor spatial and temporal resolution, even though both are very valuable clinically for their ability to capture functional details rather than anatomy [82]. The choice between CT and MRI is often based on the type of tissue being imaged and seeks to balance the improved spatial and temporal resolution of CT against its ionizing radiation burden as well as the need for contrast agents to capture soft tissue. CT images bone and other dense material very well, whereas MRI has higher contrast between soft tissues and is generally more versatile. CT scans run an order of magnitude faster and provide several times higher spatial resolution than MRI, but require exposure to ionizing radiation [82]. An additional limitation of MRI, especially the higher field systems (3 Tesla and above), is that patients with implantable defibrillators or pacemakers cannot be placed inside the large magnetic fields of an MRI with complete safety so that patients with these devices must receive CT scans. The versatility of MRI arises through a combination of contrast agents, typically based on gadolinium, and variations in the pulse sequences that are under software control and provide for a very wide range of accommodation to different tissues and tasks[86].

Because of the relative advantages of both modalities, the ideal scenario is to combine multiple scans that each focus on a different aspect of the anatomy. However, in a typical clinical setting it is rare that scans are taken solely for modeling purposes so that a single modality at moderate technical quality is adequate. While the resulting scans do not represent all that the state of the art has to offer, they are often adequate for extraction of tissues and hence the construction of geometric models.

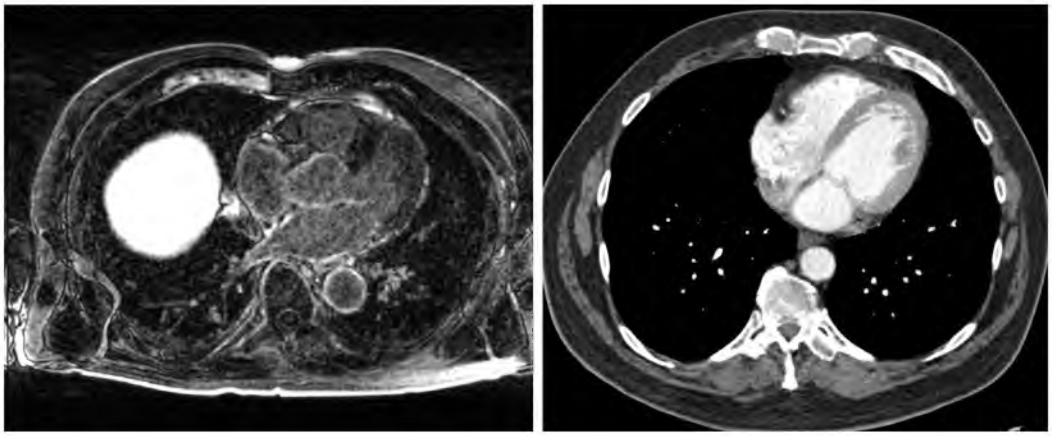

Figure 3.3: MRI and CT axial slices of a human torso MRI scan.
The figure at left shows an MRI slice of a human torso in the axial direction showing many of the tissues within the torso. The figure on the right is a CT slice with the bones and heart clearly identifiable due to the use of a cardiac contrast injection.

3.2 Segmentation

Segmentation is the process of identifying tissues and structures within an image and giving each pixel (2D) or voxel (3D) a label which associates that unit of the image with a particular tissue. Figure 3.4 shows an example of a segmentation of a torso model prepared and visualized using Seg3D [19], a custom, interactive program created at the SCI Institute of the University of Utah. The result of segmentation is what is known as a “label map” a discrete version of the original images in which each voxel receives a “label” identifying its tissue type. The number of labels is much smaller than the number of possible voxel intensities so that a label map is also a very compressed version of the original images. The process of identifying tissues types within an image can be subjective as well as very time consuming. A typical workflow (described in more detail below) is to first filter, *e.g.*, improve contrast or otherwise sharpen boundaries between tissues, the images to allow either automated or user driven identification of boundaries to be more dependable. Achieving segmentations of acceptable quality for subsequent geometric model construction can rarely be fully automated as boundaries can be intermittent or too subtle for consistent success with current image processing algorithms. Human guidance then becomes necessary and quality of segmentation ultimately depends on the skill and experience of the user.

3.2.1 Image Preprocessing

Before segmentation, it is often necessary to use smoothing spatial filters to remove from image noise and small intensity artifacts that are either the result of imaging errors or reflect

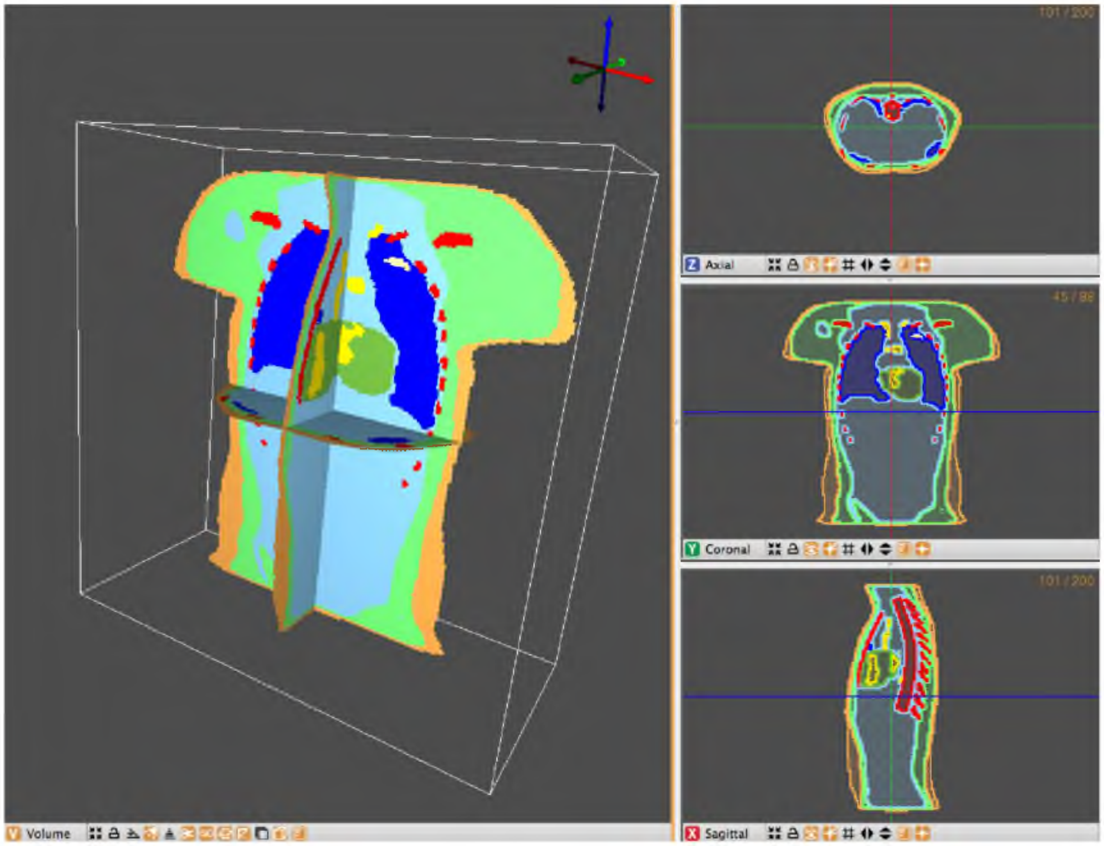

Figure 3.4: A segmented torso MRI scan produced by Seg3D. The figure shows the graphical display of Seg3D with a segmentation of a human torso in which every color represents a separate tissue type. The label maps are written to file as integer values representing each tissue.

heterogeneities in the tissue. Smoothing spatial filters not only remove noise but they also close tiny gaps in lines and edges, which can be important when interpreting the image and applying subsequent model construction algorithms [87]. The workflow presented here relies heavily on median [87] and Gaussian anisotropic filters [88], which blur or average the image, but also attempt to preserve important features such as edges. These filters are particularly useful to remove what is known as “speckle noise” and other small variations within a material while still preserving the salient features of the image.

3.2.2 Automated Segmentation Algorithms

Fully automated segmentation usually relies on *a priori* knowledge of the object represented by the image. Atlases of average shape representations are built into such segmentation routines, which then try to minimize the variation between the specific case and the atlas while identifying material boundaries [89, 90]. Such approaches can be very powerful in settings in which variation between subjects is relatively small and have shown great utility in brain segmentation [91, 92, 93]. However, when there is even modest natural variation between subjects, *e.g.,* the human torso or the heart, the resulting larger variance in the atlas means reducing the utility of such approaches.

In the workflow presented here, semiautomated routines were used to segment the cardiac MRI and CT images. The most basic method utilized in our segmentations was thresholding. Image thresholding identifies similar regions of the image, presumably the same tissue type, based on defining a range of intensity values. Thresholding is useful in images with very good contrast between materials so that each intensity value range uniquely reflects one particular material. However, in many instances, thresholding alone was not sufficient. More typically, intensity values are not unique to one material, *i.e.,* there is overlap between intensity ranges representing different tissues. In these cases, more sophisticated segmentation techniques such as water-shedding [94] and neighborhood connected methods [95] were used to identify the tissues of interest.

3.2.3 Manual Segmentation

Manual segmentation was often necessary either as a means of identifying regions within images that were too challenging for automated approaches or as a means of editing or correcting automatic or semiautomatic segmentations. The process was completely manipulated by the user and fortunately a rich set of approaches and tools existed to assist in the otherwise time consuming operations required for manual segmentation. For example, one can select multiple voxels at a time using a variety of selection tools such as paint brush or contour drawing tools, some of which are common to graphical drawing programs [96]. In Seg3D the approach is based largely on painting of regions, sometimes constrained by a mask created either from a previous automated edge detection or from an adjacent slice in the image volume [19].

3.3 Physiological Data Acquisition

In addition to anatomical features, it is often necessary to collect spatially distributed signals or parameters from the physiology that is the actual goal of the simulations. Especially in simulations based on anatomical substrate, these physiological data may also be associated with specific locations in space and thus it is necessary to align or register the physiological with the anatomical information. In the case of the heart, for example, there are often electrical potentials and what are known as "activation times" measured at discrete locations on the heart. Other examples from biomedicine and beyond include properties such as flow, electrical or thermal conductivity, stiffness, magnetic field strength, and many more, all of which are subsequently used in the simulations.

In order to associate such measured data with the correct spatial locations of the anatomy, sensor locations must be recorded using a variety of techniques. Common examples include magnetic tracking or navigation systems [97, 98], in which the interaction between a magnetic field and the measurement device allow localization of the sensor, and mechanical digitization [99, 100], in which an arm or a other form of mechanical or electromagnetic linkage records the spatial location of the sensor relative to a common coordinate system. Both systems record the spatial locations of the sensors in a coordinate system that is independent of that of the imaging system, thus requiring subsequent alignment or registration of the two geometric frames of reference (see next section).

3.4 Registration

Registration is the process of transforming two or more sets of spatially organized data into the same coordinate space [101]. In the context of the image based modeling pipeline, the data is comprised of surfaces, discrete measurement points, and images. Figure 3.5 shows a typical example, in which heart anatomy (from MRI) and coronary vasculature (from CT) are merged with what are known as "plunge needle" recording devices for capturing electric potentials within the volume of the heart (from mechanical digitization) [102, 103]. While there are subtle differences between registering points, surfaces, and images, the

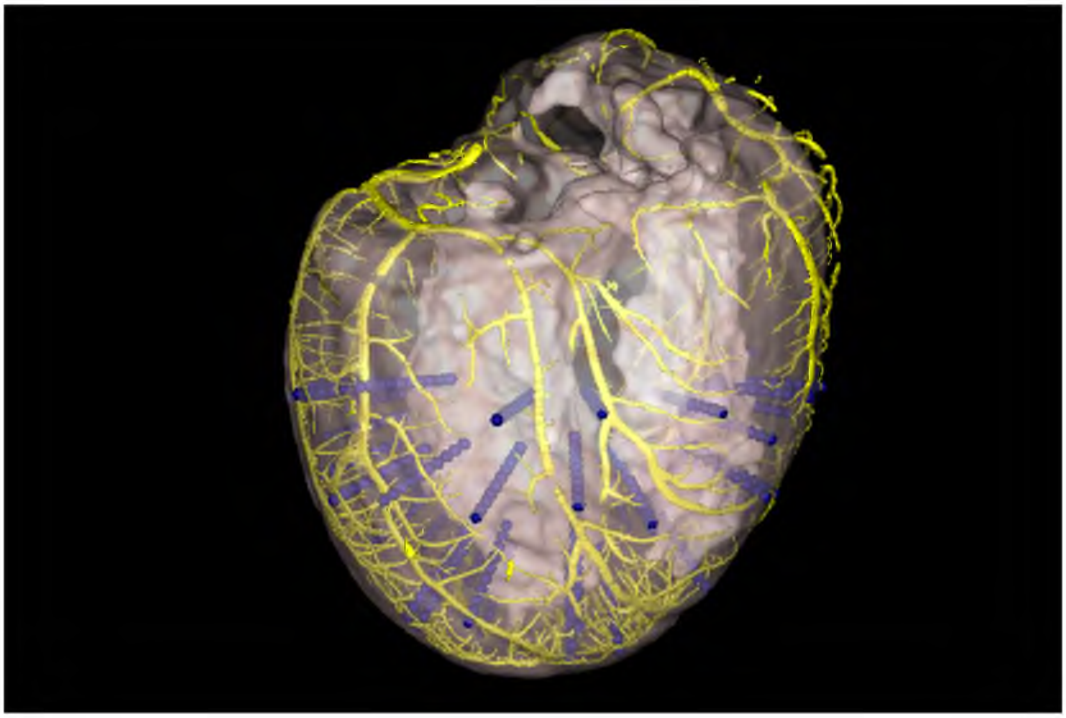

Figure 3.5: Three different data types registered into the same space. The grey transparent surface represents the surface of a canine heart obtained from an MRI scan. The yellow vessels are the coronary vasculature of the same heart, but obtained through a CT scan. The blue spheres represent locations at which electrical signals were recorded, where the locations were obtained using a digitizer.

basic principles are the same. Registration techniques can be organized into two categories, features-based and area-based methods [104]. For our workflow, only feature-based methods were used and will be discussed here. More comprehensive descriptions of registration techniques can be found in other texts [104].

3.4.1 Feature-Based Registration

Feature-based registration uses landmarks, often anatomically obvious locations that are invariant over time and are identifiable in all the different modalities to be registered. The resulting transformations used to align the landmarks can be rigid and linear [105], or can also scale or even distort and morph the geometry with nonlinear [106] transformations depending on the requirements of the registration. In many applications the required landmarks are distinct features such as roads, rivers, and intersections or more generally points, lines, and edges, that are easily identified either automatically or manually [104]. However, in medical images it is often difficult to find structures or landmarks that are easily identifiable between images. Such detection of landmarks often requires medical experts to identify anatomical correspondence points which can be particularly challenging in three-dimensional images, a source of error in the resulting geometric models. Where feasible, it is often advantageous to fix markers to the body that are visible across image and feature identification modalities.

3.4.2 Application to Cardiac Modeling

In cardiac imaging, the vasculature of the heart, particularly the bifurcation points of the major arteries, offer easily identifiable landmarks that can be used as correspondence points. Acquisition of these locations requires use of contrast agents but these exist for both MRI and CT. Vascular catheters as well as direct access with digitizers in experimental settings provide means of locating these bifurcations. However, the challenge of detailed registration of cardiac information lies in the fact that the heart is not a rigid body and deforms over time. Often, acquisition of electrical sensor based data occurs across the entire cardiac cycle whereas the MRI and CT images are captured at a single time point in the cycle. For this reason, nonrigid transformations are often needed to map measurement data to image data.

3.5 Surface Meshing

The creation of discrete polygonal geometric models or meshes is the next step in the image based modeling pipeline [11]. In this section we describe surface meshing as separate from volume meshing because there are distinct technical challenges to each. However, in some algorithms, surface and volume meshing are not separate processes. Surface meshing requires identifying and tessellating the boundaries between materials, as well as the outermost enclosing boundary, from a segmentation or label map of the underlying tissues. Surfaces that are smooth in reality are represented in the label map as discrete approximations. Thus, the challenge becomes converting this discrete, often distorted or “stair stepped” representation to a discrete representation that most closely approximates the smoothness of the original surface.

These challenges are compounded when three or more materials converge, as often occurs in living tissues [107]. In many cases, this process is broken into two steps, first creating a smooth representation of the boundaries and then representing these surfaces as discrete triangle or quadrilateral elements.

As discussed previously, segmentation is a necessary step in order to identify the various tissues within the image; however, for many types of segmentation, this process removes information necessary to reconstruct isosurfaces that approximate the smoothness of the original surfaces. When an image is segmented, it represents images as a very small number of different tissue types, effectively reducing the original number of discrete image intensities (on the order of thousands) to the order of 10 different labels. Many segmentation tools, such as Seg3D, produce "hard" boundaries between labels, in that there is no transition between labels, but each label defines a discrete region. A direct consequence is that an isosurface derived from such a representation must cross at the midpoint between two labels, thus capturing and preserving the stair-stepped artifacts based the underlying grid. In contrast, a "soft" boundary, which has values that transition from one side of the interface to the other, leads to an isosurface that utilizes interpolation to give subelement resolution of the boundary location. The difference between these methods is illustrated in Fig 3.6.

While there are some applications that produce "soft" segmentations, most produce hard segmentations; in our modeling pipeline, we dealt exclusively with the latter type of label maps. The challenge then becomes how to use the coarsely resolved label map to generate a suitably smooth estimate of the boundaries. For this step we have used a smoothing operation, *e.g.,* Laplacian smoothing [108, 109], curvature limited smoothing [110], or surface fitting techniques [111]. The resulting surfaces are smooth and are adequate representations for some applications, such as visualization. However, many simulations are sensitive to the

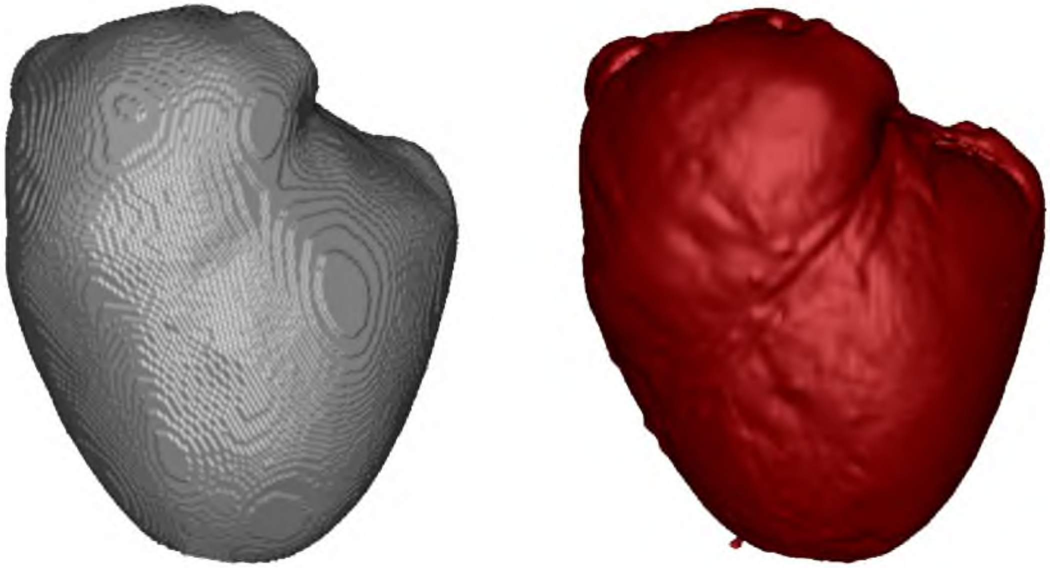

Figure 3.6: A comparison of isosurfaces between a "hard" segmentation and the raw data. The figure at left is the isosurface generated from the segmented data, showing the stair-stepped artifacts. The figure at right shows the smoother isosurface that can be produced from the raw image data.

shape of the elements used in the mesh and require further refinement. Elements with very sharp angles can produce poor numerical results [112] and there is no guaranty of well shaped elements from the previous steps. Some approaches iteratively evaluate the mesh and adjust poorly shaped elements [113, 114], while others utilize the smooth surfaces to create an entirely new mesh.

One approach to remeshing the smooth isosurfaces that have poorly shaped elements is to utilize a scalar field representation known as “indicator functions” [115]. In this technique, the scalar field represents the distance of each node to the nearby intended surface. Nodes on one side of the surface will have a positive distance and those on the other side negative while the zero-crossing of the distance field defines the location of the surface. By using an interpolation function across each grid element, the zero crossings can be located anywhere within the element. The indicator function can then be meshed utilizing algorithms that produce well shaped elements, such as variational methods that optimize the node locations [116, 115], or stenciling methods [117] with bounds on the permissible angles between faces of the element. The custom software from the SCI institute known as BioMesh3D [118] implements these strategies and Figure 3.7 contains a result from MRI images of the human skull and brain.

3.6 Volume Meshing

In simulations based on the finite element method (FEM) or visualizations of three-dimensional structure or associated function, a surface definition of geometry is not sufficient. The volume defining the space also needs to be tessellated into small three-dimensional elements, an aim typically achieved with hexahedra, tetrahedra, prisms, or pyramids [119]. Different element types have different computational properties and the choice of element type is dictated by simulation or visualization requirements. Tetrahedral meshing is perhaps the most versatile and can be used to capture complex and irregular geometries, while hexahedral elements are more efficient for certain computations [119, 120], particularly in mechanical simulations, despite the resulting poor rendering of many shapes. The construction of tetrahedral and hexahedral meshes involves very different algorithms and will be considered separately below.

3.6.1 Tetrahedral Mesh Construction

Volume meshing with tetrahedral elements is well understood and has stable and robust technical solutions with moderate computational cost. In cases in which surfaces are already

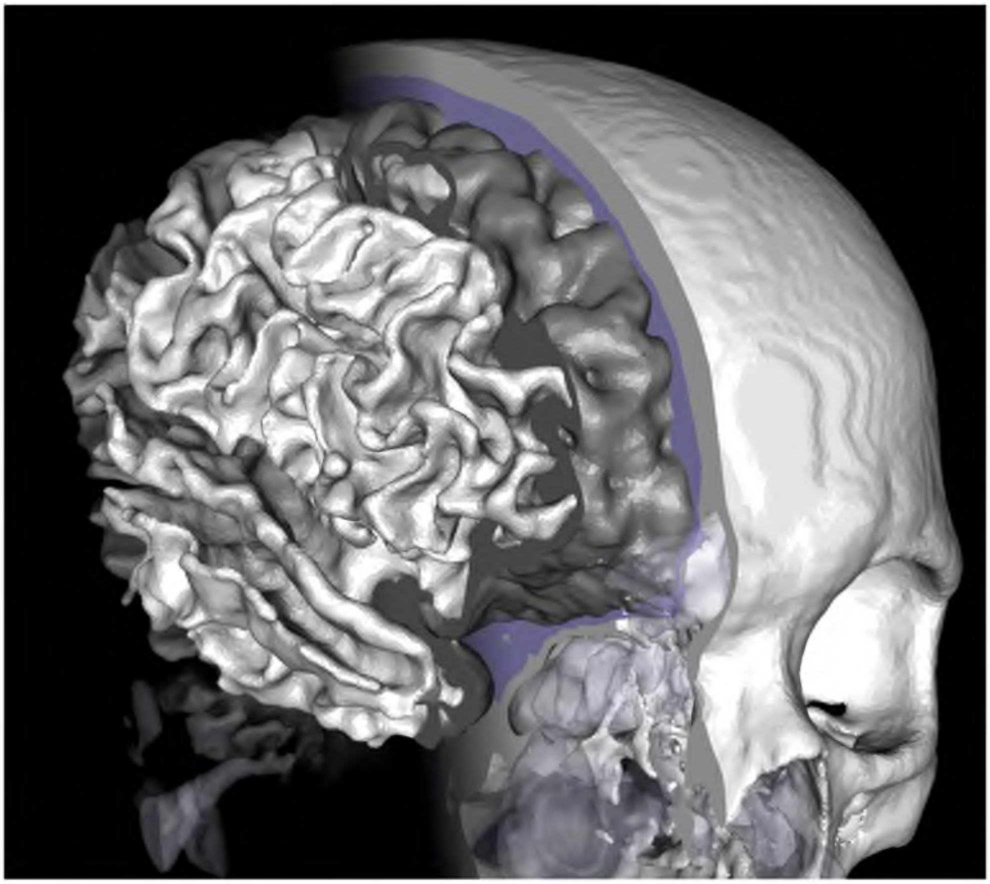

Figure 3.7: A smooth surface representation of a brain and skull. A variational meshing algorithm, Biomesh3D, produced the smooth surface representations of the brain, white and grey matter, CSF, and skull based on an MRI image of a head. Some of the tissues are clipped away in order to visualize the inner tissues.

meshed with triangles in a piecewise linear complex [121], constrained Delaunay-based algorithms [122] produce tetrahedra with optimal aspect ratios. Figure 3.8 contains an example of such a mesh with color indicating the different tissue regions captured in this very detailed and highly realistic mesh. Other techniques for tetrahedral meshing include stencil based approaches, which are very fast and can produce very uniformly shaped and sized elements [117].

3.6.2 Hexahedral Mesh Construction

Hexahedral meshes can be much more challenging to generate than those based on tetrahedra. The level of difficulty depends on the underlying shape (or label mask) and there are specific shapes that lend themselves to this type of meshing, for example, spheres

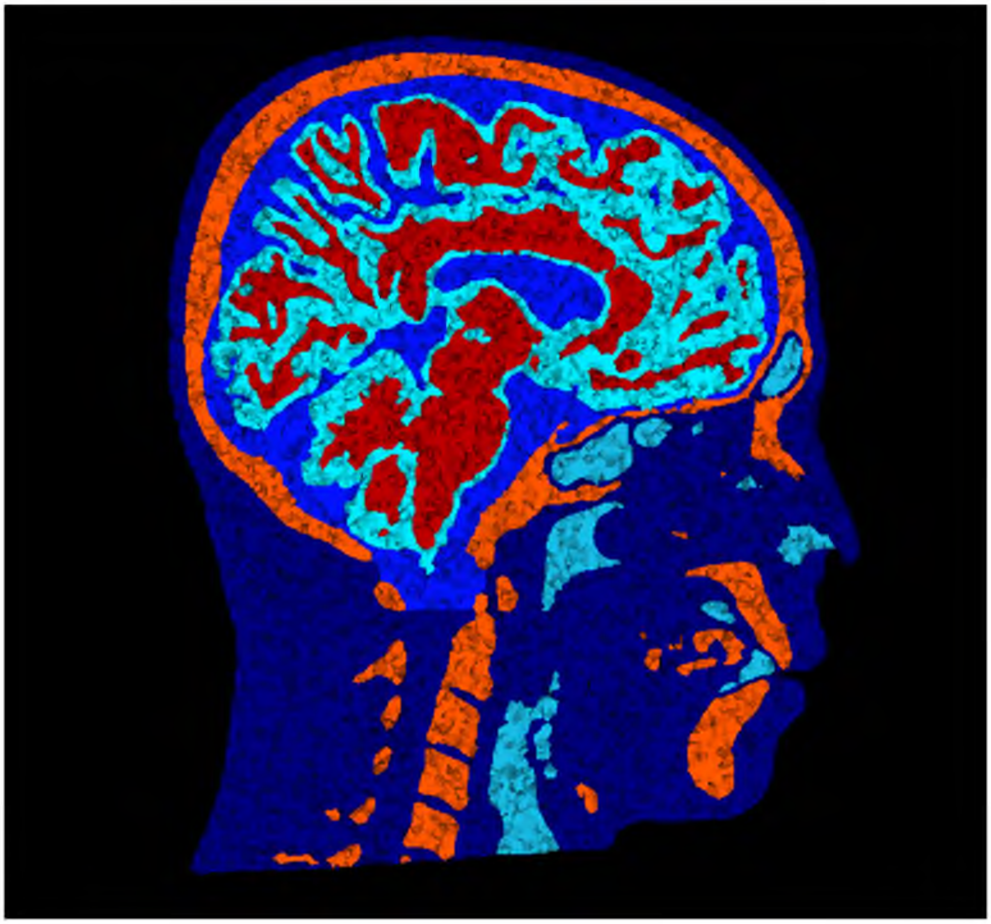

Figure 3.8: A cross-section through a volumetric tetrahedral mesh of a human head. The figure shows the inner tetrahedral mesh of a human head, where each color represents a different tissue type. The tetrahedral elements were produced using a Delaunay-based algorithm.

and rectangles, for which there exist predefined templates [123]. In some instances, a single face of an object can be meshed with quadrilateral elements and then the resulting two-dimensional mesh "lofted" or revolved through the three-dimensional object to define the hexahedral elements [124]. Other techniques are based on Octree approaches [125, 126] that subdivide cubes until there is sufficient resolution, creating irregular cells at the boundaries. Poorly shaped elements at the boundary are then adjusted using a variety of techniques [127] such as point insertion, edge/face flipping [128], smoothing [108, 109], and pillowing [129].

In some applications, for example, characterizing the complete electrical and mechanical behavior of the heart, the same label map may be the source of both a tetrahedral mesh for electrical simulations and a hexahedral mesh for subsequent computations of contraction and the two must be coupled to pass results between them [130, 131].

3.7 Boundary Conditions and Material Properties

Tissue types or, more generally, materials are defined in a mesh by assigning material properties to each element. For example, electrical simulations use the conductivity of each tissue while mechanical deflection problems need the modulus of elasticity of each material. The boundary between materials is an important interface because there is usually a sharp transition in material properties which can produce ill-conditioned matrices that are difficult to solve. One practice typically used to mitigate the associated numerical instabilities is to "smudge" or blur the boundary between these materials. Although the result is a system of equations that is easier to solve, the technique introduces errors, particularly when a sharp transition is a defining feature of the phenomena being modeled. The need to preserve sharp features and borders or to incorporate true discontinuities of material properties drive the need for meshing techniques that produce what are known as "boundary fitting" [123] material interfaces which accurately and smoothly represent the intended material interfaces.

In cardiac electrophysiology the gradients that arise at the tissue interfaces are very important to many conduction abnormalities. The interfaces between pathological tissue and heathy tissue are locations that are susceptible to arrhythmias and may even produce electrical currents, "injury currents," that can be detected on the body surface to diagnose the underlying pathology (see previous chapter). Hence, it is particularly important to model these interfaces correctly both from a physiological and a computational standpoint.

CHAPTER 4

BORDER ZONE APPROXIMATIONS USED IN BIDOMAIN SIMULATION OF MYOCARDIAL ISCHEMIA

4.1 Introduction

Myocardial ischemia is one of the leading causes of mortality in most Western countries [9] and affects approximately 6 million people in the United States alone. It is defined as a condition in which the metabolic demand of cardiac myocytes exceeds the supply of nutrients and oxygen received from the blood supply. In humans, myocardial ischemia arises primarily due to partially occluded coronary arteries, which supply the oxygen needed to metabolize energy in the tissues of the heart. The blood flow through the coronary arteries also provides a means of removing metabolic byproducts and thus sufficient blood flow is necessary to maintain healthy homeostasis. Heart tissue that is subject to complete ischemia (a full occlusion of a coronary artery or "myocardial infarction") for extended amounts of time eventually dies and becomes necrotic, or scarred, and prone to ventricular arrhythmias [45]. The limited ability of myocardial cells to survive for more than approximately one hour without adequate blood flow makes the disease not only deadly, but also very time sensitive, driving the need for rapid detection techniques.

To help fill this need for rapid detection, Electrocardiographic (ECG) based diagnostics methods are ubiquitously used to diagnose myocardial ischemia, however, their precision is limited. The ECG indicates acute ischemia from deflections of the ST segment. These deflections, whether elevations, or depressions, are indicative of injury currents that arise at the border of ischemic and healthy myocardium. While clinical interpretations indicate that there are pathophysiological differences between an elevation (ST elevated myocardial infarction, or STEMI), and a depression, (non-ST elevated myocardial infarction or NSTEMI), there is an incomplete understanding of the electrophysiological mechanisms that cause the two pathologies [46, 58, 59]. In the case of NSTEMI, the accuracy of ECG based diagnostic methods is especially inadequate, as low as 70% [47]. A mechanistic understanding of the factors that give rise to ST elevation and depression would improve the diagnosis of myocardial ischemia.

A first step toward understanding the mechanisms behind ST elevation and depression is a precise characterization of the injury current sources. Injury currents arise at the boundary of ischemic tissues because of heterogeneity in the membrane potentials between the relatively piecewise homogeneous ischemic and healthy myocardium. However, direct measurement of the transition from ischemic to normal potentials is challenging even in animal studies, often lacking the necessary spatial resolution. Consequently, there are few reports upon which to base realistic source models that include these boundary zones.

Simulation provides the most reproducible and controlled means of evaluating the impact of injury currents on electrocardiographic potentials but here, too, results are unsatisfactory. Simulations based on the bidomain approach in myocardial tissue [132] have been used to evaluate the relationship between acute ischemia and bioelectric potentials on the epicardial surface [40, 55, 56, 50, 54, 57]. While informative, these results have so far failed to establish a clear and unambiguous link between the locations of the ST depressions on the epicardium and the location or extent of the responsible ischemic zone(s) [40, 55, 56]. Most reports have concluded that more sophisticated models are needed, *i.e.,* those that include realistic heart geometry and physiologically accurate ischemic transmembrane potentials, to better represent the distribution of epicardial potentials during ischemia [56, 55].

A particular feature of simulations of acute ischemia, and possibly a major source of error, is the precise spatial representation of the border zone between ischemic and healthy myocardium. Realistic heart models of ischemia include three distinct regions: an ischemic region embedded within healthy myocardium separated by a border zone [40, 55, 56, 50, 54, 57]. Advances in cardiac imaging allow for excellent descriptions of the heart geometry as a whole, but no imaging modality captures with the necessary submillimeter precision the region between the diseased and healthy tissues, especially in the setting of acute ischemia, in which the ischemic conditions are dynamic and the location of the border zone unstable. Medical imaging modalities are not sensitive to the metabolic or electrical changes that arise during acute ischemia but rather depend on the structural changes that arise only after myocardial infarction and scar formation. Only functional imaging using intramural potential recording techniques are capable of capturing acutely ischemic regions and their spatial resolution is generally limited to multiple millimeters [51]. Perhaps as a result of these limitations in imaging, border zones have been represented simplistically in previous models of acute ischemia. However, as we will show, the configuration of the border zone in a model of acute ischemia can have profound impact on the resulting cardiac potentials, thus demanding very careful choice of assumptions.

A general limitation of previous simulations of acute ischemia has been in the shape and location of the ischemic regions. Rather than using measurements from experiments, researchers have typically defined the shape of the ischemic region and border zone based on a highly simplified notion of the pathophysiology of the disease. Generally, the ischemic zone has been modeled as a prism or trapezoidal region that has a wider base at the subendocardium and extends transmurally toward the epicardium with an extent representative of the degree of ischemia [56, 50, 54, 55]. In this formulation, the ischemic region contains homogeneously depressed membrane potential amplitude and the border zone is relatively thin (3 mm or less) with a transmembrane voltage that varies smoothly and often linearly between ischemic and healthy regions. The basis for the shapes employed comes not from experiments with induced acute ischemia, but rather from postmortem studies of infarcts. This approach assumes that regions of what becomes scar and fibrosis correspond precisely to the acute ischemic zones [133]. Acute ischemia, however, is a dynamic condition, depending on local conditions of supply and demand and levels of perfusion. As a result, the boundary may be constantly shifting and the border zone could be expected to vary in its thickness and in the local values of the transmembrane voltage [134].

The goal this study was to examine the consequences of a range of assumptions about the ischemic border zone and to compare computed and measured epicardial potentials under these assumptions. We have created subject specific models from ischemia experiments that allow direct comparison with measurements. Rather than fixing the border zone, its parameters were adjustable and were varied to reproduce the measured epicardial potentials. Postmortem MRI and diffusion tensor imaging (DTI) scans provided the basis for geometric models of the whole heart, while measurements of ST potentials from the same hearts using up to 450 transmural electrodes determined the location of ischemic regions. In this way we could define ischemic zones based on electrical recordings, albeit with less spatial precision than the medical imaging of the whole heart.

Using a model that only consisted of the three traditional regions—ischemic zone within an otherwise healthy heart separated by a standard border zone—it was not possible to reproduce measured epicardial potentials. To account for heterogeneity of potentials in a more realistic border zone, we added an additional region between ischemic and healthy tissues that represented partial ischemia. In this way, the fully ischemic region transitioned smoothly to a less ischemic region and then to the healthy tissue using a much sharper transition. This more complex arrangement produced epicardial potentials that were much closer to those measured in the experiments. These simulation results coupled with our high resolution extracellular potential measurements indicated that the commonly used simplification of the electrical boarder zone was not sufficient to reproduce accurate injury currents in our subject specific model and that a more sophisticated approximation was required.

4.2 Methods

To achieve our goal of evaluating the role of the border zone in the generation of electrocardiographic fields from acute myocardial ischemia, we carried out both experimental and subject specific simulation studies based on the same animal models. Recordings of extracellular potentials at high resolution from both the epicardial surface and a part of the myocardial volume provided detailed electrical images while high field MRI was the source of anatomical images from which we created the subject specific geometric models. Simulations were based on the bidomain technique implemented in a finite element formulation.

4.2.1 Experimental Preparation

We induced controlled episodes of acute regional myocardial ischemia in an open chest canine preparation by cannulating the left anterior descending (LAD) artery and adjusting the flow of blood with a digital rotary pump routing blood from one of the carotid arteries. To increase metabolic demand, we paced the heart from the right atrial appendage using a bipolar clip electrode with a pacing interval set to span the full range of values that was capable of capturing the heart. Gas anesthesia, artificial ventilation, and monitoring of arterial blood gases according to a protocol approved by the University of Utah Institutional Animal Care and Use Committee ensured a humane and stable preparation. Electric measurements were by means of an 247-electrode sock placed around the ventricles of the heart and up to 45 fiberglass plunge electrode needles with 10 electrodes per needle placed through the anterior aspects of the left and right ventricles to cover a volume that included both ischemic and normoxic regions. Time signal (electrogram) acquisition was by means of a 1024 channel recording unit with a 1 KHz sampling rate and 12-bit resolution. After inserting the needles, 1 hour was given for the preparation related injury currents to subside. The set of LAD flow rate values used included 23 ml/min, 16 ml/min, and 9 ml/min, while the heart rate pacing interval was reduced from 380 ms to 230 ms by increments of 30 ms for every flow rate. Recording occurred in epochs of 5 seconds captured approximately every 30 seconds beginning from before onset of each ischemia protocol and continuing throughout the ischemic period and for 5 minutes after restoration of normal flow.

4.2.2 Geometric Model Creation

Upon sacrifice of each animal, the excised heart was scanned with a 7 Tesla small animal scanner (BioSpec from Bruker Corp) for an anatomical scan with approximately 450 micron resolution in all directions and a diffusion tensor imaging (DTI) scan to identify the fiber directions [135]. Needle and sock electrodes were digitized and registered to correspondence points in the MRI scans. The software package Seg3D [19] was used to segment heart tissue using thresholding and water-shedding algorithms as well as manual fine adjustments. To convert the segmentations into smooth polygonal surface models, we used the SCIRun simulation environment [136], specifically, Marching Cubes and Taubin mesh fairing [137] algorithms. The Biomesh3D [138] and Tetgen [139] packages then converted the surfaces into boundary conforming, tetrahedral meshes containing approximately 1.5 million elements. The DTI imaging provided a means to estimate local myocardial fiber orientation, which was mapped to the geometric model.

A key aspect of the geometric model was the border zone between healthy and ischemic zone, which was the focus of the study. To define the ischemic zone, we first interpolated the measured electrograms from the intramural needle electrodes and then defined a threshold for the ST-segment potentials, which are well known to deviate from their baseline values during ischemia [140]. Interpolation of the electrograms from the needle electrodes was based on a volumetric Laplacian smoothing [141]. The ischemic border zone corresponded to an isosurface of the reconstructed ST-segment potential distribution at an elevation two standard deviations above baseline conditions, approximately 11 mV. We chose a time instant at 40% of the duration of the ST-segment based on the root mean squared (RMS) of all the recorded electrograms during a single, representative beat captured during the intervention. To establish the sensitivity of the results to the selection of the time point during the ST segment, we repeated all analyses with potentials measured at 30% and 50% of the ST-segment duration with insignificant variations.

4.2.3 Simulation

The goal of the simulation was to compute epicardial potentials based on a fixed ischemic zone but variable border zone assumptions and then compare the results to measurements from the same heart under the same conditions. The numerical approach for these simulations was based on a static bidomain approximation [54, 49] described by Equation 4.1

$$\nabla \cdot (M_i + M_e)\nabla\Phi_e = -\nabla \cdot M_i \nabla\Phi_m, \tag{4.1}$$

where M_i and M_e are intracellular and extracellular anisotropic conductivity tensors and Φ_e and Φ_m are the extracellular and transmembrane potentials. The transmembrane potential is equal to the difference between the intracellular and the extracellular potentials ($\Phi_m = \Phi_i - \Phi_e$). For ischemic regions, this difference was set at -30 mV in accordance with previous studies [54]. In order to compare the measured voltages to the simulated voltages, it was necessary to ensure that both sets of voltages were reported relative to the same reference potential. The reference potential of the simulated voltages was adjusted to match that of the measured voltages by integrating the potentials over both data sets and subtracting the difference. All simulations were implemented in the SCIRun problem-solving environment [136], which solves differential Equation 4.1 using a finite element method [142]. The normalized conductivity values came from a computational approach by Stinstra *et al.* [49] that took ischemic conditions into account. For convenience, all ratios were normalized to an extracellular longitudinal conductivity, σ_{el}, of 1 as seen in Table 4.1.

4.2.4 Modeling of Border Zone

The hypothesis of this study was that the configuration of the border zone, *i.e.,* the profile of the transmembrane potential between healthy and ischemic regions, can have profound impact on the computation of epicardial potentials. To provide a flexible, parameterized description of the potentials across the border zone, we used a Gaussian blurring approached base on the following equation:

$$G(t) = 30e^{\frac{-t^2}{2\sigma^2}}, \tag{4.2}$$

Table 4.1: Bidomain normalized conductivity values. In the bidomain simulations, only the conductivity ratios change the calculation of the electric field, thus, for convenience, all ratios were normalized to an extracellular longitudinal conductivity, σ_{el}, of 1.

	Healthy	Ischemic
Intracellular longitudinal conductivity	1	1
Intracellular transverse conductivity	0.05	0.05
Extracellular longitudinal conductivity	1	0.5
Extracellular transverse conductivity	0.333	0.25

where $G(t)$ is the potential at distance t starting from the thresholded boundary (edge of the ischemic region) and moving towards the healthy myocardium. The variance of the Gaussian distribution was the variable that controlled the overall width of the border zone. This methodology of defining a Gaussian border zone is what is traditionally found in the literature and will be referred to in this manuscript as a “simple” border zone. As a proposed alternative to this simple border zone, we explored a more complex profile representing the transmembrane potentials as four regions rather than three (ischemic, transition, border, and healthy). Figure 4.1 shows the two models; the key differences are the addition of a transition zone, (TZ) which was also modeled with a Gaussian function but with a much larger variance, and a truncation of the border zone, essentially creating a two-phase zone, with each phase showing a different spatial potential gradient. When the transition region was included in the model, it spanned across what was defined in the simple border zone as the boundary of the ischemic and border zones. The start of the transition was offset into the ischemic region a fixed distance which was optimized from the data. Whereas the location of the border zone was determined by shifting the Gaussian function such that the complex border zone terminated at the same location as the simple border zone as seen in Figure 4.1.

4.2.5 Computation of Transmembrane Potentials

The overarching goal of this study was to evaluate approximations of transmembrane potentials during acute ischemia, particularly in the border zone, used in bidomain simulations. Our unique measurement arrangement of capturing both the epicardial potentials and the intramural potentials within the ischemic region provided for two different means of evaluating these approximations. First, we constructed a model of ischemia based on the measured ischemic zone and an imposed distribution of transmembrane potentials through the border region to calculate epicardial potentials, as described above. The input to the simulation then becomes a **measured spatial description** of the ischemic region and an **assumed or imposed transmembrane potential transition** through the edges of the ischemic region. The output was the set of extracellular potentials on the epicardial surface.

However, the same bidomain equation 4.1 can be rearranged to directly solve for Φ_m from the measured Φ_e, which provided a means of testing our assumptions about the effects of ischemia on transmembrane potentials. Here, the input to the simulation was the set of **measured extracellular potentials,** Φ_e from the intramural needles. In this formulation, there is no assumption about the spatial distribution of the transmembrane

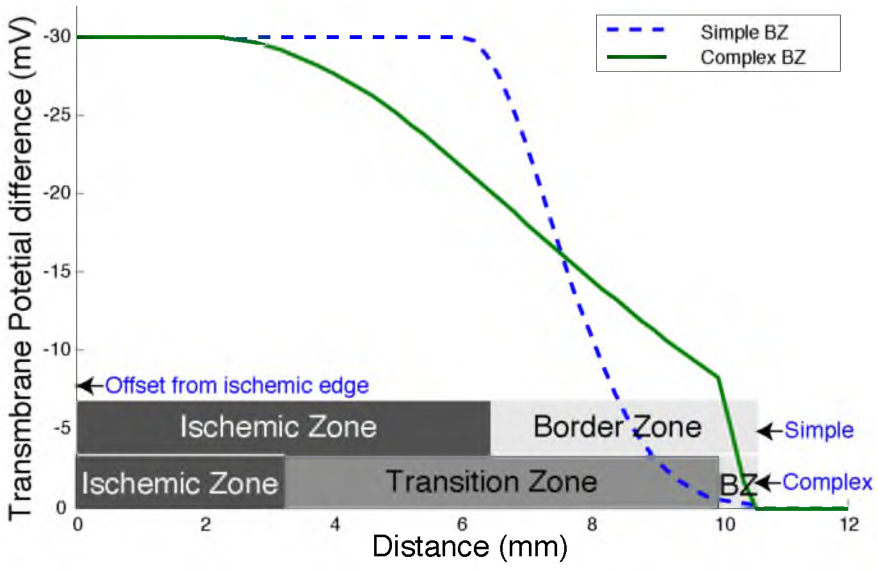

Figure 4.1: Potential profile across border zone. The schematic illustrates both the simple and complex methods for defining the border zones where dashed blue line (simple BZ) shows the transition from -30 mV transmembrane potential to 0 mV using a Gaussian function with a variance of about 3. The green solid line (complex BZ) shows a gradual transition region along with a sharp border zone. The x-axis is the distance in mm from the center of the border zone.

potentials. Instead, the output of the simulations are the resulting Φ_m which we refer to as the "computed transmembrane potentials." These potentials were compared directly to the assigned approximation of the transmembrane potentials used in the first model.

To carry out this comparison of the computed transmembrane border zone profile with the approximated profile, we sampled the computed transmembrane potentials as a function of distance along lines that ran from the fully ischemic region to the healthy region of the heart. The trajectory of these lines was normal to the surface bounding the fully ischemic tissue and these lines were sampled at increments of 200 microns, as illustrated in Figure 4.2. We examined these profiles separately and also as averages created across manually selected regions with similar profiles and as a single average that included all the profiles, as described by the equation

$$\bar{\Phi_p}(n) = \frac{1}{m}\Sigma_{i=0}^{m}\Phi_{i,n}, \tag{4.3}$$

where $\Phi_{i,j}$ is the potential at point j of profile i, as indicated by the points $P_{i,j}$ in Figure 4.2.

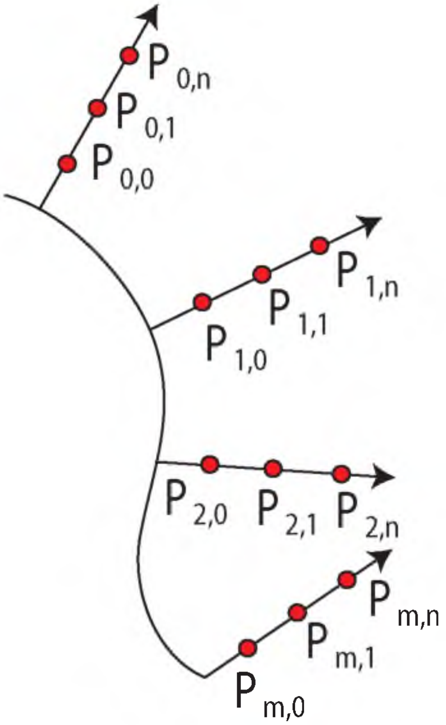

Figure 4.2: Diagram of the border zone profile calculations. The electrical potential was sampled normal to ischemic boundary, indicated by the solid curving line, such that it could be evaluated as a set of spatial profiles and then averaged across all profiles.

The precision of the computed transmembrane potentials clearly depends on the quality and especially the spatial sampling density of the intramural electrode measurements. The resulting field may be overly smoothed due to the interpolation across an undersampled border region, though the use of the "wave equation based" interpolation method [143, 141], which incorporates assumptions specific to the spread of activation, mitigates such errors. To address this concern, a second method was implemented to assure that the calculations were not biased by the sampling density. In this method, calculated transmembrane potentials were only considered directly at the electrode locations, eliminating any errors from interpolation. However, it was no longer possible to calculate a profile of the transmembrane potential through the border zone. Instead, each calculated transmembrane potential was plotted as a function of distance from its associated electrode to the boundary of the ischemic region. In this way a statistical profile was calculated for the transmembrane potential as a function of distance.

4.3 Results

In the following sections are the results describing how we identified and approximated the border region in our bidomain simulations. They also include the sensitivity of the simulation to changes in the border zone width and the effects of including a transition region. The last section shows the computed transmembrane profiles across the border zone which can be compared to our approximated profile.

4.3.1 Approximation of the Ischemic Region

The motivation for adding a second component to the border zone approximation came from our inability to match the observations of the measured epicardial potentials using only the simple border zone. In these measurements the elevated extracellular potentials in the center of the ischemic region transitioned smoothly to those in the healthy tissue–there was no evidence of two distinct regions, such as what is used in the simple border zone approximation where the border zone is a simple transition from one homogeneous region a second homogenous region. Instead, we found that there were gradients even within the ischemic region which required one type of transition and a second transition was needed to model the border zone. Both transitions in the transmembrane profile were necessary in order to achieve in the extracellular space both a smooth gradient in the ischemic region flanked by distinct negative regions.

Figure 4.3 shows the measured and interpolated ST-40 potentials from the needle data

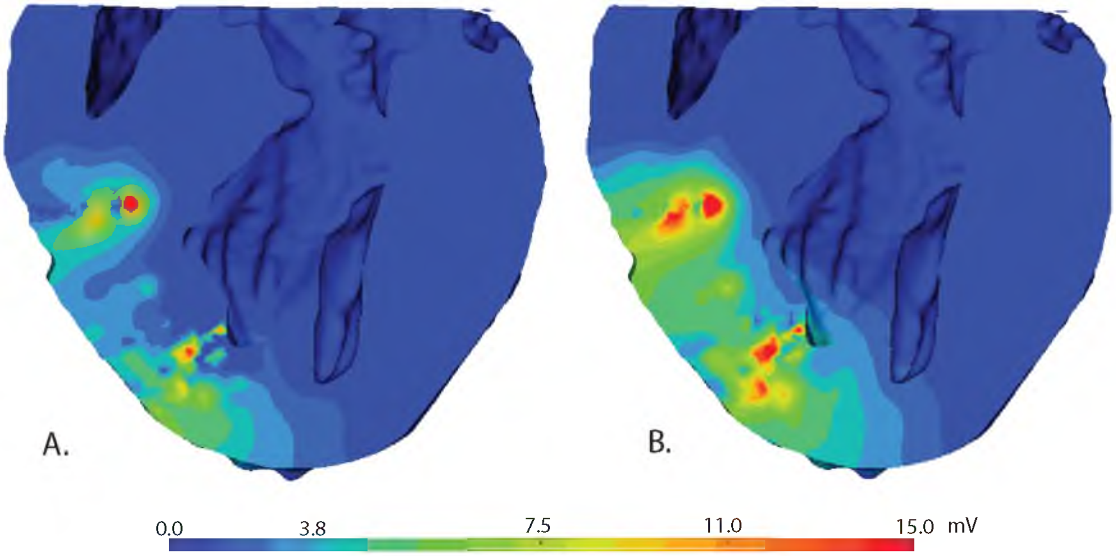

Figure 4.3: Measured ischemic potentials. A. Shows an early stage of ischemia just becoming transmural. This corresponds to a flow rate of 16 ml/min and pacing interval of 320 ms. The scale was truncated at 11 mV to better highlight the region considered ischemic. The maximum extracellular potential was 18 mV. B. Shows a fully developed ischemia corresponding to a period later in the same ischemic episode with a flow rate of 16 ml/min and pacing interval of 230 ms. The maximum extracellular potential was 26 mV.

at two different stages during the same ischemic episode. For this experiment, we defined an ischemic threshold potential of 11 mV, over the baseline value. The resulting isopotential surface represented the outer boundary of an ischemic region. Under the assumptions of the simple border zone, this also formed the inner surface of the surrounding border zone, the origin of the Gaussian function described above. Under the assumptions of the two-phase or complex model, the added transition zone (TZ) extended back into the ischemic region 10 mm from this isosurface.

4.3.2 Border Zone Sensitivity

The major goal of this study was to compare measured epicardial potentials with simulated values based on measured ischemia zones and a subject specific geometric model. By replicating all other parameters of the experiments in the simulations, we were able to isolate the role of the border zone in the simulations, treating border-zone parameters as free variables. We then varied these parameters to establish their impact and then attempted to identify values that generated accurate epicardial potentials. For this sensitivity study, we used the simple border zone approximation in which the key parameter that controls the thickness and potential profile of the border zone is the value of the variance assigned the Gaussian distribution.

The selection of the border zone width had a highly nonlinear impact on the amplitude and the distribution of the epicardial potentials. For example, for a border zone with variance less than 2, sharper than the blue curve seen in Figure 4.1, the maximum elevation and minimum depression on the epicardial surface were highly sensitive to changes in the border zone as seen in Figure 4.4. A variance of 2 corresponded to a border zone width of about 3 mm, which is commonly used in bidomain models of ischemia. The resulting sharp transition produced depressions that were localized at the edges of the border zone. In contrast, the smoother transition of the border, for example, with a border zone width of 10 mm, created depressions that were diffused across a larger area that was not specifically localized over the border zone. The diffused and acute voltage depressions resulting from the width of the border zone are shown in Figure 4.5.

4.3.3 Matching the Simulation with the Experimental Data

To simplify the presentation of the results we divided the simulations into three groups: narrow border zones (less than 3 mm), wide border zones (10–15 mm), and simulations with transition regions (10 mm) and a sharp border zones (3 mm). The simulations performed with a narrow border zone showed regions of steep epicardial potential gradients located approximately above the subepicardial ischemic zone that were not replicated in the

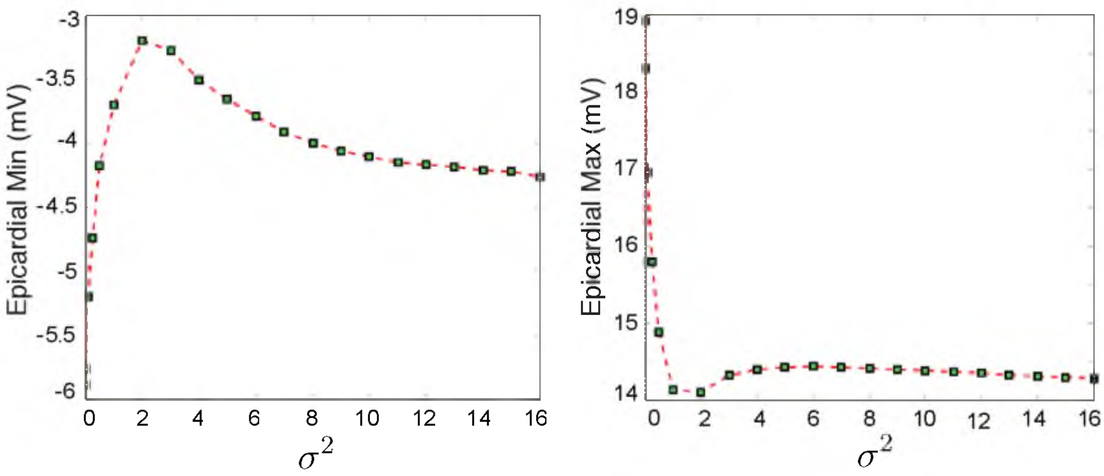

Figure 4.4: Simulated maximum and minimum epicardial potentials. The graph on the left shows the minimum epicardial potential predicted from the simulation as the border was varied based on the variance of a Gaussian distribution. The right-hand graph is the corresponding maximum epicardial potential

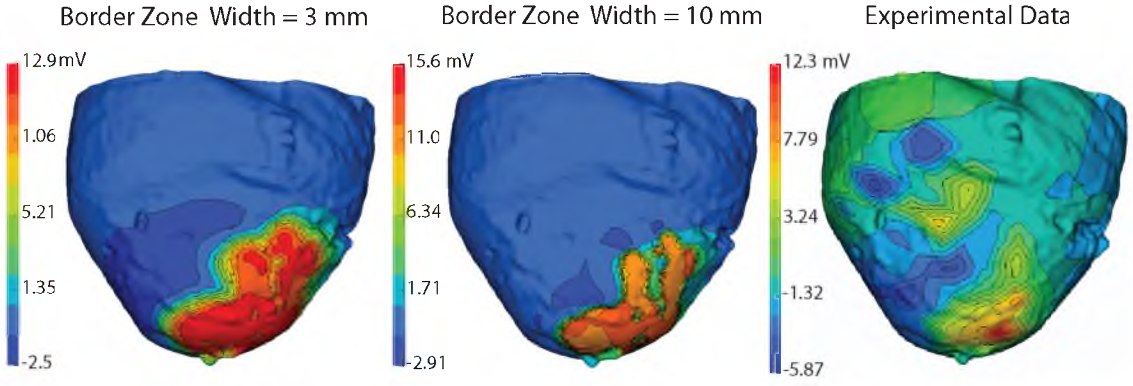

Figure 4.5: Simulated ischemic regions compared to experimental data. The row of the figure shows simulations of epicardial potentials for a nontransmural ischemic zone with both a sharp border zone (left) and a smooth border zone (middle) compared to the experimental data (right).

experimental data, as seen in Figure 4.5. Wider border zones produced less severe gradients over the ischemic region than did the narrow border zones, but also produced homogeneous epicardial potential elevations. The amplitude of the ST elevations was also lower with the wider border zones than with the narrow but was still higher than experiments for the nontransmural ischemia stage. The relation of amplitudes reversed in the case of transmural ischemia with the experimental maximum values 18% and 9% higher than the simulations with wide and narrow border zones, respectively.

The third set of simulations, which used a transition zone as well as the border zone, resulted in field gradients that were closer in magnitude and distribution to those in the measured data. Figure 4.6 shows a simulation that included a transition region of 10 mm and a border zone of 3 mm. Not unexpectedly, the simulated epicardial potentials were generally smoother than the measured values; they were derived from ischemia sources that were, themselves, smoothed and also truncated by the limited resolution and coverage of the needle electrode measurements.

4.3.4 Computed Transmembrane Potentials

In addition to approximating the transmembrane profile across the border zone, we were able to use the bidomain equation, 4.1, to directly solve for the transmembrane potentials from our experimentally recorded extracellular potentials. The mean profile across all the lines normal to the ischemic boundary is shown in Figure 4.7. Figure 4.8 shows similar profiles but computed for 8 different regions selected from the full border

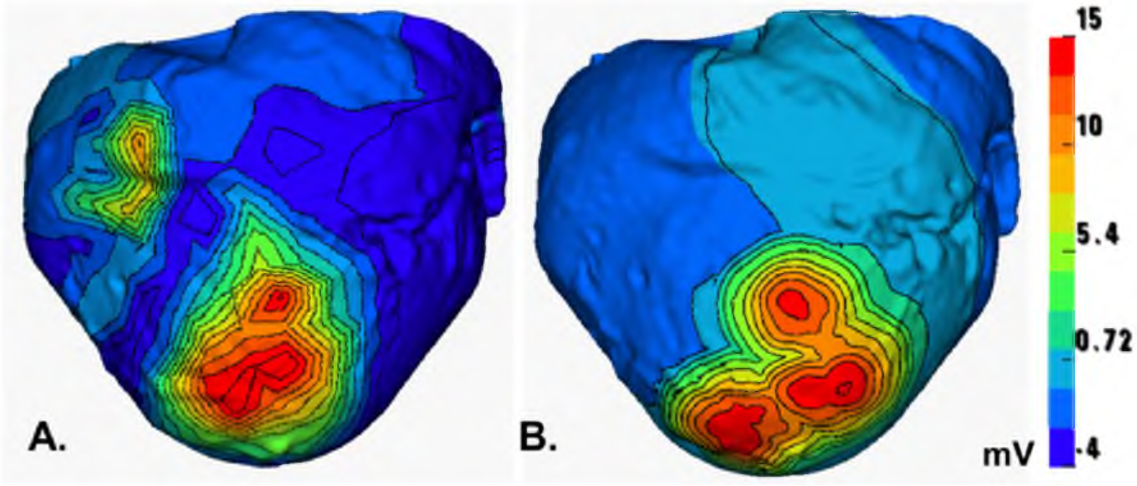

Figure 4.6: Measured versus simulated epicardial potentials using a transition region. A. Shows measured extracellular potentials during the ST segment of an ischemia protocol. B. Shows the simulated epicardial potentials from a subject specific model that corresponds to the same time point as the measured data, *i.e.,* that is based on the same ischemic volume source.

zone. Profiles from lines that ran in the transmural direction (normal to the epicardial surface) showed sharp transitions, *e.g.,* Regions 7 and 8 in Figure 4.8. Conversely in the axial and transverse directions (tangent to the epicardial surface), there appeared to be regionally heterogeneous distributions of gradients within the border zone (*e.g.,* Regions 1, 2, and 3 in Figure 4.8). The spatial organization of the different profile types (smooth vs. abrupt) varied from experiment to experiment and did not appear to have any relation to local fiber orientation as determined from diffusion weighted MRI. It is also important to note that the threshold between the ischemic zone and the border zone was determined experimentally from extracellular potentials to be approximately 11 mV. This corresponded to a transmembrane potential of -22 mV, *i.e.,* all transmembrane values above 22 mV fell within the ischemic zone.

As another approach to representing the profile of the potential across the border zone, we computed the transmembrane potentials at the locations corresponding to the measurement sites of the needle electrodes. We then computed the average potential for all the nodes at the same distance, within a prescribed delta, from the surface of the ischemic zone and plotted the results as a function of this distance, similar to a kernel regression. Figure 4.9 contains an example of such a plot.

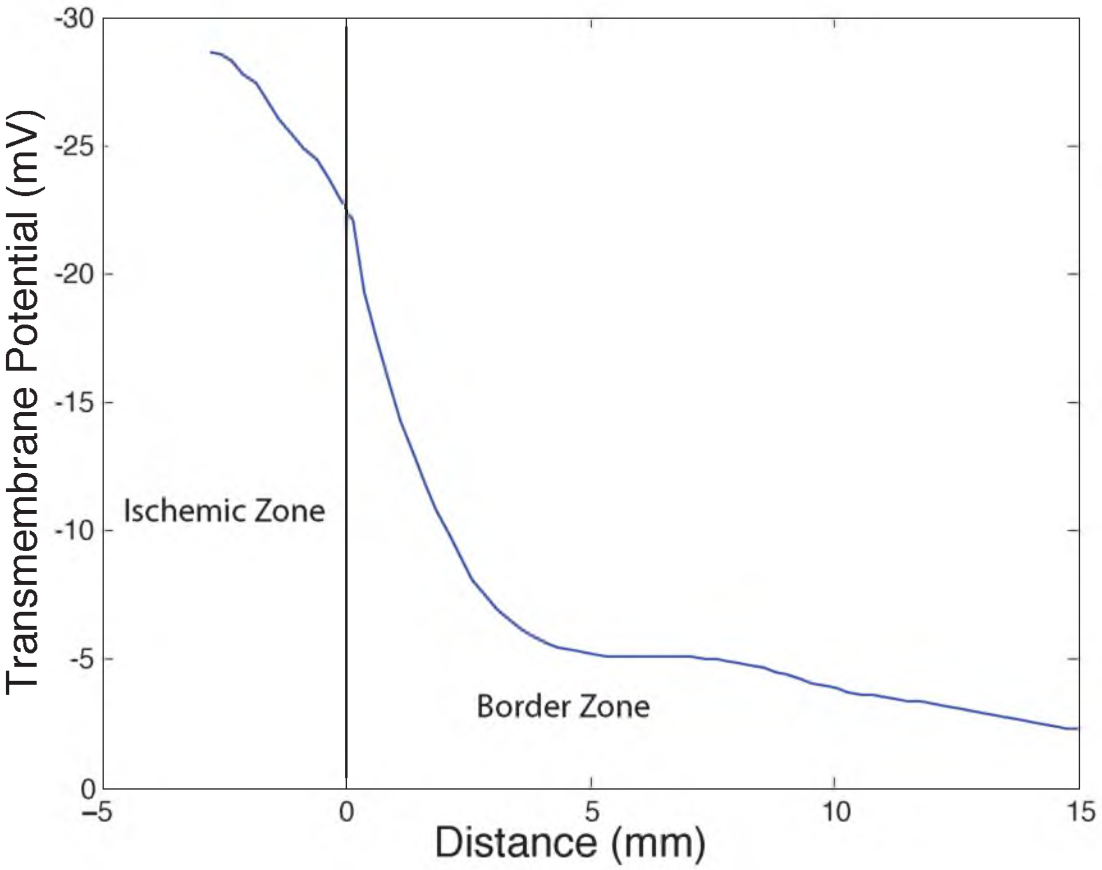

Figure 4.7: Mean transmembrane potentials calculated from plunge needle recordings. The transmembrane potentials were calculated from the recorded extracellular potentials. The graph shows the mean potential distribution normal to the border zone.

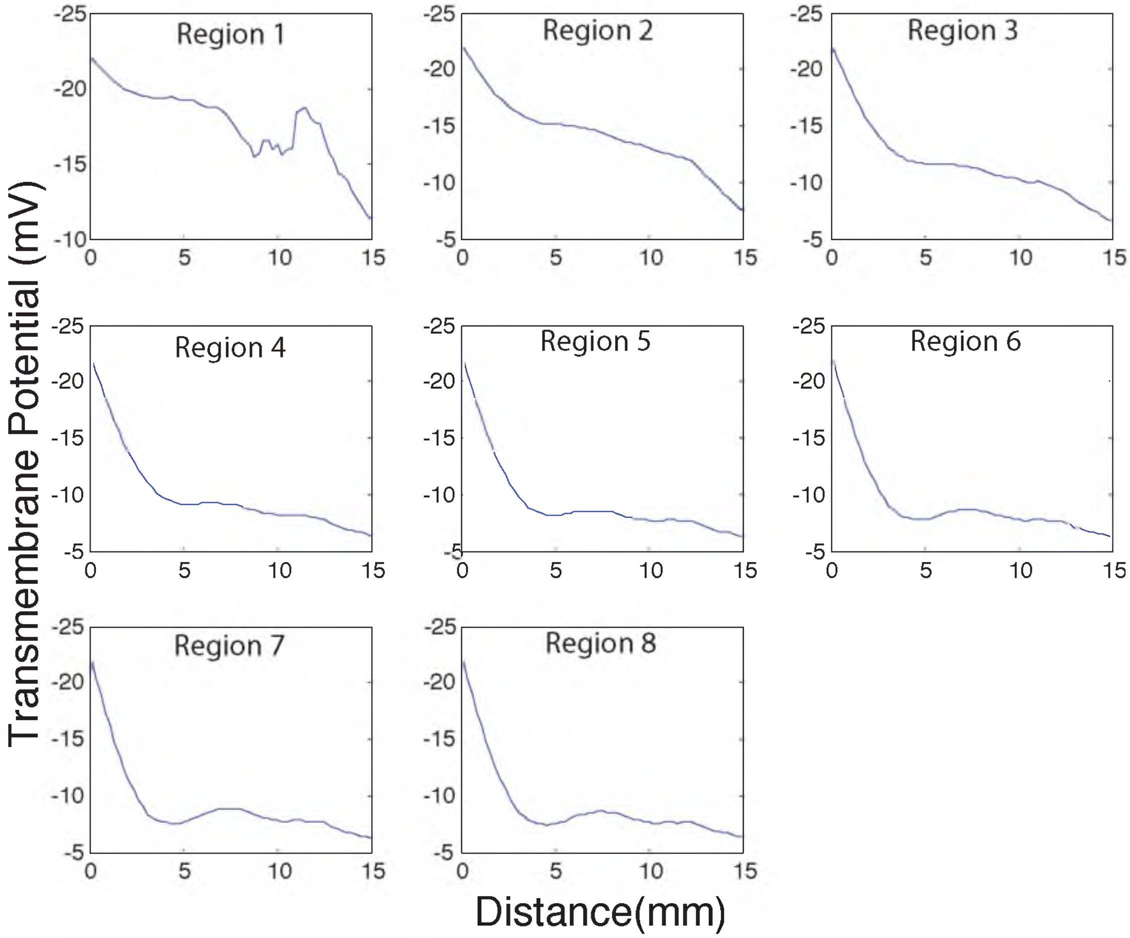

Figure 4.8: Regional variation of border zone profiles. The plot divides the border zone profile into 8 distinct regions that exhibited relatively homogeneous border zone profiles. Both sharply and smoothly varying border zones were seen across different regions.

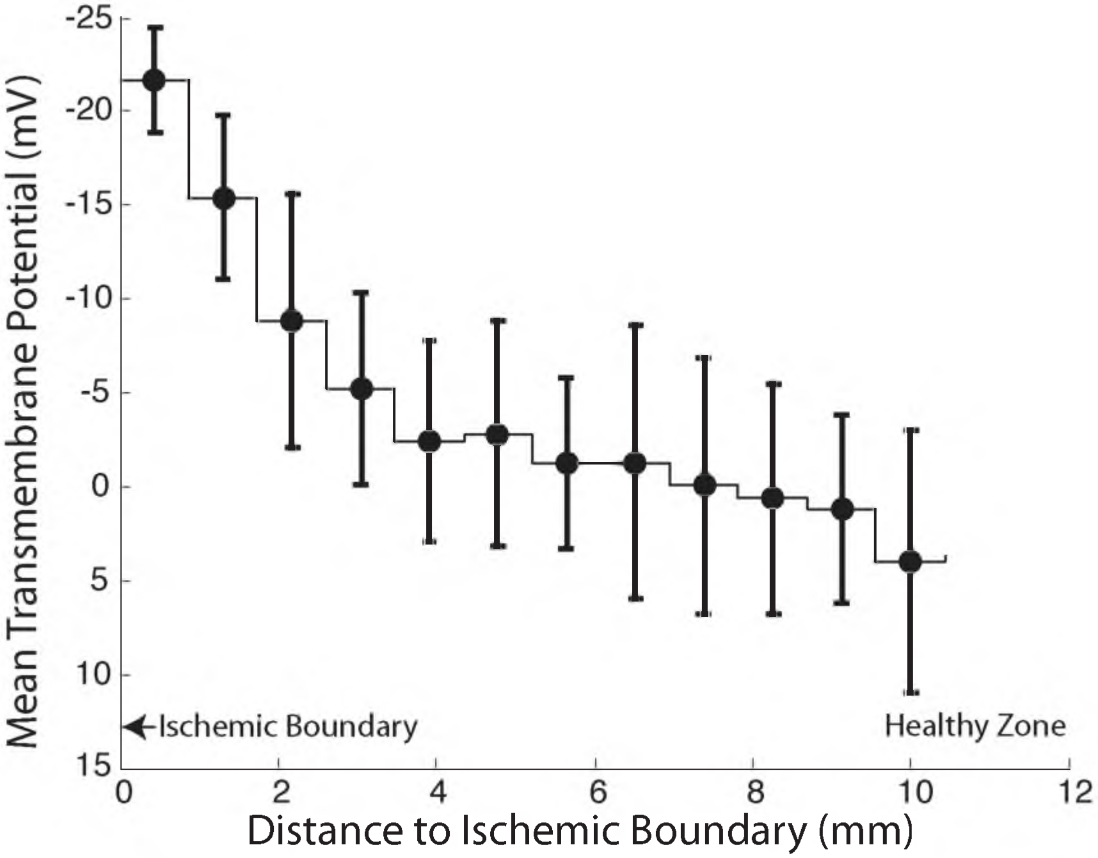

Figure 4.9: The calculated transmembrane potentials at electrode locations as a function of distance from the ischemic boundary. The transmembrane potentials at the electrode locations were binned into groups as a function of distance. The square dots indicate the mean value of the bin along with standard deviation bars. The solid line shows the width of each bin.

4.4 Discussion

The goal of this study was to examine the typical assumptions about the border zone between healthy and ischemic myocardium, making use of simulation and measurements from a highly instrumented animal heart. Measurements of this region are challenging as they require a dense array of electrodes to probe at millimeter or better resolution a very specific volume of the heart (the ischemic border zone) without *a priori* knowledge of its location. An additional challenge is that the boundaries of the ischemic region change dynamically as they are a complex function of perfusion and metabolic need. We used measurements from intramural needle electrodes to identify within a few millimeters the region of ischemia, captured simultaneously the associated epicardial potentials, and then used post mortem MR imaging to create a detailed geometric model of the anatomy of the same heart. From these elements, we created a modeling framework that allowed implementation of different border zone assumptions and then a comparison between the computed and measured epicardial potentials. The degree of agreement between these potentials on the cardiac surface became the figure of merit in evaluating the accuracy of the modeling assumptions.

4.4.1 Approximation of the Ischemic Region

A novel feature of this study was the use of intramural needle electrodes to establish realistic and subject specific boundaries for the ischemic zone. The location, shape, and continuity of the ischemic zones reconstructed from the plunge needle electrodes varied significantly from the ischemic zones seen in simulation studies reported in the literature [56, 50, 54, 55]. Most simulations assume that the ischemic region is one continuous group of similarly ischemic cells and that nontransmural ischemia occurs in regions anchored to the endocardium. In contrast, the data from our experiments typically showed a small central region of maximum ST segment potential elevation that gradually transitioned to lower elevations and eventually to normal levels. This gradual transition made it difficult to define a discrete border zone that narrowly separated the ischemic zone from surrounding well perfused tissue. The locations of the ischemic zones also varied from the endocardium, a finding based on numerous experiments and reported elsewhere[51].

This fundamentally different idea of the transition of extracellular potential within an ischemic region and border zone was not only important to the understanding of ischemia, but also to research regarding the simulation and mechanistic exploration of arrhythmias. The heterogeneity of conduction seen in the border of infarcts and ischemic regions is thought to be a major factor in the development of reentrant circuits. In infarcted tissue that has healed to form more or less patchy scar, this heterogeneity appears to be localized to a very narrow border, whereas ischemic regions appear from our results to have much larger regions of continuously varying electrical heterogeneity. The larger scale of the heterogeneous behavior is important because reentrant propagation is dependent on both the speed of conduction and the path length of any activation wave front that cycles back to encounter sufficiently recovered tissue. Large regions of compromised conduction would cause conduction slowing and create larger areas for reentrant circuits to form. These observations may provide insight into the conditions that create well characterized early vulnerable periods to arrhythmias and sudden death following acute ischemia [144, 145].

4.4.2 Border Zone Sensitivity

Varying the border zone width and profile showed that the simulated epicardial potentials were highly sensitive to the rate of transition of membrane potential. Previous simulations [56, 55, 40] have failed to match the potential distributions seen in experimental data, a finding largely attributed to the anisotropy ratios chosen in the bidomain models. However, our results indicate that the border zone width and profile are important factors in determining the magnitude and shape of the elevations and depressions of ST segments on the epicardial surface. Sharper border zone transition regions produced more localized and severe depressions. Sharp transitions were not only a function of the explicitly modeled border zone width, but also could arise due to geometric discontinuities such as corners [146]. In fact, any feature in the ischemic source or the border zone that produced a sharp transition had a significant affect on the epicardial potential distribution. This finding suggests a source of artifact in any simulation that uses geometry with sharp corners, such as rectangular or rectilinear ischemic zones, which are obviously very approximate, but also may lead to disproportionately large errors just because of their sharp features.

We were unable to match the measured epicardial potential distribution with simulated values using the traditional, linear varying, or even Gaussian blurring of a single border zone regardless of border zone width. This finding, along with the absence of a distinct ischemic border in the measured needle electrode data, led us to propose and evaluate an additional transition region in the bidomain model. Inclusion of this transition region created epicardial field gradients similar to those seen in measurements with in the ischemic region itself. However, the transition region did not reproduce the localized depressions that flank the ischemic region seen in the experimental data. It was found that a combination of a transition region in conduction with a sharp border zone produced the most realistic gardens 1 mV/mm within the ischemic zone while still producing very localized depressions. We do not assume that our solution is unique, but is one possible distribution that led to more accurate simulations.

A source of uncontrolled error in the simulations was the assumption that our needle-electrode recordings captured all the relevant ischemic regions. The measured epicardial potentials reflect the integral of all ischemia sources while the simulated equivalents were based only on the ischemic zones detected within the volume spanned by the needle electrodes.

4.4.3 Computed Border Zone

Our findings, both experimental and simulation, suggest that to capture the role of the border zone in electrocardiography requires a more complex description than has been reported to date. Moreover, our findings suggest that even relatively minor alterations in the border zone produce substantial changes in epicardial potentials. Using the measured extracellular potentials to estimate the transmembrane potentials we found both sharp and smooth potential transitions across the borders, depending on the orientation of border relative to the heart surface. The computed border zone did not completely agree with any of the approximated versions, even those that produced very reasonable simulated epicardial potentials. In particular, a large regional heterogeneity existed in the computed electric potential gradients, which was independent of the conductivity anisotropy, suggesting the existence of an additional feature missing from the model, perhaps the underlying microvascular structure.

There is considerable indirect evidence to support our simulation based observation that the border zone is broader than typically assumed and is highly nonlinear in space. Results from Johnson *et al.* [134] suggest that the distribution of potassium ions across the border zone in ischemic hearts is highly variable based on location, further supporting the idea that the transmembrane potential across the border zone would be similarly heterogeneous. An important limitation of all reports studies of the distribution of ions within the border zone is the poor sampling resolution across the border zone [147, 148, 149]. While there are important differences from the setting of acute ischemia, findings from healed infarctions also provide evidence to support the suggestion of large heterogeneity of the border zone. These studies suggest that the border zone, while very narrow (2-3 mm), comprises interdigitation of necrotic and healthy cells forming very complex conditions for spread of activation [150] and even very thin islands of healthy cells within the necrotic regions [151]. Such findings suggest a common feature of both acute and chronic settings of a supply of nutrients and oxygen that is very heterogeneous across this region.

4.4.4 Clinical Implications

This study was driven by experimental findings in a canine model of acute ischemia, in which collateral circulation is known to produce responses different from human hearts. However, the fundamental electrocardiographic principles are the same across species and so there is an opportunity to identify implications of these results to clinical diagnostic use of the ECG in the setting of acute ischemia. ST-segment depression in the ECG is thought to signify early stages of ischemia. However, many aspects of the mechanisms of ST segment depression and elevation remain unclear. In order to characterize the bioelectric source of ischemic potentials, we (as others before us) have focused attention on the heart and left the generation of associated body-surface potentials as a separate problem. Body-surface potentials are uniquely and linearly determined from epicardial potentials [152] so that the fundamental links between myocardial source and extracardiac signal can be addressed based on epicardial potentials.

Experimental studies have produced conflicting results in determining the cause of the potential depressions seen on the epicardial surface [40, 57, 54]. A persistent challenge has been to achieve reproducible nontransmural ischemia across subjects. One consequence has been consistently poor correlation between the location of the elevations and depressions relative to the ischemic region in early stages of ischemia. In addition to the experimental studies, computational models have been used to reproduce epicardial depressions, but in general their results correlate poorly to experimental or clinical data [57]. In our studies, as the border zone width was increased, the amplitude of the depressions decreased and the depressed regions were spread out over a much larger region. At very large border widths, it was difficult to identify any regions of depression on the epicardial surface making it improbable that depressions would be detectable on the torso surface. In contrast, a narrow border region produced very focal depressions with large amplitudes that might well project to the torso surface. For this reason, we conclude that to accurately model the distribution of elevations and depressions on the epicardial surface simulations must include accurate representations of complex border regions. Previous research has not considered border zone heterogeneities as a possible explanation for the confounding results often seen in epicardial potential distributions.

These findings lead to the natural extension of our model to be used in electrocardiographic inverse problems in which the objective is to localize the ischemic source potentials within the heart based on measurements from the torso surface. [153, 154] The inverse problem in this setting is highly underdetermined and many solutions satisfy the mathematics of the problem. One solution is to place additional constraints upon the nature and distribution of source potentials in the heart. Our findings that the border of the ischemic region contains heterogeneous gradients and strongly influences the location and magnitude of the depressions and elevations on the epicardial surface could be used to improve the constraints used in the inverse problem.

Subject specific modeling of acute ischemia validated against measurements of epicardial potentials has revealed a gap in our understanding of the electrical consequences of myocardial ischemia. It appears that the border zone between healthy and ischemic tissue is a vital parameter in understanding and simulating the injury currents that arise during an ischemic episode. Measurements and simulations support the assertion that the border zone is complex and consists of both sharp and smooth electrical potential profiles which help dictate the epicardial surface potential distributions and presumably the torso potential distributions as well. Additional studies are needed to explain why this heterogeneity arises and how it can be used to improve ECG diagnostic techniques.

4.5 Acknowledgment

This work was made possible in part by software from the NIH/NIGMS Center for Integrative Biomedical Computing, 2P41 RR0112553-12. The authors would like to thank the Cardiovascular Research and Training Institute and the Small Animal Imaging Facility, supported in part by NIH grant S10-RR023017. Support for the acquisition of the data used within the simulation studies came from the Nora Eccles Treadwell Foundation.

CHAPTER 5

BOUNDARY CONFORMING MESHING IN ELECTROPHYSIOLOGY

5.1 Introduction

Recent improvements in computing continue to fuel a rapid increase in the use of patient specific models to help predict and study disease [11, 15]; however, technical challenges impede achieving the full potential of this technology. One example of rapid progress is in the field of electrocardiology, in which bioelectrical activity can be modeled, both within the active myocardium and through the surrounding passive volume conductor, using efficient implementations of the mesh-based computational strategies of finite and boundary elements. While the use of such models in clinical cardiology settings is growing, for example, in such domains as ventricular arrhythmias [155], implantable cardioverter defibrillator (ICD) placement [156, 157], and detecting atrial activation sequences [158, 159], these approaches have yet to achieve widespread clinical application.

Each stage of the typical simulation pipeline [11] presents decisions that trade off fidelity to reality against computational cost. Even with the dramatic increases in computational resources available to biomedical scientists, these decisions can be difficult and critical. The decisions start with the spatial and temporal sampling of image acquisition, and even the selection of imaging modality. For example, MRI has moderate spatial resolution, poor time resolution but is sensitive to soft tissue types. Spatial resolution can be improved over the standard clinical settings, but only with an increase in imaging time, often complicated by the need for breath holding in compromised patients or ECG gating during unstable heart rhythms. Computed tomography, in comparison, has severalfold better resolution in space and time but requires contrast agents to identify soft tissues and also involves potentially harmful ionizing radiation. The choice of modality is typically a compromise between these features, driven by the needs of the simulation, which in computational cardiology is made even more complex because the heart has high spatial complexity with internal boundaries between different chambers and tissue types, as well as relatively rapid contractile motion. The final challenge with image preparation comes with segmentation of the regions of interest within the body and organs to be simulated—to decide how many and which regions of varying properties are required.

The focus of this study was the next stage in the simulation process, the conversion of segmented images to meshes, which tessellate the domain of interest, as well as the associated numerical methods used to solve the problem of interest. As with the other decisions required in carrying out biomedically or clinically useful simulations, the selection of mesh type, resolution, and features can be complex and involve compromises. Ultimately, the selections depend on the specific setting and problem, as well as the expected constraints of available computational resources and acceptable compute time. Specific to computational cardiology is the need to capture the complex shape of the heart including many small features such as papillary muscle and endocardial surface irregularities or myocardial walls that can be as thin as 2 mm. Simulations of cardiac bioelectricity can also involve the entire torso, *i.e.,* features like the thorax and its internal structures, *e.g.,* bone, lungs, muscle, fat, and other soft tissues.

Representing these tissues in a computer model is challenging not only due to intricate or small external features, but also due to the complex internal interfaces formed as two or more tissues (generically, *materials*) share points, edges and surfaces. When only two materials are involved in the segmentation, the interface between them is by definition a manifold surface, *i.e.,* at least locally it resembles the surface of a sphere in that it separates two regions. However, when three materials interface, the interfaces of each pair of materials come together in a "T"-shaped, nonmanifold configuration. And if more than three materials come together in the same region, the complexity of their interfaces grows, creating more sophisticated nonmanifold interfaces. These types of complex interfaces create special challenges for meshing algorithms, which typically assume only two materials. To bypass this difficulty, some meshing techniques simply ignore or approximate such complex internal material boundaries in a way that preserves simple topology. Such methods are "nonconforming" because the vertices of the mesh are not forced to align with the material interfaces. Figure 5.1 illustrates the difference between conforming and nonconforming internal boundaries in a model. One consequence of nonconforming approaches to meshing is that each element is assigned tissue properties based only on the location of its centroid (or some other measure of its center of mass) relative to but not aligned with the original material boundary, which creates a more or less jagged representation of the actual interface.

The influence of mesh quality—spatial resolution and fidelity to the original surface(s)—on simulation accuracy is a critical facet of evaluating the utility of a simulation. It is of

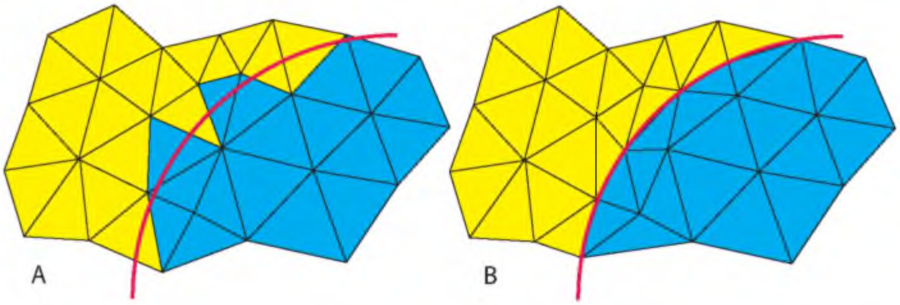

Figure 5.1: A comparison of conforming and nonconforming meshing at a boundary between two material types. The solid red line represents the original boundary between the two materials. Figure A shows a meshing algorithm that does not attempt to preserve the interface during the tessellation of the volume, but reconstructs the boundary post-tessellation. Figure B shows a conforming mesh that attempts to preserve the boundary by placing nodes directly on the interface.

special importance when the shape and/or composition of the underlying tissues are critical contributors to the physiology under study, which is almost always the case in studies of electrophysiology in the heart. It is unrealistic to generalize about the sensitivity of simulations to their underlying mesh because each simulation is so vastly different. Here we focus on a specific aspect of mesh quality, the extent to which the mesh respects external and internal tissue boundaries, in the specific setting of simulating tissue or whole-heart cardiac electrophysiology. We have shown in previous research that simulating cardiac electrical potentials through a finite element volume with nonconforming boundaries produces local concentrations of current resulting in electrical potential elevations and depressions that were not exhibited when simulating with conforming meshes [160]. The magnitude and the spatial extent of these concentrations were dependent on the resolution of the mesh and the rate of change in electrical potential over the boundary. Even with highly refined mesh resolution, the magnitude of the local errors reached 9–12%. These results raised broader questions as to the appropriate representation of boundaries for simulations of cardiac bioelectricity, for example whether the local artifactual increases in current density near the jagged surfaces of nonconforming meshes (Figure 5.2) are large enough to change the meaning or interpretation of the simulated results.

The guiding hypothesis for this study was that conforming boundaries produce significantly more accurate results at much lower resolutions compared to nonconforming boundaries, and that the errors resulting from nonconforming meshes are large enough to alter the interpretation of simulation results. In addition to verifying this hypothesis, we were able to

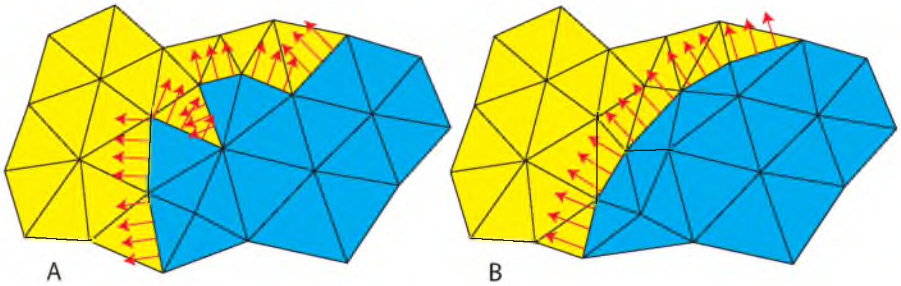

Figure 5.2: Discrete currents at a material interface. Figure A: shows the same mesh as in Figure 5.1 and the local concentration of current that will form at the jagged interface between two materials with varied conductivity; these currents can result in artificial extrema and hence errors. Figure B: such unintended current concentrations would not occur with the smooth interface created by the conforming mesh.

show that simply refining the mesh resolution has only limited effect on removing artifacts from nonconforming boundaries, and therefore, that conforming meshes often produce more accurate results at much lower mesh resolutions (and reduced computational cost). This hypothesis was tested on three separate common numerical methods in cardiac bioelectric simulations: volume conductor, bidomain, and reaction-diffusion bidomain. Errors from nonconforming meshes were particularly evident in simulations of pathophysiology that were highly dependent on internal tissue boundaries, such as modeling the effects of discrete regions of damaged heart tissue. The results indicate that while creating conforming meshes is more challenging and time consuming, it is often necessary to capture local electrical behavior in the heart such as regional myocardial ischemia or focal ectopic activity. At the same time, the complexity and computational cost of conforming meshing may not be justified when simulating features that are more global in nature, such as the activation time of a multimaterial model of the whole heart.

The goal of all simulations of cardiac electrophysiology at the tissue and whole-heart scale is to incorporate relevant behavior from the smaller scales, *i.e.,* cellular, membrane, and molecular, into a tractable formulation that can capture the meaningful aspects of electrical activity observable at this scale. It is impossible to predict whole-heart behavior as a direct ensemble of the approximately 10 billion cardiac myocytes in the heart yet it is essential for a whole heart model to capture variations in action that are based in the cell or membrane. Thus, successful cardiac tissue simulation approaches approximate, often through homogenization, behavior at one scale while still driving it from concepts and influence from a smaller scale. The three simulation approaches described below differ in how they carry out this approximation and which assumptions they include. Because of this diversity of approach, it is reasonable to assume that the impact of mesh structure may affect each method differently. In order to explore the role of mesh structure on at least a small sampling of applications, we also selected three timely simulation problems from cardiac electrophysiology.

5.1.1 Modeling Defibrillation - Volume Conductor

The goal of this first example of simulating cardiac bioelectricity is to estimate the electric potential throughout the human torso following an electrical shock applied to reset uncoordinated activation in the heart. Physically, this situation corresponds to a volume conductor problem within a single, passive domain which is assumed to have inhomogeneous (or piecewise homogeneous) and potentially anisotropic conductivity. The associated electrical source consists of a discrete set of electrodes, which are embedded at two or more locations within the volume conductor.

The goal of this volume conductor example is to simulate the action of implantable cardiac defibrillators (ICDs), which are a commonly used device for patients who are at risk of severe cardiac arrhythmias. When the device detects electrical propagation that it identifies as life threatening, it produces a shock that is intended to shock the heart and return it to normal sinus rhythm. In most patients, ICD implantation is a routine operation using standard locations for the ICD and its electrodes. However, in a small but important population, the standard procedure is not possible. Most notably in small children or children with congenital heart defects the absence of a standard procedure forces physicians to adapt the operation for each patient. Recent reports from our group have shown that patient specific models of the thorax can assist in deciding the best locations for the device [161, 157]. These models represent tissues with passive electrical conduction and are well suited to the monodomain formulation.

5.1.2 Modeling Acute Myocardial Ischemia - Single Time Point Bidomain

In contrast to the essentially passive volume conductor in the previous example, the bidomain represents an electrically active region comprised of two continuous volume conductors that provide independent pathways for current to flow. The two domains correspond to the intracellular and extracellular spaces, which occupy the same physical space and are coupled by the electrically active membrane, as described by differential equations that capture the associated physics. In the heart, current flows through both the intracellular and extracellular spaces, driven by ionic currents generated by the cellular membrane and described by differential equations that model their behavior. In the simplest form of the bidomain, a subset of potentials is known, *e.g.,* transmembrane potentials, and the goal becomes to compute the remaining unknowns, *e.g.,* extracellular potentials.

The cardiac bidomain typically also describes temporal behavior corresponding to the membrane action potential resulting in the propagation of electrical activation. Our group has previously developed a simplified, static version of the bidomain, in which we assume a known distribution of transmembrane potential corresponding to what is known as regional myocardial ischemia [25] as described in Chapter 2. Ischemia is a tissue level phenomenon that results in whole-heart currents that are detected on the body surface as abnormal elevations and depressions in the ECG. Ischemic conditions arise relatively slowly in the heart and and the resulting currents persist through approximately 100 mS of each heart beat. Thus, they represent relatively static electrophysiological conditions suitable for this simplified simulation approach. Motivation for simulation comes from the fact that while ST segment shifts are very commonly used clinical indicators, their underlying mechanisms are poorly understood, especially when the region of tissue involved does not span the full thickness of the heart [162]. By carrying out the simulation under static assumptions, it is possible to select a single time instant or short interval during the ST segment and supply approximate transmembrane potentials and then evaluate the effects of variations in location and extent of the ischemic tissue on the electric potentials throughout the heart [26, 163].

5.1.3 Modeling Cardiac Activation and Repolarization - Reaction Diffusion Bidomain

In the complete time-dependent form of the bidomain, a cardiac myocyte is excited and current begins to flow across the cell membrane, diffusing into the extracellular and intracellular spaces, subsequently exciting neighboring cells. This chain reaction produces a wave that propagates through the myocardium. One way to describe this behavior mathematically is as a reaction diffusion bidomain simulation that consists of two steps. First there is a reaction, in this case, current crossing the cell membrane modeled as a set of differential equations. In the subsequent diffusion step, the ions move more or less freely through each continuous domain, which is approximated by a partial differential equation. The whole system is solved iteratively over time to simulate the excitation wave.

A full bidomain approach is required in simulations of the heart that incorporates both spatial and temporal features, *i.e.,* when the electrical state of the heart depends on time evolution of propagating waves. This generality of approach also makes the time evolving bidomain suitable for capturing a full range of cardiac behavior, with special focus on abnormal heart rhythms or “cardiac arrhythmias” [10, 24]. The bidomain approach includes details of myocardial structure, electrical conductivity in both intracellular and extracellular domain, and the behavior of the cellular membrane but is also capable of high efficiency so that it has become the dominant approach for carrying out simulations across enormous ranges of scale and for subject specific settings [164, 10].

5.1.4 Boundary Conforming Meshing

One feature of all these applications of simulation that is common to a wide range of disciplines is the need to create subject specific geometric models in the form of nodes and polygons that support the application of numerical methods. Mesh generation is a challenging problem which we define here as creating in some automated way a tiling/tessellation (a *mesh*) of some simulation domain using simple geometric shapes such as tetrahedra, pyramids, or hexahedra. Popular approaches for mesh generation consist of tetrahedral meshes constructed with stenciling [117], optimization of vertex locations [116, 115], and iterative refinement [113, 114].

To represent geometric structures faithfully, one goal of mesh generation is to create *conforming meshes*, in which the mesh seeks to represent surfaces, both within the volume and on the outer surfaces, with great fidelity. Achieving this goal requires careful choice of node density and location and element orientation [165, 166, 167]. The resulting threefold tradeoff in mesh construction is between the fidelity of these surfaces to the original internal boundaries, preservation of the quality of the resulting mesh elements, and the often considerable computational cost of the algorithms that identify and preserve their shape. While somewhat ambiguously defined, the quality of mesh elements is determined by factors like the aspect ratios, which should generally meet some prescribed constraints. For example, an isotropic prescription of quality would prefer “round” elements (*e.g.,* equilateral triangles, cube-like hexes) over long, thin elements with acute angles between edges. Contemporary approaches to mesh generation address this concern by integrating element and simulation quality, measured through an adjoint estimation of error that guides mesh construction and also refinement with respect to error metrics [168].

In this study we leveraged a *variational* meshing algorithm, BioMesh3D [138], to create both conforming and nonconforming meshes from the same image data. BioMesh3D creates meshes by first distributing particles on the surfaces to which the mesh must conform [115], using variation to drive an energy minimization process to find ideal placements for the particles. These particles are then treated as mesh vertices, and the remaining mesh elements are constructed using a three-dimensional Delaunay triangulation (tetrahedralization) implemented in the open source software, TetGen [139]. For this study, we created meshes that both conformed to and ignored various shapes of internal boundaries in a series of simulations from cardiac electrophysiology and examined carefully the resulting errors. Our goal was to establish the extent and the nature of the improvements that result from creating meshes that conform faithfully to internal tissue boundaries in this domain of bioelectric field simulation.

5.2 Methods

The three cardiac bioelectric simulations described above were used to test the errors associated with nonconforming versus conforming meshes created with a range of resolutions. The gold standard for the simulations was a conforming mesh created at the highest resolution that was tractable; error metrics quantified both global and local variation. A further test was based on differences in the quantitative results as well as the interpretation of those results in the context of the simulation goals. For example, in the case of defibrillation, we evaluated the change in required shock strength, and for the simulation of ischemia, the change in the epicardial elevations and depressions. For the reaction diffusion models we compared the patterns of the spread of activation for different meshing strategies.

5.2.1 Mesh Generation

As described in Section 1, it is necessary to evaluate sources of error at each stage in the simulation pipeline and for this study, we focused on the transition from segmented images to computational mesh. Segmented images are discrete voxel representations of continuous and usually smooth geometry of organs and parts of the body captured at the resolution of the imaging modality. The simplest of all reconstructions would be to assume each voxel represented a hexahedral, resulting in a mesh that matched the original image but with surfaces that had a ragged or stair-stepped profile. However, in most biological tissues the true boundaries are not stair-stepped but are smooth. Consequently, creating smooth surfaces is a goal of most image based meshing algorithms such as marching cubes, Laplacian smoothing, curvature limiting smoothing, or spline based surface fitting. Our goal was not to evaluate the quality of fit between the smoothed surface and the original anatomy, but to determine the extent of the error introduced into the results of simulations by representing an anatomically smooth surface as a nonboundary fitting, or nonconforming volume mesh. Creating a ground truth for realistic simulations is challenging because of a lack of both analytical representations of realistic anatomy and analytical solutions to simulations of interest. Instead, we first built a very high resolution, smooth representation of each geometry and used the resulting simulation results as the standard for comparison.

Both the conforming and nonconforming meshes were then based upon the smoothed reference geometry. There are many different meshing techniques that are considered nonconforming; however, in this study we focused on unstructured tetrahedral meshes that conformed to the exterior surface but not the internal boundaries. The nonconforming meshes were created by filling the volume defined by the exterior conforming surface with Delaunay tetrahedra at prescribed resolutions, but ignoring the internal interfaces. After the mesh was generated, the elements were grouped by material type based on the location of each element relative to the reference surfaces. In contrast, the conforming meshes were generated in a way that preserved the internal boundaries of the reference geometry.

To formally describe the conforming meshes, we define a volumetric mesh $M = (V, E, F, C)$ to be a collection of vertices, V, edges, E, faces, F, and volumetric cells, C and let Σ be a surface embedded in three dimensions. In this context, M is called *conforming* if it explicitly represents Σ with the following conditions:

1. A subset of mesh vertices, V_Σ lie on Σ.
2. A set of mesh faces (in our context, triangular faces of tetrahedra) approximate Σ. In particular, these triangles will have their vertices as part of V_Σ and the plane of each of these triangles will be an approximation of the tangent space of Σ at each vertex of the triangle.

While there are stricter definitions of conformality, for example those that require a homeomorphism between Σ and the triangular faces which approximate it [166], applying such requirements would be unrealistic since the true Σ is not known, but rather only approximated from the image data. Thus, we think of conforming meshing as both requiring a geometric approximation in terms of distances to the surface boundaries as well as requiring the tangent space of the surfaces to be well approximated by the linear elements. Within this framework of conforming meshing, the specific geometric model and the numerical approach was different for each of the three examples, as described below.

5.2.2 Simulation of Cardiac Defibrillation

5.2.3 Geometric Model

In this example case, the biomedical goal is to predict the success of defibrillation from implantable cardiac defibrillators (ICD) using patient specific modeling and operator guided placement of the device [161, 156, 157]. To create the necessary patient specific geometric models, we used MRI scans of an entire torso from which we segmented, using both manual and automated approaches in Seg3D [19], the lungs, muscle, fat, bone, heart, blood, and connective tissues [169]. Realistically shaped meshes of the ICD generator and ICD shock electrode were manually oriented in the torso geometry under the left clavicle and in the right ventricle, respectively, using the SCIRun software framework [136]. SCIRun also provided the tools to create nonconforming meshes as structured tetrahedral grids with mesh refinement around the ICD generator and ICD shock electrode [156] while we used Biomesh3D [138] to create the conforming meshes, which also included refinement around the ICD and electrodes.

5.2.4 Simulation

For the simulation of defibrillation, we used the monodomain approach, which seeks to solve equations of electric potentials within a volume conductor under assumptions of passive electrical behavior. Such assumptions hold strictly in the torso volume outside the heart and while they are a simplification within the heart they are valid under the conditions of the very rapid external shock applied to the heart. Poisson's equation describes potentials resulting from a current density source and can be written as

$$\nabla \cdot \sigma \nabla \Phi = I_v, \tag{5.1}$$

where σ is the conductivity, I_v is the source current density, and Φ is the electrical potential. An additional Neumann boundary condition reflecting the fact that currents do not leave the body can be written as

$$\nabla \Phi \cdot \vec{N} = 0, \tag{5.2}$$

where $\vec{N}$ is the surface normal.

The ICD generator and electrodes were modeled as source and sink voltages within the torso. The potential difference needed to achieve 95% of the myocardium over 5 V/cm gradient (critical mass hypothesis) [170] was used as the metric to compare the overall accuracy of simulations from different mesh types.

5.2.5 Static Simulation of Acute Myocardial Ischemia

5.2.6 Geometric Model

The geometric model used for the simulation of electrocardiographic fields that arise during acute myocardial ischemia consisted of the heart and blood that were derived from an MRI of the same canine heart as used in the associated experimental study. The goal of these studies was to determine from measurement of intramyocardial potentials the distribution of ischemic regions in the heart and then simulate from them the heart surface potentials and eventually the ECG [43, 171]. In addition to representing the blood and the myocardium, these models contained one or more ischemic regions modeled as seen in Figure 5.3. The shape and location of these regions were derived from the three-dimensional distributions of extracellular potentials captured during ischemic phases of the experiment. Simulations based on cardiac tissue also require a description of local muscle fiber direction, which was acquired using diffusion tensor MRI and applied to each mesh as anisotropic conductivity tensors assigned to each element. The magnitude of these tensors was assigned based on microdomain simulations of ischemia by Stinstra *et al.*[49].

5.2.7 Simulation

To simulate the electric potential on the surface of the heart from regions of acute ischemia within the ventricles, we used a simplified, static version of the bidomain formulation described previously [26, 163, 160], which can be written as

$$\nabla \cdot (\sigma_i + \sigma_e)\nabla\Phi_e = -\nabla \cdot \sigma_i \nabla \Phi_m, \tag{5.3}$$

where Φ_e and Φ_m are the extracellular and transmembrane potentials, and σ_e and σ_i are the extracellular and intracellular conductivities, respectively. The ischemic region was modeled as having reduced action potential amplitude, expressed as a 30 mV potential difference between ischemic and healthy tissue during the plateau phase of the action potential (ST segment of the ECG). The blood was modeled by setting the intracellular conductivity to zero and the extracellular conductivity to 4 times that of the myocardium [49]. Neumann boundary conditions were applied to the outer surface of the heart, which simulated the open chest conditions of the experiments.

5.2.8 Propagation Modeling

5.2.9 Geometric Model

The simulation of propagation made use of the same geometry of the heart, blood, and ischemic regions as the ischemia model, but made use of a reaction diffusion simulation

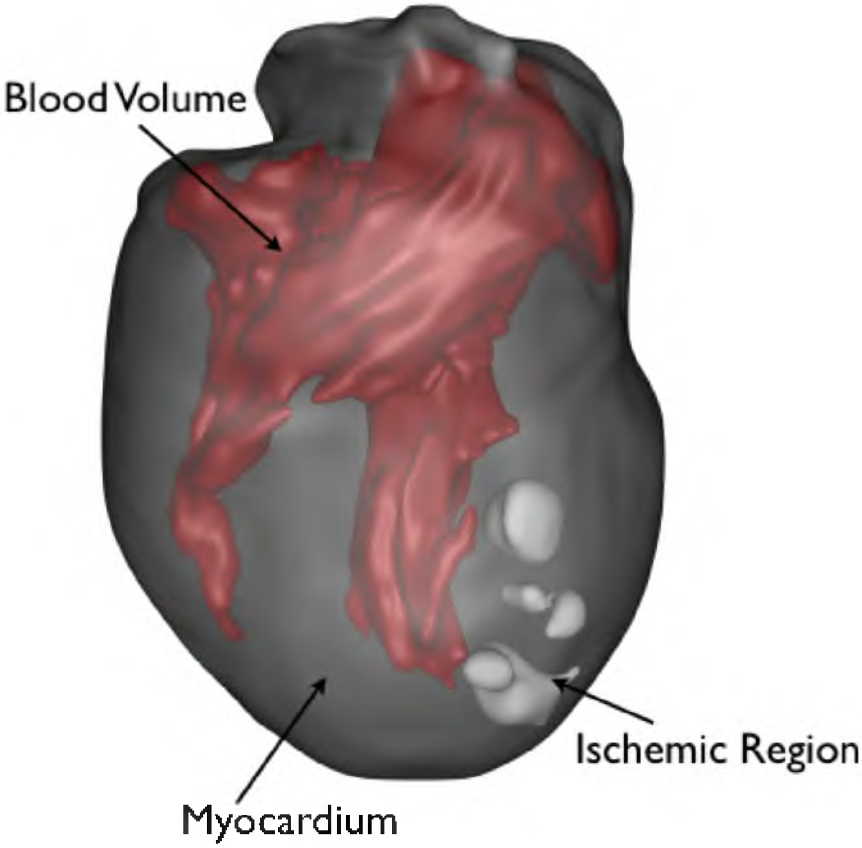

Figure 5.3: Model used to simulate myocardial ischemia. The model includes three regions: normal myocardium, blood, and ischemic myocardium and the figure shows the high quality visualization possible from meshes that conform to the material boundaries.

to predict the spread of cardiac electrical activity. Such a simulation requires a much more refined spatial resolution so that a full scale model of the heart would include tens of millions of nodes, beyond the scope of most computational resources. To reduce the size of the models to produce tractable simulations, we scaled the size of the geometry by a factor of 0.4, reducing the number of nodes by an order of magnitude.

The number of elements and nodes required to achieve a particular mesh resolution depends on the total surface area and volume of the geometry. For example, if the edge length of a hexahedral is cut in half, the result is eight new hexahedral and thus a cubic relationship. Tetrahedra are similar, but because they are not necessarily structured, the exponential relationship to the number of elements is very dependent upon the shape of the geometry being tessellated. Because hearts naturally vary in size and shape, and in our case due to a scaling factor, the total number of elements and nodes make very poor descriptors of mesh resolution. We have chosen instead to report the results in terms of average edge length which has an exponential relationship with the number of elements.

5.2.10 Simulation

To create realistic simulations of the spread of excitation in the heart, the full version of the time evolving bidomain [71] is the most commonly used approximation approach and has been implemented in widely available software (*e.g.,* CHASTE [172] and CARP [12]). This formulation also represents a reaction-diffusion system, expressed as the following system of coupled equations

$$\nabla \cdot (\sigma_i \nabla \Phi_i) = \beta I_m \nabla \cdot (\sigma_e \nabla \Phi_e) = -\beta I_m \tag{5.4}$$

where Φ_e, Φ_m, σ_e, and σ_i are defined as above and I_m is the ionic current flowing through the membrane. The transmembrane current was solved using the Faber Rudy model [173]. To predict changes in the spread of excitation in response to ischemia, we modified the ionic concentrations and the ionic currents according to Jie *et al.* [24] and as described in Table 5.1.

5.2.11 Evaluation of Error

The error was calculated by comparing each simulation to that generated using the smoothed reference conforming mesh. The global error was determined by taking the

Table 5.1: Normal and ischemic values and scale factors used in the membrane model of the bidomain simulation

	Normal Tissue	Ischemic Tissue
$[K^+]_o$ (nM)	5.4	15.0
$[Na^+]_i$ (nM)	10.0	15.0
$[ATP]_i$ (nM)	6.8	5.0
I_{Na} Scale	1.0	0.5
I_{CaL} Scale	1.0	0.5
I_{NaCA} Scale	1.0	0.2
I_{NaK} Scale	1.0	0.3
I_{over} Scale	1.0	0.65
I_{rel} Scale	1.0	0.05
I_{up} Scale	1.0	0.9
I_{Cab} Scale	1.0	1.3
I_{nsCa} Scale	1.0	1.7

root mean squared error over the entire mesh. The maximum error was also reported for each simulation, representing a more local error measurement. These errors were recorded through a range of mesh resolutions as defined by edge length. In addition to the RMS and the maximum error, at each material boundary the mean and maximum error were reported as a function of distance. In the case of the reaction diffusion simulations, the RMS error was calculated at each time step and then averaged for the whole time series.

The errors in the simulations were also evaluated as to their possible influence on the interpretation of the results. These parameters included, change in predicted shock value in the defibrillation models, change in the epicardial elevations and depressions of the ischemia models, and change in activation patterns and times for the reaction diffusion models.

5.3 Results

5.3.1 Defibrillation - Volume Conductor

The distribution of potential gradients (which correspond to electric field and hence current density) for the conforming and nonconforming models were noticeably different near the heart, as seen in Figure 5.4. The color-coded potentials from the two cross sections show gradients that were much sharper in the nonconforming mesh. It also contained more concentrated low voltage regions whereas the conforming mesh produced a smoother distribution of voltages. These difference were quantified in the final calculation of the total voltage required to reach the critical mass threshold. The nonconforming mesh predicted a 9% higher required voltage than the conforming mesh in order to reach this threshold.

Within the defibrillation model, the maximum error was as large as 15% near the stimulating electrode surface, while the mean error was less than 4% over the entire range as seen in Figure 5.5. As the mesh resolution increased, the maximum errors also decreased. However, the mean errors only decreased slightly (by 1%) as mesh resolution increased.

5.3.2 Ischemia ST Segment - Nontime Series Bidomain

Electrical potentials for the conforming meshes were smoothly distributed throughout the myocardium and on the epicardial surface Figure 5.6. The nonconforming meshes had regions that looked more discontinuous and resulted in small patches of elevations and depressions not seen in the results from conforming meshes. These patches created errors even on the epicardial surface Figure 5.6 that were as large as 2 mV which is 30% of the largest elevations seen on the surface. Errors of this magnitude are large enough to change whether an elevation or depression is considered ischemic, or just natural variation. The

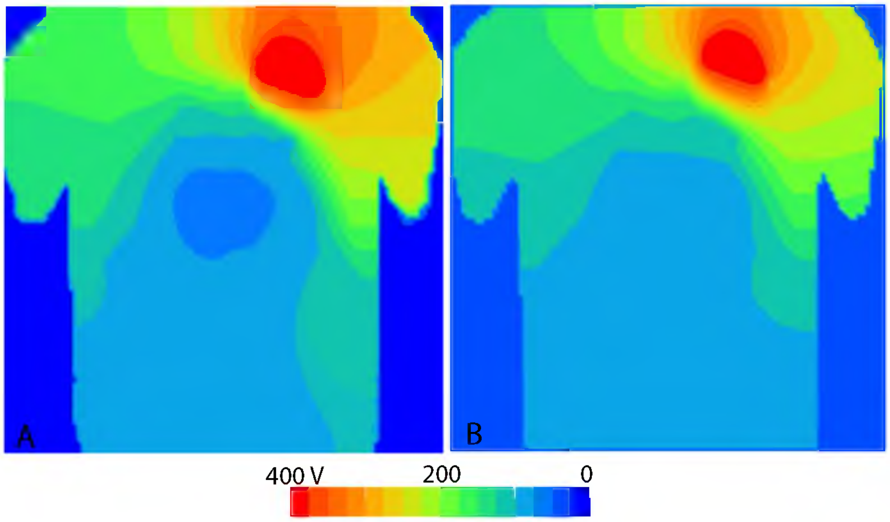

Figure 5.4: Cross-section through the torso model showing simulation of defibrillation. Panel A: shows color coded potentials from a simulation using a nonconforming mesh of an ICD shock. Panel B: shows results at the same cross section from a stimulation of the same ICD and shock settings on a conforming mesh of the same geometry.

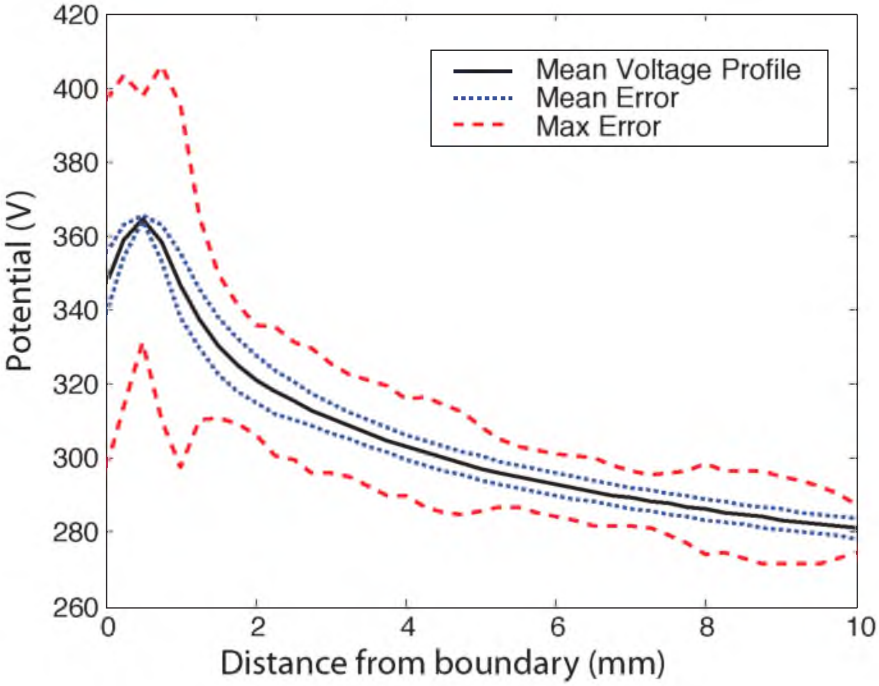

Figure 5.5: Voltage profile as a function of distance from nonconforming surfaces. The mean voltage bounded by the mean error and the maximum error measured as distance from each node in the model normal to the closest boundary boundary.

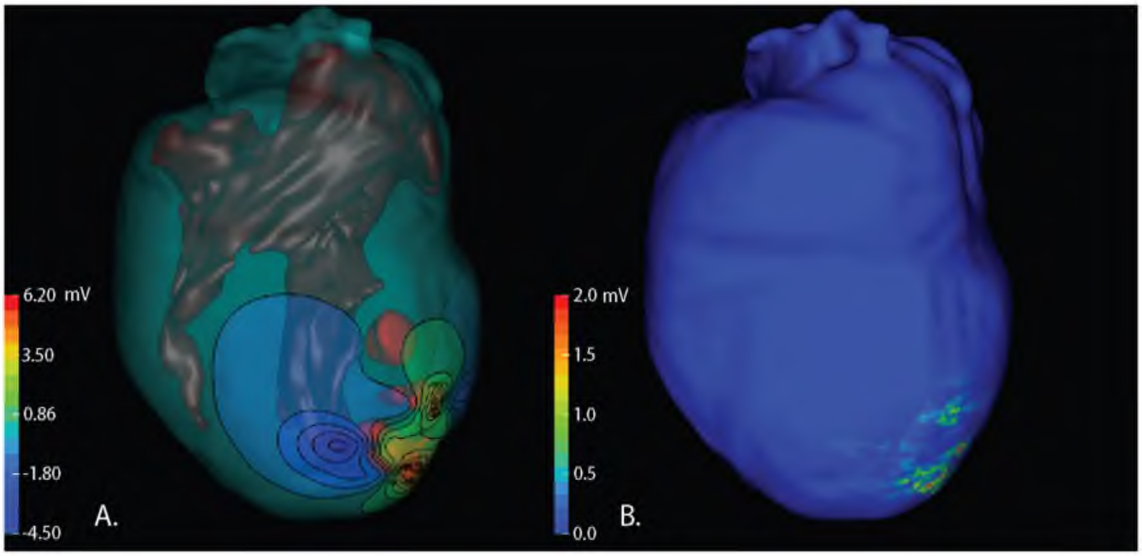

Figure 5.6: Solved bidomain simulation of epicardial potentials during acute ischemia with the location of maximal errors. A: Is a voltage map on the epicardial surface due to injury currents of an ischemic region within the myocardium simulated with a conforming mesh while B: shows the location an magnitude of errors that arise when a nonconforming mesh is used.

location of the errors is collocated with the region being analyzed. Further away from the nonconforming surfaces bounding the ischemic zone, both meshes produced smooth distributions of voltage. However, the voltage maps were altered even at a distance when there were significant current concentrations near the ischemic zone boundaries, a situation to be expected as the so called “leakage” currents from ischemia arise at these boundaries.

Figure 5.7 shows both root mean squared (RMS) errors and the maximum errors as functions of edge length. The potentials in this simulation ranged from 30 mV to -10 mV making the maximum errors of 10 mV very significant. Regions with the largest errors were located along to border between the ischemic and healthy tissue. Due to the proximity of the ischemic region to the epicardial surface (as low as 3-4 mm), many of the local errors appeared on the epicardial surface directly above the ischemic region. The errors resulted in small elevations of 4 mV and depressions of 5 mV in the coarser nonconforming meshes. These errors improved with mesh resolution, but persisted until very high resolution meshes of 0.8 mm edge length or smaller. The maximum errors were substantial for both types of meshes at very low resolution. However, the error in the conforming meshes decreased very rapidly with improved resolution while there were only slight improvements in the nonconforming meshes.

Other nonconforming boundaries were much smaller sources of error than those sur-

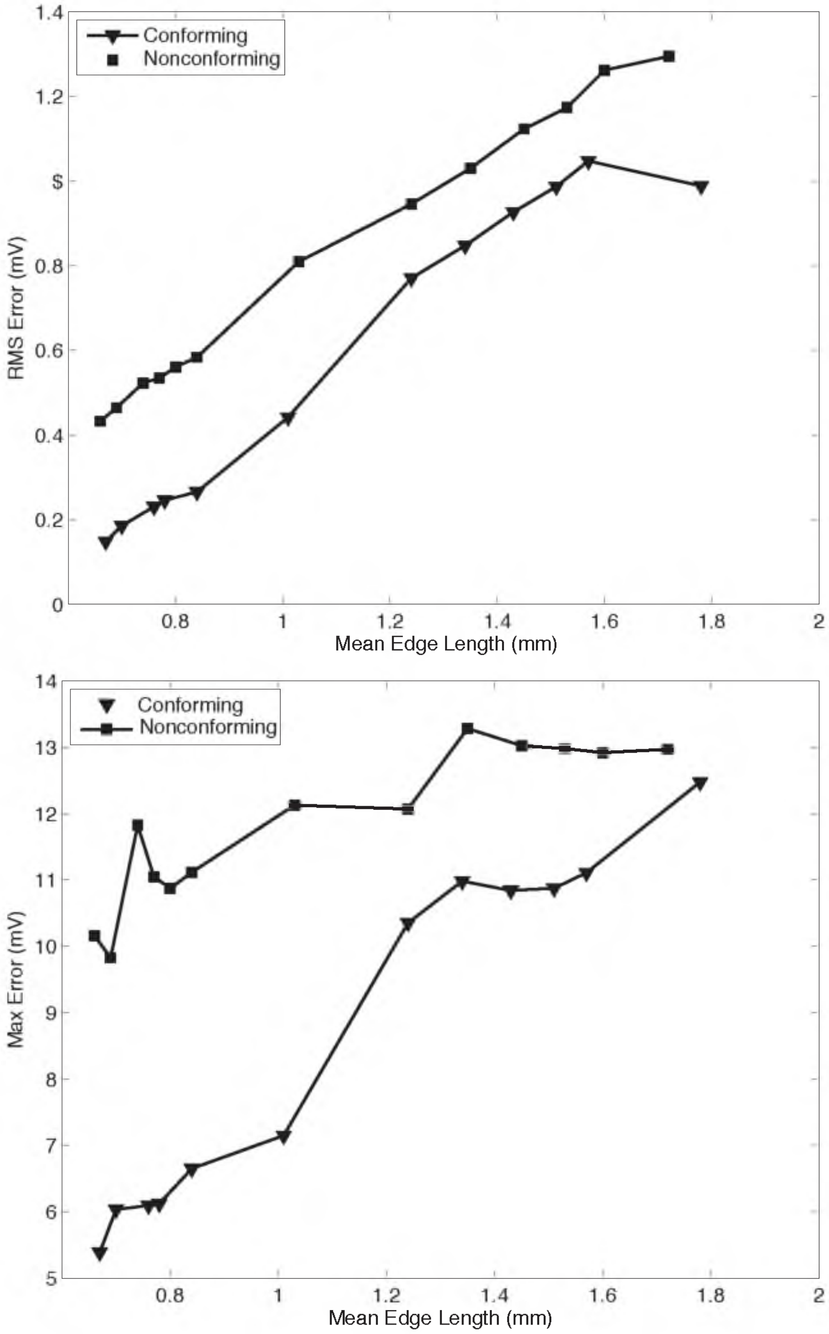

Figure 5.7: RMS and max error in conforming and nonconforming ischemia models. The graph on the left indicates the RMS error for both a set of conforming and nonconforming meshes at varied resolutions. The graph on right indicates the maximum error seen in the same set of simulations.

rounding the ischemic regions. The errors at the blood boundaries caused voltage shifts of up to 5% over the gold standard. The maximum errors at these boundaries showed slight improvements with increased mesh resolution, reducing the error to just over 3%. Current densities at blood boundaries were much smaller than those over the ischemic zones, consistent with the observation that the largest errors arise near regions of concentrated sources.

Globally, the conforming meshes produced an RMS error of at least 0.2 mV better than nonconforming meshes over the entire range of mesh resolutions which did not improve as the meshes became more refined. A second way to consider these results is that a nonconforming mesh with an average edge length of 0.65 mm would give the same accuracy as a conforming mesh with a larger edge length of 1 mm. For such models, this improvement would represent the difference between 1.7 million and 0.49 million nodes.

5.3.3 Reaction Diffusion Bidomain

Figure 5.8 shows the RMS error of potentials during activation as a function of model resolution for the spread of activation of a heart beat under conditions of localized ischemia and suggests that there is no clear difference in performance between conforming and nonconforming meshes for this problem. The maximal errors indicated more substantial sensitivity to mesh choice than RMS as they showed values as large as 18 mV, which all occurred along the activation front, whereas errors along the material boundaries were an order of magnitude smaller, much like the errors found in the static bidomain simulations found in Figure 5.7, suggesting once again that regions of high source strength respond most strongly to choice of mesh type.

Figure 5.9 shows the first 200 ms of the RMS curves of the simulated electrograms for two different mesh resolutions. The RMS curves produced by the lower resolution meshes had decreased slopes and increased widths of the activation wave form, which is indicative of conduction slowing. This trend held through all mesh resolutions, confirming that the propagation velocity does change across mesh resolutions, but also that there is very little difference between the conforming and nonconforming meshes when they had similar resolutions. The activation times computed for both mesh types were very similar, within 3% demonstrating that there was no clear advantage to one or the other. These findings suggest that the selection of mesh type plays no substantial role in simulation accuracy.

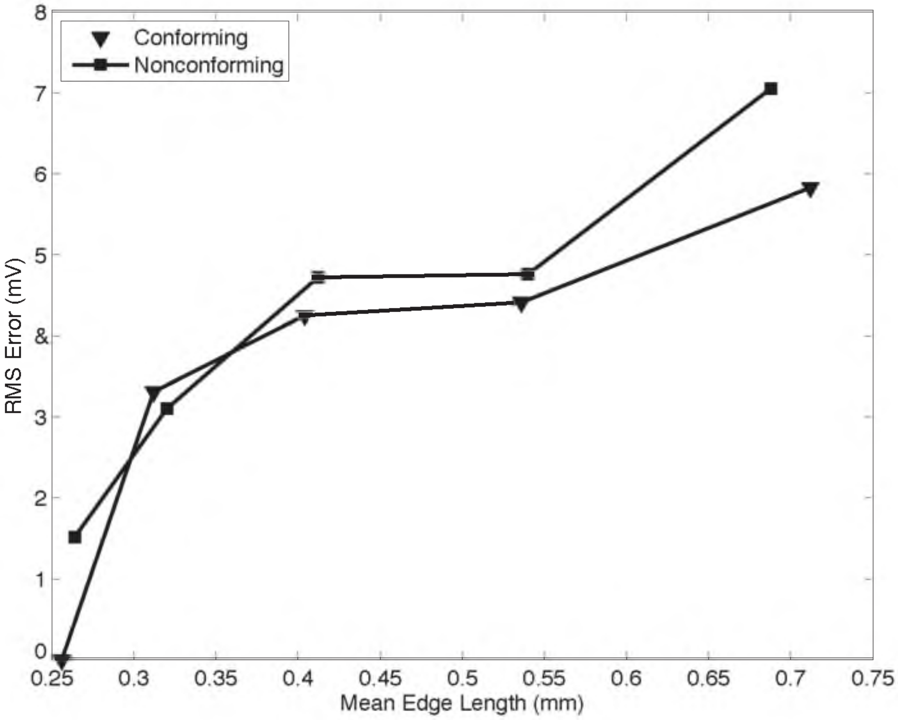

Figure 5.8: RMS error from reaction diffusion bidomain simulation of the spread of activation. The RMS error over the entire activation of the ventricles comparing conforming with nonconforming meshes as a function of mesh resolution (edge length).

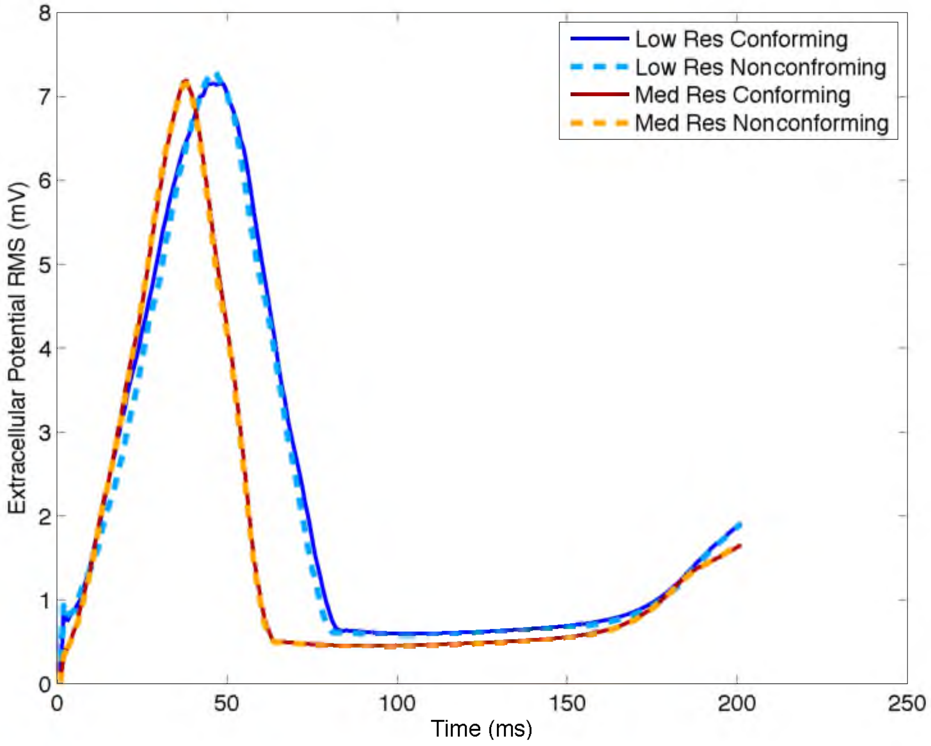

Figure 5.9: Extracellular RMS electrograms from a reaction diffusion bidomain simulation for each time step. This figure shows for two different mesh resolutions, the RMS error in voltage as a function of time for beats computed using both conforming and nonconforming meshes.

5.4 Discussion

The goal of these studies was to evaluate the benefits to simulation accuracy associated with finite elements meshes designed to reproduce internal boundaries with high fidelity. Such conforming meshes involve more elaborate algorithms and lengthier computation times than nonconforming or nonboundary fitting meshes, and their value for visualizing the structure of the underlying anatomy and the simulation results is clear because of the smooth surfaces their tetrahedral elements can produce. What is not, to our knowledge, established is the extent and nature of any benefits to simulation accuracy of meshes that conform to both external and internal surfaces. A completely general answer to this question is unlikely and so we have selected to evaluate three different and common simulation strategies in an application domain of interest in medicine. In contrast to previous evaluations based on more or less arbitrary indices of mesh quality, we focused instead on the results of the bioelectric field simulations produced by these meshes. Our results suggest that even within this single domain of cardiac electrophysiology, the choice of meshing strategy yields diverse impact depending on the goals of the simulation.

The hypothesis that nonconforming meshes could lead to artifacts that significantly affect the results of simulations was supported for both the defibrillation and the static bidomain studies but less convincing for the spread of activation in the reaction-diffusion simulation using the full bidomain. In the first two cases, overall errors were higher when using nonconforming meshes. Moreover, the errors were largest in regions with large local sources, which were the tissues that were of direct interest to users of the simulations. In the case of simulating defibrillation, the spatial gradient of electric potential is the parameter thought to predict successful outcome; nonconforming meshes produced errors specifically in the gradients within the heart that would lead to an almost 10% increase in the predicted voltage required for successful defibrillation. Similarly, for the static simulation of ischemia, the errors related to meshing strategy were largest in regions of the heart that also have the largest impact on the ST-segment shifts in the body-surface ECG that are most relevant for diagnosis.

In contrast to the other cases we examined, the reaction diffusion bidomain simulation did not show a clear preference for either mesh type, at least in part due to the strong dependency of the simulations on parameters common to both conforming and nonconforming meshes, primarily the spatial resolution in the region of the activation wave front. The transition from resting to fully stimulated cells at the wave front extends over only approximately 1 mm so that simulations of propagation require substantially sub-millimeter mesh resolution. At this fine scale, the differences between conforming meshes driven by fixed anatomical surfaces and nonconforming meshes based on imaging orientation disappear and so do not play a role in simulation error. A further critical structural factor of cardiac tissue is the anisotropic nature of current flow along the long axis of heart cells and the fibers they form. While it is possible to imagine a conforming meshing strategy based on fiber orientation, our conforming meshes sought instead to respect larger scale anatomical boundaries and so would be unlikely to perform any better than a nonconforming mesh with regard to anisotropy.

While these results lack a clear conclusion regarding the relationship between the specific application and the role of meshing parameters, there are some generalities that emerge from our findings. Errors from nonconforming meshes were large in cases in which the shapes of bioelectric sources were poorly captured compared to what was possible with a conforming mesh. Examples of this scenario included the shape of the implantable cardiac defibrillator (ICD) electrode in the defibrillation model and the ischemic region in the bidomain simulation of reduced myocardial perfusion. The second case of marked differences between conforming and nonconforming meshes arose when nonconforming boundaries were in close proximity to the areas of the models most relevant for subsequent analysis and interpretation of the results. For example, in the simulation of the bioelectric effects of myocardial ischemia, the outer (epicardial) surface was at once a structure of great anatomical relevance (and hence a driver of conforming meshing) and at the same time a place where measurements and hence analysis of electric potentials occurs in experiments and occasionally even clinical practice [174]. A lack of fidelity to this surface, as in nonconforming meshes, could be expected to lead to highly relevant localized errors, which our results were able to substantiate. In contrast, in the case of simulating the spread of activation in a bidomain model of the ventricles, there was little relationship between anatomical structure and the wave front and hence little benefit to a conforming meshing approach based on gross anatomical elements.

Algorithmic and computational cost are key drivers in any discussion of meshing (or modeling) strategies and they must be part of the interpretation of our results. We found no case of a conforming mesh of similar resolution producing *worse* results than a nonconforming mesh and thus it would be tempting to propose conforming meshing as a general strategy. However, in many cases, nonconforming meshes can take seconds to generate compared to hours for comparable conforming meshes of the same size. Not conforming to the boundaries allows for computationally efficient meshing strategies such as regular grids to be implemented. Conversely, in two of the simulations presented here, a conforming mesh could produce the same quality results as a larger, more finely resolved nonconforming mesh. In the case of the ischemia model, an edge length of 0.65 mm in the nonconforming mesh was equivalent to a conforming mesh with an edge length of 1 mm which would reduce the number of nodes in the model from 1.7 million to 0.49 million. Computational speedup depends on specifications of the computer used. However, we observed improvements that were at least proportional to the reduction in size of the model and often much greater, particularly for the larger meshes. The smaller meshes also decreased the time and memory needed to process and visualize the computed solutions.

The models used in this study were all derived from MRI images but the conclusions are largely agnostic to the imaging modality. The typically higher resolution of computed tomography (CT) over MRI will, of course, result in more finely resolved surface boundaries, assuming they can be visualized either through the radio opacity of materials or contrast agents. However, the segmentation step that is an essential step in image based modeling provides a means to normalize for image resolution through techniques such as smoothing or interpolation. Thus, within the specific questions of the impact of conforming and noncomforming mesh structure, it is fair to assume our findings will apply to models derived from any imaging modality capable of resolving the boundaries of interest.

An important finding of this study was that nonconforming meshes performed just as well as the conforming meshes in the reaction-diffusion bidomain simulations. Reaction-diffusion simulations, and the bidomain approach specifically, already represent a simplification, typically a mathematical homogenization, that seek to achieve the efficiency necessary to carry out simulations of large structures, for example, the whole heart rather than just a small, presumably representative block of tissue. They are intrinsically a compromise driven by computational resources so that any improvement in memory usage or calculations is critically important. nonconforming meshes are always faster to create and to refine, and often show advantages in numerical approximations. Of specific current interest are their potential advantages in the application of parallel algorithms, either CPU or GPU (graphical processing unit) based [175]. It is somewhat reassuring that nonconforming meshes performed very well in our comparisons with conforming meshes of similar size in this setting.

One observation that can tie our findings to the more traditional evaluation based on mesh quality metrics is that element shape tends to improve as the mesh resolution becomes finer because the elements better approximate regions of high curvature. To reduce the impact of this limitation, element quality of conforming meshes, as measured by the scaled Jacobian, was monitored during the mesh creation so that all poorly shaped elements could be improved. In an effort to reduce the differences in element quality between conforming and nonconforming meshes we used the same Delaunay based meshing algorithm to create both and produced similar mesh element qualities at each resolution.

In conclusion, these experiments suggest a complex and application dependent role of mesh structure on simulation accuracy. This study has demonstrated settings in which conforming meshes outperformed nonconforming meshes of similar size but at least one major application domain in which there was no difference in simulation accuracy. Simulation scientists are faced with many decisions in creating functional pipelines and our findings suggest that careful selection of mesh generation approaches, perhaps preceded by numerical experiments, may be necessary in order to optimize these decisions for the available computational resources and desired simulation scope and accuracy. It appears unlikely that selecting the closest software to hand, or even the algorithms that have proven utility in one setting, will yield the best compromise in a new application domain.

5.5 Acknowledgment

This work was made possible in part by software from the NIH/NIGMS Center for Integrative Biomedical Computing, 2P41 RR0112553-12.

CHAPTER 6

CARDIAC POSITION SENSITIVITY

The cardiac position sensitivity study builds upon the previous two chapters in that it takes the epicardial potentials during an ischemic episode and projects them onto the torso surface. The purpose of this study was two fold. First was to quantify sensitivity of the motion of the heart due to postural changes on the ECG detection of myocardial ischemia. The second purpose was to develop a framework for using a relatively novel stochastic method, the general Polynomial Chaos-Stochastic Collocation (gPC-SC), in bioelectric simulations. The following research is published in the Annals of Biomedical Engineering and thus appears here in the format in which it was published with their permission.

Annals of Biomedical Engineering, Vol. 39, No. 12, December 2011 (© 2011) pp. 2900 2910
DOI: 10.1007/s10439-011-0391-5

Cardiac Position Sensitivity Study in the Electrocardiographic Forward Problem Using Stochastic Collocation and Boundary Element Methods

Darrell J. Swenson,[1,2] Sarah E. Geneser,[2] Jeroen G. Stinstra,[2] Robert M. Kirby,[2,4] and Rob S. MacLeod[1,2,3]

[1]Department of Bioengineering, University of Utah, Salt Lake City, UT, USA; [2]Scientific Computing and Imaging Institute, Salt Lake City, UT, USA; [3]Nora Eccles Harrison Cardiovascular Research and Training Institute, Salt Lake City, UT, USA; and [4]School of Computing, University of Utah, Salt Lake City, UT, USA

(*Received 23 May 2011; accepted 27 August 2011; published online 10 September 2011*)

Associate Editor Joan Greve oversaw the review of this article.

Abstract—The electrocardiogram (ECG) is ubiquitously employed as a diagnostic and monitoring tool for patients experiencing cardiac distress and/or disease. It is widely known that changes in heart position resulting from, for example, posture of the patient (sitting, standing, lying) and respiration significantly affect the body-surface potentials; however, few studies have quantitatively and systematically evaluated the effects of heart displacement on the ECG. The goal of this study was to evaluate the impact of positional changes of the heart on the ECG in the specific clinical setting of myocardial ischemia. To carry out the necessary comprehensive sensitivity analysis, we applied a relatively novel and highly efficient statistical approach, the *generalized polynomial chaos-stochastic collocation method,* to a boundary element formulation of the electrocardiographic forward problem, and we drove these simulations with measured epicardial potentials from whole-heart experiments. Results of the analysis identified regions on the body-surface where the potentials were especially sensitive to realistic heart motion. The standard deviation (STD) of ST-segment voltage changes caused by the apex of a normal heart, swinging forward and backward or side-to-side was approximately 0.2 mV. Variations were even larger, 0.3 mV, for a heart exhibiting elevated ischemic potentials. These variations could be large enough to mask or to mimic signs of ischemia in the ECG. Our results suggest possible modifications to ECG protocols that could reduce the diagnostic error related to postural changes in patients possibly suffering from myocardial ischemia.

Keywords—Electrocardiographic forward problem, Boundary element methods, Polynomial chaos, Stochastic collocation, Sensitivity analysis, Uncertainty quantification.

INTRODUCTION

The standard electrocardiogram (ECG) records body-surface potentials at the limbs and precordial area of the chest and provides remote measurements of the electrical activity of the heart. It is a powerful diagnostic and monitoring tool for patients exhibiting cardiac pathophysiologies such as rhythm disturbances, acute myocardial ischemia, and infarction. Despite its utility, a fundamental weakness of the ECG is the fact that it is a remote measurement, capturing cardiac electrical activity at the body surface. As a result, a number of factors that are not related to intrinsic cardiac activity can affect the signals recorded at the body-surface lead positions and thus induce errors in clinical evaluation.[1,2,12] The goal of our research was to capture and quantify those factors and their influence on the clinical use of the ECG.

In a healthy heart, the ST segment represents the time between complete ventricular depolarization and the beginning of repolarization. During this time interval, the myocardium is relatively isopotential, with potential differences that are small compared to those that arise during activation and repolarization. In a heart experiencing myocardial ischemia, there is at least one region of underperfused tissue that has decreased action potential amplitude and an increased resting membrane potential. The resulting potential difference between the healthy and ischemic tissue during the ST segment causes injury currents, which are then detected on the body surface as ST elevations or depressions.[6,11,18,21] During movement of the heart due, for example, to changes in posture, the position of these electrical sources also changes, thus changing the amplitude and orientation of the associated body-surface

---

Address correspondence to Darrell J. Swenson, Robert M. Kirby, and Rob S. MacLeod, Scientific Computing and Imaging Institute, Salt Lake City, UT, USA. Electronic mail: darrell@sci.utah.edu, geneser@cs.utah.edu, jeroen@sci.utah.edu, kirby@cs.utah.edu, MacLeod@sci.utah.edu

potentials. Our results suggest that such changes can potentially mask the injury currents. Conversely, even in a healthy heart, there are small spatial variations in action potential amplitude during the plateau phase that generate cardiac currents and body-surface potentials usually below clinically meaningful thresholds. To account for variations in ST potentials across patients and improve sensitivity of the ECG during patient monitoring, it is common clinical practice to use a baseline recording to set patient specific thresholds against which subsequent variations are compared.[2,11,26,30]

Positional changes of the heart with posture and respiration can alter ECG signal amplitude and morphology in ways that influence clinical decision making. Though the heart is anchored at its base by relatively rigid tissue, the apical end of the heart can shift position significantly within the torso due to simple movements of the patient, e.g., lying down or rolling over. In the clinical context, such positional shifts can affect the ST-segment and R-wave amplitude[22]; however, these parameters are also common indicators of myocardial ischemic injury.[6,11,18,21] Postural changes can be minimized and controlled during ECG recording for diagnostic and acute evaluation purposes, but not during continuous patient monitoring. Even seemingly insignificant movements during such monitoring can result in deviations from the baseline ECG pattern that are sufficient to unnecessarily trigger patient distress alarms.[2,11,26,30]

In ECG interpretation, one can identify two types of errors that result from these heart and body position changes. The first category includes errors that mimic disease induced changes, i.e., that create false positive results.[11] The second category includes factors that hide underlying disease or deteriorating cardiac function and thus precipitate false negative results, a situation known as "electrocardiographically silent ischemia".[8,22] Silent ischemia is much more difficult to detect and is also of greater clinical concern as failure to detect a true injury has such a high impact on patient well being. The settings in which such errors are of the greatest concern include the emergency room and intensive care units, where patient monitoring is constant and the consequences of hesitation can be costly.

Previous research has described the effects of heart position on torso-surface potentials but has lacked comprehensive statistical quantification. MacLeod *et al.* used a realistically human-shaped, electrolytic torso tank to measure the body-surface and epicardial potentials from healthy canine hearts located at various positions along three orthogonal directions within the tank.[24] They concluded that changes in heart position of only a few centimeters were sufficient to produce changes in ST-segment potentials that could mimic acute myocardial ischemic injury. In a separate study using the same approach but with a heart experiencing acute myocardial ischemia, the group showed that simple rotation of the heart position produced ECG waveforms without the characteristic features of ischemic injury and proposed a possible mechanism for clinically silent ischemia.[22] Both these studies also included simulation of geometric models derived from the torso tank to predict torso potentials from epicardial sources measured during the experiments. A limitation of these studies was that they included only on a small number of specific instances, i.e., the heart was placed in a series of fixed locations. Complete sensitivity analyses, by contrast, should include a comprehensive statistical description of the dependence of the outcome on variations of all parameters of interest. Such a study based on experiments would be prohibitively expensive and plagued with methodological challenges. Even simulation, which provides a more tractable framework for sensitivity analysis, can become prohibitive in computational cost if each test requires more than a few seconds to complete.

Many methods exist for simulation based assessment of sensitivity and their utility depends on the complexity of the underlying system. The best known and simplest is the Monte Carlo approach, which samples the entire parameter space and often results in prohibitive computational cost. A simplification of this approach known as "brute-force" methods reply on highly under-sampling the parameter space and interpolating between the results.[29] Another variation is that what is known as "range finding" experiments, in which the outer extremes of the parameter limits are evaluated and assumed to represent the total variation across the parameter range. As we will show, variation of the ECG with heart position is not linear and the maximum impacts do not occur at the extremes of the parameters, thus precluding range finding and undermining brute-force approaches. A more sophisticated variation, known as the "generalized polynomial chaos-stochastic collocation" (gPC-SC) method[33,34] is effectively a sampling method which exploits assumptions concerning the mathematical nature of the stochastic field or process of interest—assumptions which are often justified mathematically—to minimize the number of samples that are needed for the computation of accurate statistics. This approach has formed the basis of previous studies by our group[15,16] and of the results described here.

In this study, we carried out a mathematically robust sensitivity evaluation using gPC-SC to predict the effects of changes in heart location and orientation on body-surface electrocardiographic potentials have gone beyond simple case-study strategies to a systematic and quantitative approach that provides a statistical metric of parameter sensitivity which could lead to clinical improvements for ECG based diagnosis and monitoring. The findings support and enhance previously reported results from torso tank experiments by MacLeod *et al.*[22,24]

METHODS

The electrocardiographic forward problem solves for body-surface potentials given a set of known cardiac sources and the shape and conductivity of the intervening volume conductor.[19] Of the possible source models, arguably the most complete and most unique representation of cardiac activity is the time sequence of epicardial voltages,[5] which leads to a quasi-static approximation of Maxwell's equations expressed as the following classic Laplace problem:

$$\begin{aligned} \nabla \cdot (\sigma(\boldsymbol{x}) \nabla u(\boldsymbol{x})) = 0, \quad & \boldsymbol{x} \in \Omega \\ u(\boldsymbol{x}) = u_0(\boldsymbol{x}), \quad & \boldsymbol{x} \in \Gamma_H \\ \vec{n} \cdot \sigma(\boldsymbol{x}) \nabla u(\boldsymbol{x}) = 0, \quad & \boldsymbol{x} \in \Gamma_T, \end{aligned} \tag{1}$$

where Ω denotes the torso domain, consisting of the volume internal to the torso surface, Γ_T, and external to the heart surface, Γ_H. $u(\boldsymbol{x})$ is the potential, which obeys Dirichlet boundary conditions, $u_0(\boldsymbol{x})$, on the heart surface and a Neumann zero-flux condition on Γ_T. The electrical conductivity, $\sigma(\boldsymbol{x})$, is that of the volume conductor, assumed homogeneous in the experiments with the electrolytic torso tank. The outward facing normal with respect to the torso is denoted $\vec{n}$.

Geometric Model

The geometric model consisted of triangular elements that represented the heart and torso tank surfaces, as depicted in Fig. 1. The heart surface contained 670 points, of which 247 were the locations of electrodes that recorded cardiac electrical potentials in canine experiments of acute ischemia. A surface Laplacian interpolation was used to reconstruct the values for the remaining points.[28] The tank surface consisted of 771 nodes and 1538 triangular elements. Figure 1 shows the relative position of the reference heart location within the torso tank, as well as the coordinate axes of the geometry. An MRI of a healthy adult was used as a reference for the placement of the heart in the torso. The conductivity of the torso was modeled after the experimental setup of MacLeod *et al.*[22,24,25] with a homogeneous value of 500 Ω·cm, approximating the average conductivity of the torso. The coordinate system was set so that the x-axis corresponded to the lateral (left/right) direction, the y-axis to the dorsal/ventral direction, and the z-axis to the cranial/caudal direction.

Numerical Methods

To solve Eq. (1) we used the well known boundary element method (BEM),[7] which has been successfully applied to a range of electrocardiographic problems.[4,10,23,32] The result is a transformation operator, $\mathcal{F}_\Omega : v_H \rightarrow v_T$, that links epicardial to torso potentials, $u_T \in v_T : \mathcal{T}(\Gamma_T) \rightarrow \mathbb{R}$. In order to evaluate variations in torso potential resulting from uncertainties in the position of the heart, we sought solutions to the forward problem for various positions of Γ_H within Ω. We assumed linear variation of the potential over the elements that make up both surfaces[13] so that the transformation operator $\mathcal{F}_\Omega$ was a matrix that transformed the heart potentials, u_H, to the torso-surface potentials, u_T. The BEM requires computation of weighted solid angles between each collocation point and every triangular element in all surfaces and we

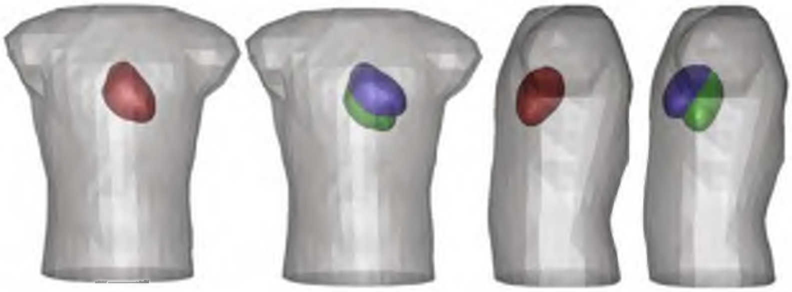

FIGURE 1. Extremes of motion of the torso tank and cardiac sources. The torso surface is grey and the epicardial surface red in the most central location. The cardiac location extremes are shown in green and blue for a pivoting motion in both *x* and *y* directions around a vector centered at the base of the heart.

employed the analytical formulas for solid angles given by de Munck[10] and the transform matrix construction scheme presented by Barr *et al.*[5] Because the solid angles change in response to affine transformations of the heart surface, the transformation operator, $\mathcal{F}_{\Omega}$, must be recomputed for each unique coordinate transformation resulting from a new heart surface location.

Experimental Methods

All experimental data were taken from previous studies that had the approval from the Institutional Animal Care and Use Committee at the University of Utah and conformed to Guide for the Care and Use of Laboratory Animals (NIH Pub. No 85-23, Revised 1996). Epicardial potentials used in the simulations were taken directly from experiments of isolated, instrumented canine hearts suspended in the human-shaped torso tank. Variable degrees of ischemia were induced by restriction of blood flow through the left anterior descending coronary artery and the epicardial potentials were recorded using 247 electrodes covering the ventricles.[24,25] We used epicardial potentials from the ST segment of the ECG during representative beats under both control and ischemic conditions.

Imaging of Cardiac Position

It was essential for these studies to set the variation of spatial parameters—heart motion arising from respiration and changes in posture—to physiologically realistic values. We obtained magnetic resonance images (MRIs) for a test subject during normal respiration in three positions; supine, prone, and lying on the right side. One set of data contained images that were cardiac gated and acquired during breath holds. To quantify a respiration induced cardiac motion, a second set of scans recorded ungated, cine MRI in supine and the right side positions. The scans were registered together in order to measure the changes in heart orientation.

From these images, we derived the following constraints: (1) apical motion in the axial plane restricted to a maximum end-to-end deviation of 6 cm, achieved through a pendulum-like swinging motion about a point near the center of the base of the heart; (2) vertical translation limited to a deviation of 2 cm; (3) rotational pivoting of the heart about a vertical axis, limited to a deviation of 20°. A final assumption was that all positions have an approximately equal likelihood so that we could assume uniform probability density functions for each parameter of motion. This assumption implies that, within physiological ranges, all values of swing, rotation, and vertical translation are equally likely to occur. It does not suggest that the time the heart spends in each position is equal, just that there is no *a priori* knowledge of which positions the heart is likely to assume within the specific constraints.

Modeling Uncertainty in Heart Position

To carry out a comprehensive and quantitative sensitivity analysis of the role of heart position on the ECG requires a combination of simulation to compute body-surface potentials from cardiac sources, as well as an efficient strategy to capture statistical variation in the model variables. The simulation model, described below, is a solution to the forward problem of electrocardiography based on source potentials on the outer (epicardial) surface of the heart.[5] Implemented as a boundary element discrete model, this approach allows efficient movement in heart position, which is the parameter space to explore. To capture the statistical variation, we employed the gPC-SC method for its efficiency and appropriate assumptions about the underlying system.

To formalize this process mathematically, we let $(\chi, \mathcal{A}, \mu)$ be a complete continuous probability space that expresses variation in the heart position, where χ is the event space consisting of outcomes corresponding to heart position, $\mathcal{A} \subset 2^{\chi}$ is the σ-algebra used to define measurable events, and μ is the probability measure expressing the distribution from which outcomes are drawn. We can now express the heart position as a function of four uniform independent random variables $\vec{\xi} = (\xi_1, \xi_2, \xi_3, \xi_4)$, which correspond to swing about x-axis, swing about y-axis, rotation about the long axis of the heart, and translation along the z-axis, respectively, as seen in Fig. 2. The term swing refers to the pendulum type of movement made by the heart as it pivots around its base. The random field of interest (and in particular, its statistical characterization) in this study is the torso-surface potential. The heart position can be completely expressed in terms of $\vec{\xi}$, and because the torso-surface potential is a direct consequence of heart position, the torso potential can also be expressed as a function of $\vec{\xi}$. We can denote the torso potential by $f(\vec{\xi})$. We are interested in computing statistics on the random field $f(\vec{\xi})$ with the mean of the field given by $\mathrm{mean}(f) = \mathbb{E}[f(\vec{\xi})]$ and the variance by $\mathrm{var}(f) = \mathbb{E}[(f(\vec{\xi}) - \mathrm{mean}(f))^2]$.

The stochastic collocation approach selects a collection of sample points for the random field and applies a set of corresponding weights that account for the probability density function characteristics of the set from which the points (or outcomes) are drawn. In this case, each collocation point, $\vec{\xi}_j$, represented a particular heart position selected from the outcome set. At each collocation point we computed the torso

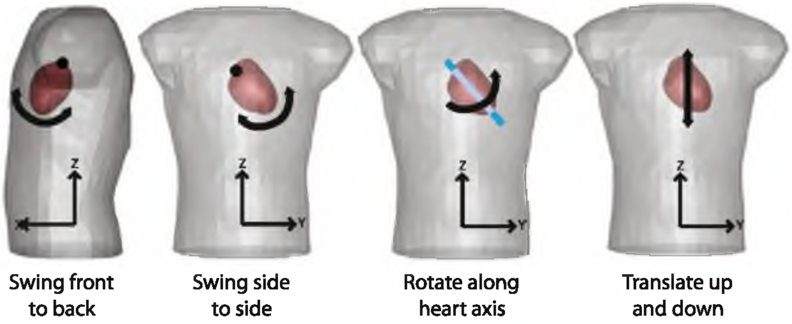

FIGURE 2. Modes of motion. ξ_1 = swing front to back, ξ_2 = swing side to side, ξ_3 = rotation along the long axis of the heart, and ξ_4 = translation along the *z*-axis.

potential field, $f(\vec{\xi}_j)$, by traditional ECG forward solution techniques (described above). Unlike traditional Monte Carlo, in which very large numbers of collocation points are required to compute accurate statistics, only a limited number of samples are necessary by utilizing the smoothness assumption to select points and weights without loss of accuracy (achieving as much as 400 times speed-up in test simulations).

Statistical Analysis

Once solutions (torso potentials) were computed for each heart position dictated by the collocation sampling, the statistics of these solutions were given by the following expressions:

$$\begin{aligned} \operatorname{mean}(f) &= \mathbb{E}[f(\vec{\xi})] \approx \sum_{j=1}^{q} w_j f(\vec{\xi}_j) \\ \operatorname{var}(f) &= \mathbb{E}[(f(\vec{\xi}) - \operatorname{mean}(f))^2] \\ &\approx \sum_{j=1}^{q} w_j (f(\vec{\xi}_j) - \operatorname{mean}(f))^2, \end{aligned} \tag{2}$$

variable, and w_j denotes the weights. For this study, we utilized second-order Smolyak collocation points and weights for independent and uncorrelated uniform distributions, which required $q = 5$ points for a single random dimension, $q = 13$ points for two, $q = 25$ points for three, and $q = 41$ points for four random dimensions.[31,33,35] The points and weights were based on Smolyak's first algorithm and more details are available elsewhere,[36] including discussion of further statistics that can be computed beyond mean and variance using the collocation approach. As in other applications, larger values of standard deviation (STD) at particular points on the torso surface indicated a larger sensitivity of the ECG at those points to variations in the associated modes of cardiac swing, rotation, or translation.

Range Finding Evaluation

Stochastic Collocation methods are an effective tool for a specific class of numerical problems because the gPC-SC relies on the underlying probability distribution being continuous. Moreover, if variations within the parameter space produce nearly linear results, then the added complexity of the collocation methods may not be justified and a range finding approach may be sufficient. To evaluate the utility of the range finding approach to sensitivity analysis in this problem, we carried out simulations of the ECG at lead V_4 for different ranges of cardiac motion constrained as described above. For each of 20 positions uniformly spaced between the extremes, we computed a forward transform matrix and applied epicardial potentials from the ST segment. The results were plotted to demonstrate the response of the system for one sample parameter.

RESULTS

Figure 3 shows a reconstructed ECG from the V_4 location from epicardial potentials recorded during conditions that produced ischemia. The resulting elevation of the ST segment is obvious, as is the large amplitude of the ECG (approximately 5 mV peak to peak for the QRS complex). The amplitude of ECGs from the experimental preparation was determined by the conductivity of the electrolyte tank in which the heart was placed, and they could not perfectly replicate the conditions in humans. The figure also shows the time point used to capture ST-segment shifts (40% of the time between the QRS and T waves) based on the root mean square (RMS) curve of the measured electrograms. All subsequent displays of body-surface potentials maps were based on the value recorded at this time point. The ECG also shows the typical, shifted ischemic ST segments relative to a TQ segment that was adjusted for each beat to define a flat baseline, as is customary with ECG recordings.

Figure 4 contains the results of the range finding evaluation for the V_4 position and heart swing in two orthogonal directions. The shape of the resulting curves shows that variation of ECG amplitude is neither linear nor monotonic over the range of motion. Moreover, the peak variations do not arise at either extreme of motion, but somewhere in the middle of the range. These results suggest that simple schemes like range finding or brute force will capture only part of the true variation and that a comprehensive sensitivity analysis is justified.

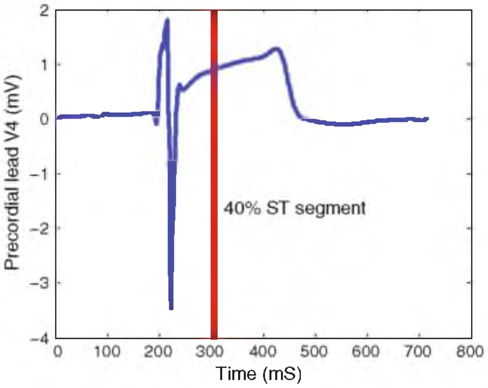

FIGURE 3. Reconstructed ECG for precordial lead V_4. The ECG signal was reconstructed using the BEM from epicardial potentials captured during the late phase of a 180-s episode of elevated heart rate and reduced coronary blood flow. The red line indicates the time of 40% of the ST segment, the time instant used for all subsequent displays of body surface-potential maps below.

Figure 5 depicts an example of ST-segment torso potentials computed from measured epicardial potentials. The baseline map represents the torso potentials computed from epicardial potentials during control conditions, i.e., without induced ischemic injury. The ischemic tank potentials show the obvious changes that arise from using measured heart potentials recorded during an episode of induced acute ischemia. The lower row of the figure contains computed tank potentials from ischemic epicardial potentials, for the two extreme positions of one mode of heart motion: front/back swing (±17.5°) as seen in Fig. 1. The torso potentials, computed at maximum backswing, would be difficult to distinguish from those computed from control conditions shown at top left panel—a case that could result in a false negative diagnosis.

While Fig. 5 shows torso potentials from the extreme positions of a single mode of motion, the STD maps shown in Fig. 6 provide a more comprehensive report of the sensitivity throughout the entire range of motion for all parameters. For example, the SD map for swinging front-to-back in the case of ischemia shows large STDs for leads V_2, V_3, and V_4 with values of 0.40, 0.37, and 0.29 mV, respectively, and only moderate SD values for V_1 and V_5 at 0.11 and 0.17 mV. Figure 6 also contains the quantitative results for each of the modes of motion and for both ischemic and nonischemic epicardial potentials.

Observations from this figure summarize general findings about the effect of heart position on the ECG. For example, the precordial areas—and hence the precordial electrodes (V_1–V_6)—would be specifically sensitive to swinging around either of the x or y-axes,

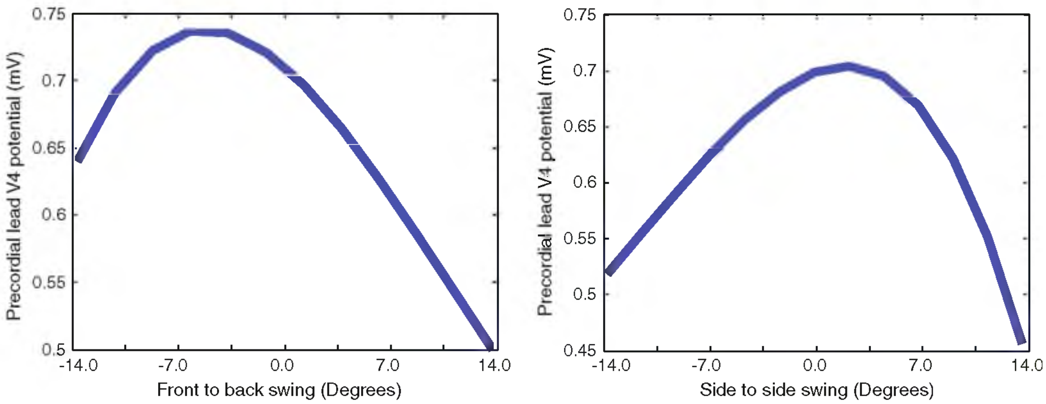

FIGURE 4. Sampling of the front-to-back swing and the side-to-side swing on the recordings of precordial lead V4. The left figure shows the effects of 20 sample points for front-to-back heart with a maximum value at −6.5°. At right, the figure demonstrates the case of side-to-side cardiac swinging motion. Both figures illustrate the nonlinear nature of the parameter space.

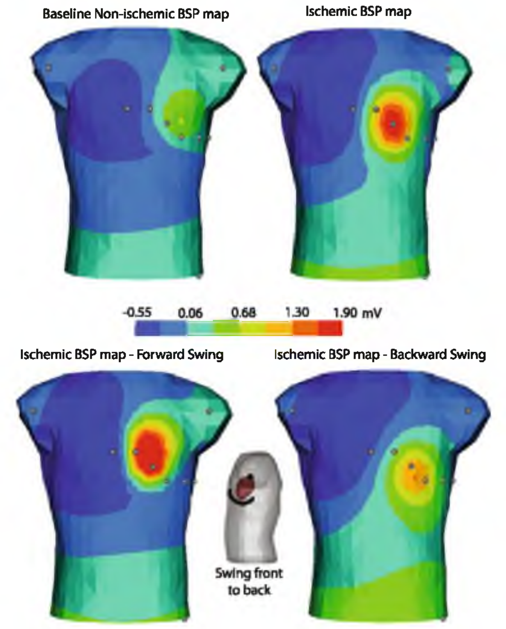

FIGURE 5. Effect of heart position shift on ST segments during ischemic injury. The top left panel depicts the torso potentials for the baseline condition obtained from the epicardial potentials with normal blood flow. Top right panel shows the torso potentials obtained from epicardial potentials recorded during acute ischemia. The bottom row shows the torso potentials in response to the ischemic heart swinging forward and backward to reasonable physiological limits, ±17.5°.

i.e., antero-posterior or lateral movement of the apex. Moreover, combinations of antero-posterior swing and vertical translation caused some of the largest STDs, indicating very high sensitivities to this type of motion. Such motion would occur when a patient rolls over in bed or sits up and then lies back down. Translation in the vertical (z) axis, perhaps as expected, produced changes above and below the precordial areas and thus would be better detected in the limb leads. This type of motion was evident during respiration but produced very low STDs. Pivoting motions around the long axis of the heart produced similarly low variations in tank-surface potentials. Thus, it appears particularly unlikely that pivoting of the heart about the long axis or translations along the z-direction would be sufficient to produce significant errors in the ECG during ischemia. However, the STDs of the torso potentials due to swinging motions were large enough at 0.3 mV or more, that it would be possible to measure substantial ST-segment elevations in leads V_3 and V_4, even for the case of nonischemic epicardial potentials (upper row of Fig. 5). Such a result suggests the possibility of a false positive detection of ischemic injury.

DISCUSSION

The goal of the study was to evaluate the role of positional changes of the heart in the setting of acute myocardial ischemia through statistical sensitivity analysis using the gPC-SC methodology. This approach provides advantages over other methods reported in the setting of electrocardiography.[3,9,20] We have also shown that the parameter sensitivity of the problem is neither linear nor monotonic, thus justifying the need for an unbiased statistical approach like the gPC-SC. Statistical methods provide detailed quantitative results, including the spatial maps of STD for any distribution of parameter variation, examples of which appear in Fig. 6. Our results both support and refine previously reported clinical findings and suggest specific heart motions that are likely to cause substantial errors in ECG monitoring and diagnosis.

The results summarized in Figs. 5 and 6 illustrate both the power of the gPC-SC approach and its utility in quantifying complex relationships. We evaluated the twin hypotheses that shifts in heart position can cause (a) false positive or (b) false negative monitoring errors and could predict which ECG leads would be most susceptible to such errors. No previous studies have provided this level of spatial detail or a probabilistic metric of the error possible from such a variation in system parameters. The STD maps are a novel means to summarize parameter sensitivity in electrocardiography. They represent the spatial extent and magnitude of possible shifts in potentials induced by variation in one or more modes of heart movement. Just as one often assigns two or three times the STD (for a Gaussian distribution) to encompass the full extent of variation that is likely in a single random variable, one can picture two or three times the absolute values of the standard-deviation torso maps as the approximate range of absolute variation possible for a given set of cardiac potentials and mode(s) of motion.

The results of the sensitivity study indicate that some modes of heart motion are capable of both obscuring ST elevations as well as mimicking them. Rotation around the long axis of the heart is a component of normal cardiac contraction; translation up and down mimics a major component of respiratory motion. Neither mode of motion produced significant variations in the ECG, with STD less than 0.1 mV, suggesting that if such findings came from a realistic, patient based model, they need not be of concern to clinicians. In contrast, the motions of swinging front-to-back and side-to-side both produced STDs of more than 0.3 mV, larger than the ST shifts of 0.2 mV that are considered clinically significant. Such swinging occurs, for example, when a subject lies down, sits up, or leans forward. And while postural changes can

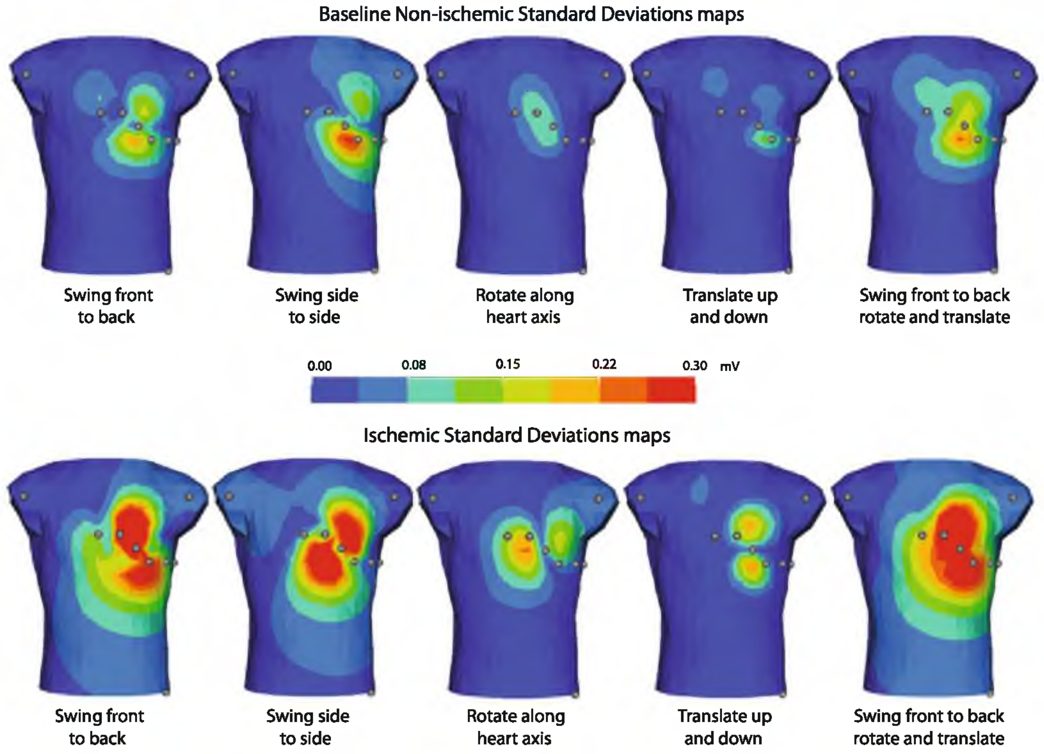

FIGURE 6. Standard deviation of tank-surface potentials resulting from heart position shift during ischemia. The top row shows the SD from the motion of a heart with control epicardial potentials. The bottom row shows the SD of tank surface potentials from the motion of a heart with ischemic epicardial potentials. Colored dots indicate locations of standard limb and precordial leads.

readily be controlled in an emergency room or other acute setting, they represent a more elusive problem for critical care, in which monitoring continues over hours or days and patient motion is common. With knowledge of the specific results of postural changes, one could imagine clinical tests in which a patient were articulated in ways that could increase the sensitivity to ischemia; thus the test sensitivity and specificity might be improved. Conversely, mechanical sensors on a critically ill patient could record postural changes and adjust ECG monitoring to account for the associated changes in ECG sensitivity and reduce the incidence of false positives, as other have proposed.[27]

In order for cardiac motion to create false positive findings of ST-segment shifts in the ECG, it is necessary that there exist during the plateau phase of the action potential at least small cardiac potential differences that project to the torso surface. Even during the nominally isopotential period of the plateau phase, there exist differences in voltage across the heart because of variations in action potential amplitude and timing. Such differences create currents that are small but detectable on the cardiac surface and the body surface, as reflected by the need to set thresholds for clinically meaningful ST-segment potentials.[17]

The STD represents a statistical expectation of the possible range of the quantity of interest, in this case ECG potentials. It does not indicate which specific values of the system parameters, in this case heart motion, will generate extremes of that range. In some cases, basic biophysical relationships will provide the necessary intuition to explain, for example, enhancement of anterior body-surface potentials when the heart moves closer to the front of the chest. But for others (e.g., the swinging motion we have explored), the maximum deviation of the body-surface potentials occurs not at the extremes of motion, but somewhere in the midrange. The SD maps indicate the extent of possible variations but further exploration is necessary to identify the actual parameter values (heart position) that would create such variations.

We have assumed a uniform distribution of the input parameters of the simulation, the heart-motion values, because there is no data available to suggest otherwise.

The uniform distribution assumes that any particular value of heart rotation, swing, or translation is equally likely to occur, but not that the heart spends equal time in each position. One notable feature of the gPC-SC method is that it supports any assumed probability density function. If data became available or one wished to test other assumptions about the distribution of heart positions, this information could be included by using the appropriate probability density function.

Our approach does not account for the impact of variations in heart position and orientation upon the epicardial potentials because these potentials are assumed to be constant regardless of the heart position, an assumption supported by previous experimental studies from members of our group.[24] The gPC-SC approach presented here could, however, be easily modified to include such changes in the source potentials. Our formulation also did not account for consequences of the deformation of the heart during postural changes. However, such effects would likely increase the variability of the system, and our conclusions would become a conservative estimate of the variation caused by positional changes.

The primary objectives of this study were to describe a quantitative sensitivity approach that has not been reported previously for this problem and then carry out a study using cardiac potentials measured from a torso tank experiment in order to augment previous qualitative analyses.[24] The advantages of this approach compared to one based on artificial or estimated cardiac sources embedded in a realistic or patient specific human torso model are twofold. First, the cardiac sources available from experiments, although from an animal model, are highly realistic and capture normal and ischemic conditions that arise during physiologically realistic conditions. Secondly, the volume conductor in these simulations was based on a very accurate (within 5 mm) measurement of a rigid electrolytic tank and the heart position in the tank, thus preserving a geometric accuracy rarely achievable even from medical imaging of a human subject. Moreover, the *conductivity* of the volume conductor in such an experimental preparation can be set very precisely, removing an additional source of ambiguity that arises in a patient specific model.

This approach also presents limitations to interpreting the results of such a study, especially when extrapolating to the clinical domain. The model of the electrolytic tank is homogeneous and thus the effects of organs or other variations in tissue conductivity cannot be evaluated. Similarly, changes in the shape of both the internal organs and the torso as a whole due to respiration or changes in posture are not included in a model based on a rigid, homogeneous torso tank. A model that did include all these variations would also depend on many approximations, e.g., conductivity values and distortions of soft tissue shape during cardiac and respiratory motion and postural changes. A quantitative and statistical parameter sensitivity evaluation under such conditions would require a sophistication of model construction and variation that would likely be prohibitive. There are very few reports of cardiac simulations that even include cardiac contraction and none to our knowledge that include respiration and postural changes. No matter which modeling paradigm or level of realism one wishes to pursue, the framework of gPC-SC can accommodate and provide a method for quantitative sensitivity analysis as long as boundaries among the heart and other organs in the thorax are respected.

One indication of the physiological reasonableness of our results comes from a comparison with previously reported experiments,[24] in which a canine heart was suspended in the same, human shaped, electrolytic tank. Variations in due to positional changes heart position 6 cm side-to-side.[24] The gPC-SC method computed similar results with STDs of up to 0.25 mV, as shown in Fig. 5. A different study by Garcia *et al.* measured ST_{60} and T-wave amplitude as a function of body position and found large variations among patients.[14] The maximum variation of torso potentials after a positional change from the left side to supine, was 188 μV for the ST segment and 686 μV during the T wave. The results simulated for the gPC-SC method, 350 μV STD for the T wave and 250 μV STD for the ST_{60} amplitude, were well within this range for the T-wave amplitude, and just outside their extremes for ST_{60}. It is reasonable to expect that our modeling approach would correlate better with the tank experiments, which make the same assumptions of geometry and tissue conductivity, than with the results of patient studies.

These results and our previous studies of the effects of variations in tissue conductivities[15] support the further use of the gPC-SC technique—and parameter sensitivity studies in general—for this problem domain. There is a clear need to improve the diagnostic robustness of the ECG, especially in the setting of emergency and critical care medicine, and our results point to sources of variation that are large enough to explain at least some of the errors that arise in clinical practice. These findings also suggest some possible means of adjusting current practice to accommodate for heart motion, or even to use explicit movements to reveal otherwise subthreshold abnormalities in ECG metrics.

ACKNOWLEDGMENTS

The authors would like to thank Dr. Dongbin Xiu of Purdue University (USA) for his generous help with generalized polynomial chaos and Dr. Tom Fletcher for his mathematical insights. We also appreciate the input on clinical electrocardiography from Ravi Ranjan, MD/PhD and Chris McGann, MD. We also gratefully acknowledge the computational support and resources provided by the Scientific Computing and Imaging Institute. This work was funded by a University of Utah Seed Grant Award, NSF Career Award (Kirby) NSF-CCF0347791, NSF IIS-0914564, and the NIH NCRR Center for Integrative Biomedical Computing (http://www.sci.utah.edu/cibc), NIH NCRR Grant No. P41-RR12553-12. Support for the acquisition of the experiment data came from the Nora Eccles Treadwell Foundation.

REFERENCES

[1] Adams, M. G., and B. J. Drew. Body position effects on the ECG: implication for ischemia monitoring. *J. Electrocardiol.* 30:285–291, 1997.

[2] Adams-Hamoda, M. G., M. A. Caldwell, N. A. Stotts, and B. J. Drew. Factors to consider when analyzing 12-lead electrocardiograms for evidence of acute myocardial ischemia. *Am. J. Crit. Care* 12(1):9–16, 2003; quiz 17–8.

[3] Amoore, J. N., Y. Rudy, and J. Liebman. Respiration and the ECG: a study using body surface potential maps. *J. Electrocardiol.* 21(3):263–271, 1988.

[4] Barnard, A. C. L., I. M. Duck, and M. S. Lynn. The application of electromagnetic theory to electrocardiology: I. Derivation of the integral equations. *Biophys. J.* 7:433–462, 1967.

[5] Barr, R. C., M. Ramsey, and M. S. Spach. Relating epicardial to body surface potential distributions by means of transfer coefficients based on geometry measurements. *IEEE Trans. Biomed. Eng.* 24:1–11, 1977.

[6] Birnbaum, S. L., Y. Hale, and R. A. Kloner. Changes in R wave amplitude: ECG differentiation between episodes of reocclusion and reperfusion associated with ST-segment elevation. *J. Electrocardiol.* 30:211–216, 1997.

[7] Brenner, S., and R. L. Scott. The Mathematical Theory of Finite Element Methods (2nd ed.). New York, NY: Springer-Verlag, 2002.

[8] Bridges, S. L., J. S. Hollowell, S. W. Stagg, K. A. Kemle, M. L. Nusynowitz, D. C. Allensworth, D. B. Pryor, and J. R. Moorman. Is silent ischemia on the routine admission ECG an important finding? *J. Electrocardiol.* 26(2):131–136, 1993.

[9] Charulatha, R., and Y. Rudy. Electrocardiographic imaging: I. Effect of torso inhomgeneities on body surface electrocardiographic potentials. *J. Cardiovasc. Electrophysiol.* 12:229–240, 2001.

[10] de Munck, J. C. A linear discretization of volume conductor boundary integral equation using analytically integrated elements. *IEEE Trans. Biomed. Eng.* 39(9):987–990, 1992.

[11] Drew, B. J., and M. G. Adams. Clinical consequences of ST-segment changes caused by body position mimicking transient myocardial ischemia: hazards of ST-segment monitoring. *J. Electrocardiol.* 34(3):261–264, 2001.

[12] Drew, B. J., and M. W. Krucoff. Multilead ST-segment monitoring in patients with acute coronary syndromes: a consensus statement for healthcare professionals. ST-segment monitoring practice guideline international working group. *Am. J. Crit. Care* 8(6):372–386, 1999; quiz 387–8.

[13] Ferguson, A. S., and G. Stroink. Factors affecting the accuracy of the boundary element method in the forward problem I: calculating surface potentials. *IEEE Trans. Biomed. Eng.* 44(11):1139–1155, 1997.

[14] García, J., M. Astrõm, J. Mendive, P. Laguna, and L. Sörnmo. ECG-based detection of body position changes in ischemia monitoring. *IEEE Trans. Biomed. Eng.* 50(6):677–685, 2003.

[15] Geneser, S. E., R. S. MacLeod, and R. M. Kirby. Application of stochastic finite element methods to study the sensitivity of ECG forward modeling to organ conductivity. *IEEE Trans. Biomed. Eng.* 55(1):31–40, 2008.

[16] Geneser, S. E., D. B. Xiu, R. M. Kirby, and F. B. Sachse. Stochastic Markovian modeling of electrophysiology of ion channels: reconstruction of standard deviations in macroscopic currents. *J. Theor. Biol.* 245(4):627–637, 2007.

[17] Goldberger, A. L., and E. Goldberger. Clinical Electrocardiography. St. Louis: C.V. Mosby, 1986.

[18] Grosse-Heitmeyer, W. Is there a specific response of the ECG R-wave amplitude to exercise induced myocardial ischemia? Exercise test and dipyridamole test. *Schweiz. Med. Wochenschr.* 123:414–421, 1993.

[19] Gulrajani, R. M. The forward and inverse problems of electrocardiography. *EMBS Mag.* 17(5):84–101, 1998.

[20] Huiskamp, G. J. M., and A. van Oosterom. The effect of torso inhomogeneities on body surface potentials. *J. Electrocardiol.* 22:1–20,1989. .

[21] Lexhava, M. G., N. Khvichiia, and K. V. Iosava. Assessment of the diagnostic significance of R wave amplitude changes in patients with ischemic heart disease in computer-assisted monitoring analysis of ECG during treadmill tests. *Kardiologiia* 30:63–65, 1990.

[22] MacLeod, R. S., R. L. Lux, and B. Taccardi. A possible mechanism for electrocardiographically silent changes in cardiac repolarization. *J. Electrocardiol.* 30(Suppl.):114–121, 1997.

[23] MacLeod, R. S., R. M. Miller, M. J. Gardner, and B. M. Horáček. Application of an electrocardiographic inverse solution to localize myocardial ischemia during percutaneous transluminal coronary angioplasty. *J. Cardiovasc. Electrophysiol.* 6:2–18, 1995.

[24] MacLeod, R. S., Q. Ni, B. Punske, P. R. Ershler, B. Yilmaz, and B. Taccardi. Effects of heart position on the body-surface ECG. *J. Electrocardiol.* 33(Suppl.):229–238, 2000.

[25] MacLeod, R. S., B. Taccardi, and R. L. Lux. Electrocardiographic mapping in a realistic torso tank preparation. In: Proceedings of the IEEE Engineering in Medicine and Biology Society 17th Annual International Conference. New York: IEEE Press, 1995, pp. 245–246.

[26] Madias, J. E. Comparability of the standing and supine standard electrocardiograms and standing sitting and supine stress electrocardiograms. *J. Electrocardiol.* 39:142–149, 2006.

[27] Nelwan, S. P., S. H. Meij, T.B. van Dam, and J. A. Kors. Correction of ECG variations caused by body position changes and electrode placement during ST-T monitoring. *J. Electrocardiol.* 34:213–216, 2001.

[28] Oostendorp, T. F., A. van Oosterom, and G. J. Huiskamp. Interpolation on a triangulated 3D surface. *J. Comput. Phys.* 80:331–343, 1989.

[29] Seigneur, S., T. W. Teche, R. M. Roth, and L. E. Reid. Sensitivity of complex urban air quality model to input data. *J. Appl. Meteorol.* 20:157–177, 1981.

[30]Shusterman, V., A. Goldberg, D. M. Schindler, K. E. Fleishcmann, R. L. Lux, and B. J. Drew. Dynamic tracking of ischemia in the surface electrocardiogram. *J. Electrocardiol.* 40:S179–S186, 2007.

[31]Smolyak, S. Quadrature and interpolation formulas for tensor products of certain classes of functions. *Soviet Math. Dokl.* 4:240–243, 1963.

[32]Stinstra, J. G. The Reliability of the Fetal Magnetocardiogram. PhD thesis, Universiteit Twente, Enschede, Netherlands, 2001.

[33]Xiu, D. Efficient collocational approach for parametric uncertainty analysis. *Commun. Comput. Phys.* 2(2):293–309, 2007.

[34]Xiu, D. B. Fast numerical methods for robust optimal design. *Eng. Opt.* 40(6):489–504, 2008.

[35]Xiu, D. B., and J. S. Hesthaven. High-order collocation methods for differential equations with random inputs. *SIAM J. Sci. Comput.* 27(3):1118–1139, 2005.

[36]Xiu, D. B., and J. Shen. An efficient spectral method for acoustic scattering from rough surfaces. *Commun. Comput.* 2(1):54–72, 2007.

CHAPTER 7

CONCLUSIONS

Computational modeling and simulation is a powerful tool that has great potential to help improve understanding of mechanisms and eventually diagnosis and treatment of cardiac disease. The results from these three projects illustrate that there are still significant technical challenges to overcome before many of these simulations can be clinically useful. Each of the findings we have presented addresses a different technical aspect of modeling with a focus on the spatial or geometric assumptions of subject specific modeling of cardiac bioelectric fields. Each study also underscored the potential for modeling and simulation to address aspects of importance to the study and clinical application of bioelectric fields.

The first study presented in this dissertation explored the role in simulations of myocardial ischemia of the border zone, *i.e.,* the transition from normal to under-perfused tissue in the heart. The results of this study suggest that even subtle features like the spatial profile of the transition of transmembrane potential across the border zone can have dramatic impact on the accuracy of simulations. One novelty of the study was the use of high resolution three-dimensional measurements and subject specific modeling techniques to compare simulations directly to the experimental results. With this paradigm, we could evaluate existing bioelectric source models of ischemia and then propose improvements that resulted in a better match to measured heart-surface potentials. These improvements represent more than a mathematical or numerical refinement in that they also suggest novel physiological insights into ischemic disease. Our findings suggest that the transition between healthy and ischemic tissues is more complicated and spatially heterogeneous than previously reported which, in turn, suggests the need for a more refined evaluation of ECG recordings especially of nontransmural acute ischemia. There are many reports of the nonspecific interpretation afforded by ST depression on the body surface and our findings suggest that the spatial organization of the boundary between ischemic and healthy tissue could contribute substantially to this vagueness. Thus what started as a technical consideration of the best way to represent one aspect of the simulation domain has become a stimulus to consider a set of much more physiological questions regarding the ischemic substrate.

These specific findings that the ischemic border zone is a complex, heterogeneous boundary lead naturally to the second study in this dissertation, the numerical counterpart of the role of boundary representations in discrete geometric models used for simulation. In the boundary conforming mesh study, we found that simply increasing the resolution and degrees of freedom of the geometric model for three different problems did not always improve the solution. The answer to the apparent paradox appears to be that more sophisticated solutions, such as meshing algorithms that can conform to internal material interfaces, greatly improve the accuracy even of very coarse meshes. This technical solution allowed us to create more accurate simulations while also reducing computational cost.

The third study also followed logically from the previous two in that one needs a means of evaluating the effects of uncertainty in all aspects of the geometric assumptions or simplifications of a realistic numerical model. The variety of forms of this uncertainty and the additive, and possibly nonlinear, effects of multiple sources of uncertainty require a sophisticated approach. We found such an approach in the polynomial chaos and stochastic collocation techniques we applied to forward problems of electrocardiography. Using this very generalizable approach we found that many simulation parameters, even those that are not accessible to direct measurement, can be explored using stochastic modeling. From this study we demonstrated a framework that utilizes a relatively novel stochastic method to quickly and accurately account for the variation seen in modeling parameters. This framework is adaptable for many numerical approaches and we were able to apply it to the boundary element methods for use in the cardiac surface based formulation of the forward problem in electrocardiography. The novel contributions of this study included a quantitative assessment of the impact of realistic movements of the heart on the ECG and specifically on features of the ECG used clinically to monitor patients with ischemia. As with the other studies, this one underscored the utility of simulation in the clinical use of bioelectric field monitoring and interpretation.

7.1 Computational Mesh Requirements for Bioelectric Field Problems

Throughout this dissertation we have generated volumetric (for finite elements) and surface (for boundary element) meshes to solve a range of cardiac bioelectric problems. One of the primary conclusions of this work is that what constitutes a high quality mesh is highly problem specific. In this section we discuss the meshing requirements of three different types of problems in the setting of cardiac electrophysiology: high resolution/propagation modeling, medium resolution/electric fields, low resolution/inverse problems.

7.1.1 Propagation Models

The first consideration for constructing high quality meshes in the context of propagation models was to determine the appropriate mesh resolution needed to accurately describe the spatial domain. Modeling electrical propagation through the heart requires a very high resolution mesh, with internodal spacing well below 1 mm. For a human heart, for example, a 0.2 mm resolution produces a model with on the order of 80 million nodes which must be solved over tens of thousands of iterations to simulate a single cardiac cycle. The highly resolved models are necessary to capture the very sharp gradient that result at the activation front that propagates through the heart. Simulations based on such very large models have huge computational costs and take weeks to months to solve without the aid of very large supercomputers.

In these simulations the conduction velocity of the propagating wave is dependent on both the distance between nodes and the associated conductivity. It is common practice to adjust the conductivity of a specific tissue type in order to “tune” the conduction velocity of the model to what is seen in literature. However, this approach assumes that there is a fairly uniform spacing between nodes. Even small irregularities in node space or element shape can cause portions of the advancing wave to accelerate or decelerate becoming significant source of error. In addition, the meshing study in Chapter 5 indicated that meshes that did not accurately represent the smoothness of a boundary between tissues could be another source of error. However, the errors arising from the changes in conduction velocity were an order of magnitude larger than those seen due to nonconforming boundaries.

The results from Chapter 5 indicate that creating boundary conforming geometry is not the only meshing consideration that affects the simulation accuracy. In the reaction diffusion bidomain models inconsistent distances between nodes, or varied edge lengths, had a much larger impact on the simulation than did the conforming boundaries. In this case well shaped and uniformly sized elements or even structured grids could be used to produce more accurate simulations even though the boundaries are nonconforming. Simplified meshes such as structured meshes have many advantages over unstructured meshes such as they are much easier to create and easier to solve computationally. These simplifications result in dramatically improved computational times without an increased computational error.

7.1.2 Simulation of Static Bioelectric Fields

This section focuses on the meshing requirements for calculating electrical fields at a single time instance which can differ from those in the preceding section due to a quite different set of constraints and requirements. Examples of this sort of problem include the static bidomain, monodomain, or simple volume conductor problems. Typical of this category of problems is that the spatial domain is usually large compared to tissue simulations but that they contain no explicit time dependence, *i.e.,* no propagation or evolving source. Even if the source does change with time, the problem is linear so that it needs only to be fully solved once. As a result, computational efficiency is slightly less important compared to capturing details of the spatial domain and any heterogeneities it contains.

In general these problems do not require the very high resolution of the propagation models. As with most numerical solutions of problems over space, the resolution requirements depend on the size of gradients that arise. Typically, in such whole heart or volume conductor simulations, the node spacing is on the order of 0.7–1.5 mm, sufficient to simulate the electric field over the entire heart. In some cases, such as modeling cardiac defibrillation, local refinement must be performed around the shock electrodes in order to account for the large gradients that occur at such interfaces, where the rest of the model can be relatively coarsely resolved.

In addition to resolution, we found that modeling many diseases, such as ischemia or infarction, requires accurate geometric representations of the interface between diseased and healthy tissues. In these cases, boundary conforming meshes are critical to the underlying mesh structure. More generally, we found that boundary conforming meshes produced more accurate simulations in all cases and were particularly important when either the interface was between a source and a volume conductor or the area of interest in the simulation was at or near a material interface.

7.1.3 Mesh Requirements for Solving Bioelectric Inverse Problems

As a category, inverse problems differ substantially from the forward problems discussed so far. Inverse problems are almost always based on an associated forward problem but require either multiple (often many) iterations of that forward problem or the application of constraints to deal with their often ill-posed nature. In both the high and medium resolution forward models described above there is a relatively clear tradeoff between accuracy and computational cost, however, for inverse simulations this is not necessarily the case. In inverse problems, the trade off is much less predictable because, for example, increasing the number of nodes generally worsens the conditioning of the resulting matrix that has to be solved (inverted) numerically, thus reducing accuracy. As a result, the trade off is between accurately representing the geometry and using the fewest nodes possible.

The altered numerical constraints also drive altered meshing priorities. In this case, the meshing algorithms need to preserve major geometric features and produce well shaped elements while also minimizing the number of nodes being used, which is a relatively rare set of requirements for meshing algorithms. As a result, mesh decimation algorithms are often employed after the original mesh is constructed; in some cases, heavy manual guidance is required to achieve suitable mesh quality. In both instances the results are not as optimal as a carefully designed meshing algorithm could produce. The resulting meshes share the weaknesses of being costly to construct and of having no quantifiable guarantees of quality or precision.

7.2 Future Work

The field of patient-specific modeling is advancing very quickly as is the more general field of personalized medicine. With these advances, especially in the use of image based modeling, clinical applications are slowly emerging [157, 176]. As in all application domains, in the field of electrocardiology there remain technical challenges to widespread acceptance and use of simulation approaches. The following sections address some of these outstanding challenges.

7.2.1 Border Zone

In this work we developed a new description of the electrical changes that occur during myocardial ischemia. While this description is already very important in modeling the forward problem, its largest impact could emerge in the setting of mathematical inverse calculations to identify and locate early stages of myocardial ischemia from the body surface. Inverse solutions represent a powerful tool to noninvasively detect and also localize myocardial ischemia within the heart itself, a goal that has driven (and frustrated) electrocardiographers for 50 years [140]. Electrocardiographic inverse problems are highly ill-posed and require additional constraints to limit the solutions to be physiologically reasonable. Our new definition of ischemic border zones represents both a novel, parameterized source formulation and also a highly realistic constraint in this highly relevant inverse problem.

The simulation results indicating the requirement for the inclusion of a transition region and a complex heterogeneous border zone, suggesting that the complexity of the perfusion system and metabolic needs in the ischemic zone may likely be the key to understanding epicardial potential distributions during nonftransmural ischemia. To further investigate this hypothesis requires better solutions to a few technical challenges in both imaging of the microvasculature and registration techniques of the electrical plunge needles to the anatomical scans. Currently, we do not capture sufficient resolution to accurately identify the microvasculature. One approach that provides at least the potential for measurements of perfusion is the use of fluorescent microspheres, which could become part of our experimental protocol. Using this technique we could study the changes in perfusion to the heart at the scale of perhaps multiple millimeters to centimeters and correlate regional perfusion levels with our electrical measurements. A further modification to the experiment protocol would be to exchange the plunge needles for imaging markers detectable in MRI and CT scans in order to reduce errors that arise from the heart changing shape between the time of needle extraction and imaging.

7.2.2 Multimaterial Boundary Element Models

In Chapter 6 we explored the role of uncertainty in heart position on the electrical potentials on the body surface. In this study the heart was placed in an electrolytic phantom that approximated the average electrical conductance of the torso. However, in the body there are large heterogeneities in conductivities between the heart and the body surface that we did not account for. In particular, the lungs have a very small conductivity and have been shown to effect the forward BEM simulation. Future work is needed to understand the motion of the lungs relative to both body position and during respiration. Once a suitable model is created, the gPC-SC method could also account for the variations to body surface potentials due to the motion of the lungs.

7.2.3 Fiber Approximation

The orientation of local muscle fibers in the heart indicates the orientation of anisotropic conductivity of the myocardium and so is an essential element of tissue levels simulations. For our simulations, the fiber information of the heart was obtained postmortem using MRI diffusion weighted imaging or diffusion tensor imaging (DTI). As discussed previously, DTI scans of a beating heart are not currently feasible. Even in the eventual application of such simulations to human subjects, the recent project has minimized the impact of this limitation. Two approaches to estimating subject specific fiber orientation that show considerable promise are rule based methods and fiber atlases [177].

Despite this progress, what remains unclear is the sensitivity of various simulations to errors in fiber orientation. Given the current level of abstraction in state of the art simulations, researchers need to assess whether fully patient specific tensor fields are necessary or if atlas morphing is sufficient. To address this incomplete state of knowledge, the first step would be a sensitivity study similar to the study described in Chapter 6 on the effect of variation in heart position using the gPC-SC method. Because the sensitivity to conductivity tensors could be highly dependent on the type of simulation, two highly relevant candidates would be an ischemia model and a propagation model. Each study would include generating rule based fibers and parameterizing the assignment of helical angle to each element. It would then be possible to assign reasonable uncertainties to the fiber orientations in the form of probability distribution functions and then determine the statistical consequences to the simulation potentials or activation times.

7.2.4 Automation for Model Creation

Personalized medicine and patient-specific modeling have the potential to revolutionize the health care industry. In the context of the heart, simulation is emerging as a relevant tool in procedures such as ventricular ablations [178, 155]and implantation of implantable cardioverter defibrillators (ICD) [157, 179]. Many other simulations have potential for clinical applications but are limited by technical challenges such as construction of the geometric model and completing the simulations in a time frame that is useful to clinicians. Other engineering disciplines such as the aerospace industry have faced similar challenges, and have developed technical solutions such as parametric models attached to automated meshing and simulation routines (*e.g.,* AutoModeler), where details of the desired mesh, boundary conditions, and type of simulation reside as properties of the CAD model. A new geometry can be created by selecting an appropriate template from a database and then updating the parameters to "fit" the model to the specific case and then launching the meshing and simulation routines. Similar approaches could have promise in many biomedical domains, especially as more and more image based atlas projects describe human and animal anatomy in parameterized formulations.

A hallmark of early studies in cardiac simulation has been the huge cost to create appropriate geometric models. As a result, many research groups have turned to one of the very few existing models of the heart such as the Auckland dog heart[180], Oxford rabbit ventricles[181], or the visible human heart geometry[182]. Of these three only the Auckland dog heart is parametric, *i.e.,* can change shape based on input parameters. The research presented here shows that in many instances appropriate geometric approximations can be made without compromising accuracy. We also have developed a framework for evaluating the consequences of different approximations. The combination of viable, shape statistical methods to create atlases of organs like the heart and the error estimation framework that we have applied support the need for and the feasibility of a focused effort to develop a shared resource of cardiac geometric models.

There exist many technical challenges in translating this technology into clinical settings; however, with the advances in computing power, imaging technology, and understanding of basic physiology, patient-specific models may soon become a reality.

REFERENCES

[1] Hodgkin A, Huxley A: **A Quantatative Decription of Membrane Current and Its Application to Conduction and Excitation in Nerve**. *J. Physiol.* 1952, **11**:500–544.

[2] Hodgkin A, Huxley A: **The Components of Membrane Conductance in the Giant Axon of Loligo**. *J. Physiol.* 1952, **11**:473–496.

[3] Hodgkin A, Huxley A: **The Dual Effect of Membrane Potential on Sodium Conductance in the Giant Axon of Loligo**. *J. Physiol.* 1952, **11**:497–506.

[4] Neher E, Sakmann B: **Single-channel currents recorded from membrane of denervated frog muscle fibres.** *Nature* 1976, **260**(5554):799–802.

[5] Hunter P, Kohl P, Noble D: **Integrative Models of the Heart: Achievements and Limitations**. *Phil. Trans. R. Soc. Lond. A* 2001.

[6] Hunter P, Robbins P, Noble D: **The IUPS human Physiome Project.** *Pflugers Arch* 2002, **445**:1–9.

[7] Hunter P, Borg T: **Integration from proteins to organs: the Physiome Project.** *Nat Rev Mol Cell Biol* 2003, **4**(3):237–243.

[8] Gianni D, McKeever S, Yu T, Britten R, Delingette H, Frangi A, Hunter P, Smith N: **Sharing and reusing cardiovascular anatomical models over the Web: a step towards the implementation of the virtual physiological human project.** *Philos Transact A Math Phys Eng Sci* 2010, **368**(1921):3039–3056.

[9] Organization WH: **The global burden of disease: 2004 update**. Tech. rep., World Health Organization, Geneva 2004.

[10] Plank G, Zhou L, Greenstein J, Cortassa S, Winslow R, ORourke B, Trayanova N: **From mitochondrial ion channels to arrhythmias in the heart: computational techniques to bridge the spatio-temporal scales**. *Phil. Trans. Royal Soc.* 2008, **366**:3381–3409.

[11] Macleod R, Stinstra J, Lew S, Whitaker R, Swenson D, Cole M, Kruger J, Brooks D, Johnson C: **Subject-specific, multiscale simulation of electrophysiology: a software pipeline for image-based models and application examples.** *Phil. Trans. Royal Soc.* 2009, **367**(1896):2293–2310.

[12] Vigmond E, Vadakkumpadan F, Gurev V, Arevalo H, Deo M, Plank G, Trayagnova N: **Towards predictive modelling of the electrophysiology of the heart**. *J Exp. Physiol.* 2009, **94**(5):563–577.

[13] Camara O, Sermesant M, Lamata P, Wang L, Pop M, Relan J, Craene MD, Delingette H, Liu H, Niederer S, Pashaei A, Plank G, Romero D, Sebastian R, Wong K, Zhang

H, Ayache N, Frangi A, Shi P, Smith N, Wright G: **Inter-model consistency and complementarity: learning from ex-vivo imaging and electrophysiological data towards an integrated understanding of cardiac physiology.** *Prog Biophys Mol Biol* 2011, **107**:122–133.

[14] Bernabeu M, Bordas R, Pathmanathan P, Pitt-Francis J, Cooper J, Garny A, Gavaghan D, Rodriguez B, Southern J, Whiteley J: **CHASTE: incorporating a novel multi-scale spatial and temporal algorithm into a large-scale open source library.** *Philos Transact A Math Phys Eng Sci* 2009, **367**(1895):1907–1930.

[15] Vadakkumpadan F, Arevalo H, Prassl A, Chen J, Kickinger F, Kohl P, Plank G, Trayanova N: **Image-Based Models of Cardiac Structure in Health and Disease**. *WIREs Syst Biol Med* 2010, **2**(4):489–506. [Defibrillation, model building, meshing].

[16] Plank G, Neic A, Liebmann M, Hoetzl E, Mitchell L, Vigmond E, Haase G: **Accelerating cardiac bidomain simulations using Graphics Processing Units.** *IEEE Trans Biomed. Eng.* 2012, :69–69.

[17] CIBC: 2011. [ImageVis3D: A SCIRun Power App for interactive visualization of vary large image volumes. Scientific Computing and Imaging Institute (SCI), Download from: http://www.imagevis3d.org].

[18] CIBC: 2011. [BioPSE: Problem Solving Environment for modeling, simulation, image processing, and visualization for biomedical computing applications. Scientific Computing and Imaging Institute (SCI), Download from: http://www.scirun.org].

[19] CIBC: 2011. [Seg3D: Volumetric Image Segmentation and Visualization. Scientific Computing and Imaging Institute (SCI), Download from: http://www.seg3d.org].

[20] CIBC: 2011. [Data Sets: NCRR Center for Integrative Biomedical Computing (CIBC) data set archive. Download from: http://www.sci.utah.edu/cibc/software.html].

[21] Kléber A: **Resting Membrane Potential, Extracellular Potassium Activity, and Intracellular Sodium Activity during Acute Global Ischemia in Isolated Perfused Guinea Pig Hearts**. *Circ. Res.* 1983, **52**:442–450.

[22] Kleber A, Riegger C: **Electrical constants of arterially perfused rabbit papillary muscle**. *J. Physiol.* 1987, **385**:307–324.

[23] Dube B, Gulrajani R, Lorange M, LeBlanc A, Nasmith J, Nadeau R: **A computer heart model incorporating anisotropic propagation. IV. Simulation of regional myocardial ischemia.** *J. Electrocardiol.* 1996, **29**(2):91–103.

[24] Jie X, Gurev V, Trayanova N: **Mechanisms of mechanically induced spontaneous arrhythmias in acute regional ischemia**. *Circ Res* 2010, **106**:185–92.

[25] Hopenfeld B, Stinstra J, MacLeod R: **Mechanism for ST Depression Associated with Contiguous Subendocardial Ischemia**. *J. Cardiovasc. Electrophysiol.* 2004, **15**(10):1200–1206.

[26] Hopenfeld B, Stinstra J, MacLeod R: **The Effect of Conductivity on ST Segment Epicardial Potentials Arising from Subendocardial Ischemia**. *Annal. Biomed. Eng.* 2005, **33**(6):751–763.

[27] Olbrich O, Woodford-Williams E: **The effect of change of body position on the precordial electrocardiogram in young and aged subjects**. *J. Gerontol* 1953, **8**:56–62.

[28] MacLeod R, Ni Q, Punske B, Ershler P, Yilmaz B, Taccardi B: **Effects of Heart Position on the Body-Surface ECG**. *J. Electrocardiol.* 2000, **33**((supp)):229–238.

[29] Swenson D, Geneser S, Stinstra J, Kirby R, MacLeod R: **Cardiac Position Sensitivity Study in the Electrocardiographic Forward Problem Using Stochastic Collocation and BEM**. *Annal. Biomed. Eng.* 2011, **30**(12):2900–2910.

[30] Silverthorn D: **Human physiology**. *Recherche* 2009, **67**:02.

[31] Hodgkin A, Huxley A: **A quantitative description of membrane current and its application to conduction and excitation in nerve**. *Bulletin of mathematical biology* 1990, **52**:25–71.

[32] Alberts B: *Essential cell biology: an introduction to the molecular biology of the cell.* Garland 1998.

[33] Fozzard H, et al.: **Conduction of the action potential**. *Handbook of physiology* 1979, **1**:335–356.

[34] Hille B: *Ionic channels of excitable membranes*, *Volume 2.* Sinauer associates Sunderland, MA 1984.

[35] Opie L: *Heart physiology: from cell to circulation.* Lippincott Williams & Wilkins 2004.

[36] Woodbury J: **Action potential: properties of excitable membranes**. *Physiology and Biophysics* 1965, :26–72.

[37] Fozzard H, Arnsdorf M: **Cardiac Electrophysiology**. In *The Heart and Cardiovascular System.* Edited by Fozzard H, New York: Raven Press 1986:1–30.

[38] Roberts D, Hersh L, Scher A: **Influence of Cardiac Fiber Orientation on Wavefront Voltage, Conduction Velocity, and Tissue Resistivity in the Dog**. *Circ. Res.* 1979, **44**:701–712.

[39] Randall D, Burggren W, French K, Eckert R: *Eckert animal physiology: mechanisms and adaptations.* WH Freeman 2002.

[40] Li D, Li CY, Yong AC, Kilpatrick D: **Source of electrocardiographic ST changes in subendocardial ischemia.** *Circ Res* 1998, **82**(9):957–970.

[41] Fletcher GF, Flipse TR, Kligfield P, Malouf JR: **Current status of ECG stress testing**. *Curr Probl Cardiol* 1998, **23**(7):353–423.

[42] Galper BZ, Moran A, Coxson PG, Pletcher MJ, Heidenreich P, Lazar LD, Rodondi N, Wang YC, Goldman L: **Using stress testing to guide primary prevention of coronary heart disease among intermediate-risk patients: a cost-effectiveness analysis**. *Circulation* 2012, **125**(2):260–70.

[43] Aras K, Shome S, Swenson D, Stinstra J, MacLeod R: **Electrocardiographic Response of the Heart to Myocardial Ischemia**. In *Computers in Cardiology 2009* 2009:105–108.

[44] Hearse D: **Myocardial ischemia: can we agree on a definition for the 21st century**. *J. Cardiovasc. Res.* 1994, **28**:1737–1744.

[45] Reimer K JR: *Myocardial Ischemia, hypoxia and infarction.* New York: Raven Press 1992.

[46] Wolferth C, Bettet S, Livezey M, et al: **Negative displacement of the RS-T segment in the electrocardiogram and its relationships to positive displacement: An experimental study.** *Am Heart J* 1945, **29**(220).

[47] Selker HP: **Coronary care unit triage decision aids: how do we know when they work?** *Am J Med* 1989, **87**(5):491–493.

[48] Janse M, van Capelle F, Morsink H, Kleber A, Wilms-Schopman F, Cardinal R, d Alnoncourt C, Durrer D: **Flow of "injury" current and patterns of excitation during early ventricular arrhythmias in acute regional myocardial ischemia in isolated porcine and canine hearts**. *Circ. Res.* 1980, **47**(2):151–165.

[49] Stinstra JG, Shome S, Hopenfeld B, MacLeod RS: **Modelling passive cardiac conductivity during ischaemia.** *Med Biol Eng Comput* 2005, **43**(6):776–782.

[50] Hopenfeld B, Stinstra JG, Macleod RS: **Mechanism for ST depression associated with contiguous subendocardial ischemia.** *J Cardiovasc Electrophysiol* 2004, **15**(10):1200–1206.

[51] Aras K, Swenson D, MacLeod R: **The Origin of Myocardial Ischemia is Not Limited to the Sub-endocardium**. In *International Society for Computerized Electrocardiology (ISCE)* 2011.

[52] Fletcher G, Flipse T, Kligfield P, Malouf J: **Current status of ECG stress testing.** *Curr Probl Cardiol* 1998, **23**(7):353–423.

[53] Stern S: **State of the art in stress testing and ischaemia monitoring.** *Card Electrophysiol Rev* 2002, **6**(3):204–208.

[54] Hopenfeld B, Stinstra JG, MacLeod RS: **The effect of conductivity on ST-segment epicardial potentials arising from subendocardial ischemia.** *Ann Biomed Eng* 2005, **33**(6):751–763.

[55] Johnston PR, Kilpatrick D: **The effect of conductivity values on ST segment shift in subendocardial ischaemia.** *IEEE Trans Biomed Eng* 2003, **50**(2):150–158.

[56] Kilpatrick D, Johnston PR, Li DS: **Mechanisms of ST change in partial thickness ischemia.** *J Electrocardiol* 2003, **36 Suppl**:7–12.

[57] Potse M, Vinet A, LeBlanc AR, Diodati JG, Nadeau R: **Understanding ST depression in the stress-test ECG.** *Anadolu Kardiyol Derg* 2007, **7 Suppl 1**:145–147.

[58] Viles-Gonzalez JF, Fuster V, Badimon JJ: **Atherothrombosis: a widespread disease with unpredictable and life-threatening consequences**. *Eur Heart J* 2004, **25**(14):1197–207.

[59] Gibler WB, Cannon CP, Blomkalns AL, Char DM, Drew BJ, Hollander JE, Jaffe AS, Jesse RL, Newby LK, Ohman EM, Peterson ED, Pollack CV, American Heart Association Council on Clinical Cardiology, American Heart Association Council on Cardiovascular Nursing, Quality of Care and Outcomes Research Interdisciplinary Working Group, Society of Chest Pain Centers: **Practical implementation of the Guidelines for Unstable Angina/Non-ST-Segment Elevation Myocardial Infarction in the emergency department**. *Ann Emerg Med* 2005, **46**(2):185–97.

[60] Edmunds J, Gibbons R, Breshahan J, Clements I: **Significance of anterior ST depression in inferior wall acute myocardial infarction**. *Am. J. Cardiol.* 1994, **73**:143–148.

[61] Irvine LA, Jafri MS, Winslow RL: **Cardiac sodium channel Markov model with temperature dependence and recovery from inactivation**. *Biophys J* 1999, **76**(4):1868–85.

[62] Hodgkin AL, Huxley AF: **A quantitative description of membrane current and its application to conduction and excitation in nerve.** *J Physiol* 1952, **117**(4):500–544.

[63] Ten Tusscher K, Noble D, Noble P, Panfilov A: **A model for human ventricular tissue**. *American Journal of Physiology-Heart and Circulatory Physiology* 2004, **286**(4):H1573–H1589.

[64] Luo C, Rudy Y: **A dynamic model of the cardiac ventricular action potential. I. Simulations of ionic currents and concentration changes**. *Circulation research* 1994, **74**(6):1071–1096.

[65] Faber G, Rudy Y: **Action potential and contractility changes in [Na+] i overloaded cardiac myocytes: a simulation study**. *Biophysical Journal* 2000, **78**(5):2392–2404.

[66] Adler CP, Costabel U: **Cell number in human heart in atrophy, hypertrophy, and under the influence of cytostatics**. *Recent Adv Stud Cardiac Struct Metab* 1975, **6**:343–55.

[67] Leon L, Roberge F: **Structural complexity effects on transverse propagation in a two-dimensional model of myocardium.** *IEEE Trans Biomed. Eng.* 1991, **38**(10):997–1009.

[68] Lesh M, Pring M, Spear J: **Cellular uncoupling can unmask dispersion of action potential duration in ventricular myocardium. A computer modeling study.** *Circ. Res.* 1989, **65**(5):1426–1440.

[69] Roth BJ: **How the anisotropy of the intracellular and extracellular conductivities influences stimulation of cardiac muscle.** *J Math Biol* 1992, **30**(6):633–646.

[70] Brenner S, Scott L: *The mathematical theory of finite element methods, Volume 15.* Springer Verlag 2008.

[71] Henriquez CS: **Simulating the electrical behavior of cardiac tissue using the bidomain model.** *Crit Rev Biomed Eng* 1993, **21**:1–77.

[72] Saad Y: *Iterative methods for sparse linear systems*. Philadelphia: SIAM, 2nd ed edition 2003, [`http://www.loc.gov/catdir/enhancements/fy0665/2002044644-d.html`].

[73] Johnson C, MacLeod R, Parker S, Weinstein D: **Biomedical Computing and Visualization Software Environments**. *Comm. ACM* 2004, **47**(11):64–71, [`http://www.sci.utah.edu/publications/crj04/ACM-Nov04.pdf`].

[74] Potse M, Dubé B, Richer J, Vinet A, Gulrajani RM: **A comparison of monodomain and bidomain reaction-diffusion models for action potential propagation in the human heart**. *IEEE Trans Biomed Eng* 2006, **53**(12 Pt 1):2425–35.

[75] Vigmond EJ, Aguel F, Trayanova NA: **Computational techniques for solving the bidomain equations in three dimensions**. *IEEE Trans Biomed Eng* 2002, **49**(11):1260–9.

[76] Rudy Y, Messinger-Rapport B: **The Inverse Solution in Electrocardiography: Solutions in Terms of Epicardial Potentials**. *Crit. Rev. Biomed. Eng.* 1988, **16**:215–268.

[77] Pullan A, LKCheng, Nash M, Brooks D, Ghodrati A, MacLeod R: **The Inverse Problem of Electrocardiography**. In *Comprehensive Electrocardiology*. Edited by Macfarlane P, van Oosterom A, Pahlm O, Kligfield P, Janse M, Camm J, Springer Verlag 2010.

[78] Keane AJ, Nair PB: *Computational approaches for aerospace design: the pursuit of excellence*. Chichester, England: Wiley 2005, [`http://www.loc.gov/catdir/enhancements/fy0624/2005044335-d.html`].

[79] Donner LJ, Schubert WH, Somerville R: *The development of atmospheric general circulation models: complexity, synthesis, and computation*. Cambridge: Cambridge University Press 2011, [`http://www.loc.gov/catdir/enhancements/fy1116/2010037289-b.html`].

[80] Babuska I, Banerjee U, Osborn J: **Generalized finite element methods: main ideas, results, and perspective**. Tech. rep., DTIC Document 2004.

[81] Cohen E, Riesenfeld R, Elber G: *Geometric modeling with splines: an introduction, Volume 1*. AK Peters Wellesley, MA 2001.

[82] Prince J, Links J: *Medical imaging signals and systems*. Pearson Prentice Hall 2006.

[83] Van Leemput K, Maes F, Vandermeulen D, Suetens P: **A unifying framework for partial volume segmentation of brain MR images**. *Medical Imaging, IEEE Transactions on* 2003, **22**:105–119.

[84] Shellock F, Kanal E: **Safety of magnetic resonance imaging contrast agents**. *Journal of Magnetic Resonance Imaging* 1999, **10**(3):477–484.

[85] Adluru G, Hsu E, Di Bella E: **Constrained reconstruction of sparse cardiac MR DTI data**. *Functional Imaging and Modeling of the Heart* 2007, :91–99.

[86] Pflugfelder P: **Magnetic Resonance Imaging of the Cardiovascular System: Potential Applications**. *Medicine North America* 1990, :410–418.

[87] Gonzalez R, Richard E: **Woods, digital image processing** 2002.

[88] Weickert J: *Anisotropic diffusion in image processing, Volume 1*. Teubner Stuttgart 1998.

[89] Aljabar P, Heckemann R, Hammers A, Hajnal J, Rueckert D: **Multi-atlas based segmentation of brain images: Atlas selection and its effect on accuracy**. *Neuroimage* 2009, **46**(3):726–738.

[90] Lorenzo-Valdes M, Sanchez-Ortiz G, Mohiaddin R, Rueckert D: **Atlas-based segmentation and tracking of 3D cardiac MR images using non-rigid registration**. *Medical Image Computing and Computer-Assisted InterventionMICCAI 2002* 2002, :642–650.

[91] Fischl B, Salat D, Busa E, Albert M, Dieterich M, Haselgrove C, Van Der Kouwe A, Killiany R, Kennedy D, Klaveness S, et al.: **Whole brain segmentation: automated labeling of neuroanatomical structures in the human brain**. *Neuron* 2002, **33**(3):341–355.

[92] Heckemann R, Hajnal J, Aljabar P, Rueckert D, Hammers A: **Automatic anatomical brain MRI segmentation combining label propagation and decision fusion**. *NeuroImage* 2006, **33**:115–126.

[93] Khan A, Wang L, Beg M: **FreeSurfer-initiated fully-automated subcortical brain segmentation in MRI using large deformation diffeomorphic metric mapping**. *NeuroImage* 2008, **41**(3):735–746.

[94] Beucher S, Meyer F: **The morphological approach to segmentation: the watershed transformation**. *OPTICAL ENGINEERING-NEW YORK-MARCEL DEKKER INCORPORATED-* 1992, **34**:433–433.

[95] Haralick R, Shapiro L: **Image segmentation techniques**. *Computer vision, graphics, and image processing* 1985, **29**:100–132.

[96] Galer M, Andrews P: *Photoshop CS5: Essential Skills*. Focal Press 2010.

[97] Shpun S, Gepstein L, Hayam G, Ben-Haim S: **Guidance of radiofrequency endocardial ablation with real-time three-dimensional magnetic navigation system**. *Circulation* 1997, **96**(6):2016–2021.

[98] Worley S: **Use of a Real-Time Three-Dimensional Magnetic Navigation System for Radiofrequency Ablation of Accessory Pathways**. *Pacing and clinical electrophysiology* 1998, **21**(8):1636–1645.

[99] Blood E: **Three dimensional digitizer with electromagnetic coupling** 1986. [US Patent 4,613,866].

[100] Marinaccio P, Nappi B, Captain K, Lane A: **Contact digitizer, particularly for dental applications** 1992. [US Patent 5,131,844].

[101] Haber E, Modersitzki J: **Numerical Methods for Image Registration**. *Inverse Problems* 2004.

[102] El-Sherif N, Caref E, Yin H, Restivo M: **The Electrophysiological Mechanism of Ventricular Arrhythmias in the Long QT Syndrome: Tridimensional Mapping of Activation and Recovery Patterns**. *Circ. Res.* 1996, **79**(3):474.

[103] Rogers J, Melnick S, Huang J: **Fiberglass needle electrodes for transmural cardiac mapping**. *IEEE Trans Biomed. Eng.* 2002, **49**(12):1639–1641.

[104] Zitova B, Flusser J: **Image registration methods: a survey**. *Image and vision computing* 2003, **21**(11):977–1000.

[105] Gower J: **Generalized procrustes analysis**. *Psychometrika* 1975, **40**:33–51.

[106] Crum W, Hartkens T, Hill D: **Non-rigid image registration: theory and practice**. *British journal of radiology* 2004, **77**(suppl 2):S140–S153.

[107] Reitinger B, Bornik A, Beichel R: **Constructing smooth non-manifold meshes of multi-labeled volumetric datasets**. *WSCG (Full Papers)* 2005, :227–234.

[108] Canann S, Tristano J, Staten M, et al.: **An approach to combined Laplacian and optimization-based smoothing for triangular, quadrilateral, and quad-dominant meshes**. In *7th International Meshing Roundtable*, Citeseer 1998:479–494.

[109] Freitag L: **On combining Laplacian and optimization-based mesh smoothing techniques**. *ASME APPLIED MECHANICS DIVISION-PUBLICATIONS-AMD* 1997, **220**:37–44.

[110] Williams J, Rossignac J: **Tightening: curvature-limiting morphological simplification**. In *Proceedings of the 2005 ACM symposium on Solid and physical modeling*, ACM 2005:107–112.

[111] Besl P, Jain R: **Segmentation through variable-order surface fitting**. *Pattern Analysis and Machine Intelligence, IEEE Transactions on* 1988, **10**(2):167–192.

[112] Knupp P: **Algebraic mesh quality metrics for unstructured initial meshes**. *Finite Elements in Analysis and Design* 2003, **39**(3):217–241.

[113] Cheng SW, Dey TK, Ramos EA, Ray T: **Quality meshing for polyhedra with small angles**. *Int. J. Comput. Geometry Appl.* 2005, **15**(4):421–461.

[114] Shewchuk JR: **Tetrahedral Mesh Generation by Delaunay Refinement**. In *Proceedings of the 14th Symposium on Computational Geometry* 1998:86–95.

[115] Meyer MD, Whitaker RT, Kirby RM, Ledergerber C, Pfister H: **Particle-based Sampling and Meshing of Surfaces in Multimaterial Volumes**. *IEEE Transactions on Visualization and Computer Graphics* 2008, **14**(6):1539–1546.

[116] Alliez P, Cohen-Steiner D, Yvinec M, Desbrun M: **Variational tetrahedral meshing**. *ACM Transactions on Graphics* 2005, **24**(3):617–625.

[117] Labelle F, Shewchuk JR: **Isosurface stuffing: fast tetrahedral meshes with good dihedral angles**. *ACM Trans. Graph.* 2007, **26**:1–10.

[118] Callahan M, Cole M, Shepherd J, Stinstra J, Johnson C: **BioMesh3D: A Meshing Pipeline for Biomedical Models**. SCI Institute Technical Report UUSCI-2007-009, University of Utah 2007, [`http://www.sci.utah.edu/publications/SCITechReports/UUSCI-2007-009.pdf`].

[119] Teng S, Wong C: **Unstructured mesh generation: Theory, practice, and perspectives**. *International Journal of Computational Geometry and Applications* 2000, **10**(3):227–266.

[120] Owen S: **A survey of unstructured mesh generation technology**. In *7th International Meshing Roundtable*, no. 6 in 3, Citeseer 1998.

[121] Si H, Gärtner K: **Meshing piecewise linear complexes by constrained Delaunay tetrahedralizations**. In *Proceedings of the 14th international meshing roundtable*, Springer 2005:147–163.

[122] Rajan V: **Optimality of the Delaunay triangulation in d**. *Discrete & Computational Geometry* 1994, **12**:189–202.

[123] Zhang Y, Hughes T, Bajaj C: **Automatic 3d mesh generation for a domain with multiple materials**. In *Proceedings of the 16th international meshing roundtable*, Springer 2008:367–386.

[124] Lau H, Ruys A, Carter P, Wang X, Li Q: **Subject Specific Modelling of Electrical Conduction in the Body: a Case Study**. *Journal of Biomimetics, Biomaterials, and Tissue Engineering* 2011, **10**:43–53.

[125] Shephard MS, Georges MK: **Automatic three-dimensional mesh generation by the finite octree technique**. *International Journal for Numerical Methods in Engineering* 1991, **32**(4):709–749, [`http://dx.doi.org/10.1002/nme.1620320406`].

[126] Yerry M, Shephard M: **Automatic three-dimensional mesh generation by the modified-octree technique**. *International Journal for Numerical Methods in Engineering* 1984, **20**(11):1965–1990.

[127] Borden M, Shepherd J, Benzley S: **Mesh cutting: Fitting simple all-hexahedral meshes to complex geometries**. In *Proceedings of the 8th International Socity of Grid Generation conference* 2002.

[128] Shepherd J, Tuttle C, Silva C, Zhang Y: **Quality improvement and feature capture in hexahedral meshes**. Tech. rep., Citeseer 2006.

[129] Mitchell S, Tautges T: **Pillowing doublets: refining a mesh to ensure that faces share at most one edge**. In *4th International Meshing Roundtable*, Citeseer 1995:231–240.

[130] Guccione JM, Costa KD, McCulloch AD: **Finite element stress analysis of left ventricular mechanics in the beating dog heart**. *J. Biomechanics* 1995, **28**(10):1167–1177.

[131] Costa KD, Hunter PJ, Wayne JS, Waldmann LK, Guccione JM, McCulloch AD: **A Three-Dimensional Finite Element Method for Large Elastic Deformations of Ventricular Myocardium: II - Prolate Spheroidal Coordinates**. *J. Biomedical Engineering* 1996, **118**(4):464–472.

[132] Henriquez C: **Simulating the electrical behavior of cardiac tissue using the bidomain model**. *Crit. Rev. Biomed. Eng.* 1993, **21**:1–77.

[133] Savage R, Wagner G, Ideker R, Podolsky S, Hackel D: **Correlation of Postmortem Anatomic Findings with Electrocardiographic Changes in Patients with Myocardial Infarction**. *Circ.* 1977, **5**:279–285.

[134] Johnson TA, Engle CL, Boyd LM, Koch GG, Gwinn M, Gettes LS: **Magnitude and time course of extracellular potassium inhomogeneities during acute ischemia in pigs. Effect of verapamil.** *Circulation* 1991, **83**(2):622–634.

[135] Jiang Y, Guccione JM, Ratcliffe MB, Hsu EW: **Transmural heterogeneity of diffusion anisotropy in the sheep myocardium characterized by MR diffusion tensor imaging**. *Am J Physiol Heart Circ Physiol* 2007, **293**(4):H2377–84.

[136] Institute S: 2011. [SCIRun: A Scientific Computing Problem Solving Environment, Scientific Computing and Imaging Institute (SCI), Download from: http://www.scirun.org].

[137] Taubin G: **A signal processing approach to fair surface design.** *Conf Proc SIGGRAPH* 1995, :351–158.

[138] Scientific Computing and Imaging Institute (SCI): **BioMesh3D: Quality Mesh Generator for Biomedical Applications**. *http://www.biomesh3d.org.*

[139] Si H: **TetGen: A Quality Tetrahedral Mesh Generator and Three-Dimensional Delaunay Triangulator**. *http://tetgen.berlios.de/.*

[140] Fozzard H, DasGupta D: **ST-Segment Potentials and Mapping: Theory and Experiments**. *Circ.* 1976, **54**:533–537.

[141] Swenson D, Stinstra J, Burton B, Aras K, MacLeod R: **Wave Equation Based Interpolation on Volumetric Cardiac Electrical Potentials**. In *Computers in Cardiology 2009*. Edited by Murray A 2009:217–220.

[142] Sachse FB, Cole MJ, Stinstra JG: **A software framework for solving bioelectrical field problems based on finite elements.** *Conf Proc IEEE Eng Med Biol Soc* 2006, **1**:2554–2557.

[143] Ni Q, MacLeod R, Lux R, Taccardi B: **Interpolation of cardiac electric potentials**. *Annal. Biomed. Eng.* 1997, **25**(Suppl):61. [Biomed. Eng. Soc. Annual Fall Meeting].

[144] Merx W, Yoon M, Han J: **The role of local disparity in conduction and recovery time on ventricular vulnerability to fibrillation**. *Am. Heart J.* 1977, **94**(5):603–610.

[145] Witkowski F, Leon L, Penkoske P, Giles W, Spano M, Ditto W, Winfree A: **Spatiotemporal evolution of ventricular fibrillation.** *Nature* 1998, **392**(6671):78–82.

[146] Swenson D, Levine J, Tate J, Whitaker R, MacLeod R: **Impacts of Boundary Conforming Meshes on Electrical Cardiac Simulation**. In *Proceedings of the 21st International Meshing Roundtable*. Edited by Jiao X, Weill JC, Springer Berlin Heidelberg 2013:585–602, [`http://dx.doi.org/10.1007/978-3-642-33573-0_34`].

[147] Wilensky RL, Tranum-Jensen J, Coronel R, Wilde AA, Fiolet JW, Janse MJ: **The subendocardial border zone during acute ischemia of the rabbit heart: an electrophysiologic, metabolic, and morphologic correlative study.** *Circulation* 1986, **74**(5):1137–1146.

[148] Janse MJ, Cinca J, Morena H, Fiolet JW, Kleber AG, de Vries GP, Becker AE, Durrer D: **The "border zone" in myocardial ischemia. An electrophysiological, metabolic, and histochemical correlation in the pig heart.** *Circ Res* 1979, **44**(4):576–588.

[149] Coronel R, Wilms-Schopman FJ, Fiolet JW, Opthof T, Janse MJ: **The relation between extracellular potassium concentration and pH in the border zone during regional ischemia in isolated porcine hearts.** *J Mol Cell Cardiol* 1995, **27**(9):2069–2073.

[150] Ursell PC, Gardner PI, Albala A, Fenoglio JJJ, Wit AL: **Structural and electrophysiological changes in the epicardial border zone of canine myocardial infarcts during infarct healing.** *Circ Res* 1985, **56**(3):436–451.

[151] de Bakker J, van Capelle F, Janse M, van Hemel N, Hauer R, Defauw J, Vermeulen F, de Wekker PB: **Macroreentry in the infarcted human heart: the mechanism of ventricular tachycardias with a "focal" activation pattern**. *J. Am. Coll. Cardiol.* 1991, **18**(4):1005–1014.

[152] Barr R, Ramsey M, Spach M: **Relating Epicardial to Body Surface Potential Distributions by Means of Transfer Coefficients Based on Geometry Measurements**. *IEEE Trans Biomed. Eng.* 1977, **24**:1–11.

[153] Nielsen B, Cai X, Lysaker M: **On the possibility for computing the transmembrane potential in the heart with a one shot method: An inverse problem**. *Mathematical Biosciences* 2007, **210**(2):523–553.

[154] MacLachlan M, Sundnes J, Lines G: **Simulation of ST Segment Changes During Subendocardial Ischemia Using a Realistic 3-D Cardiac Geometry**. *IEEE Trans Biomed. Eng.* 2005, **52**(5):799–807.

[155] Wang Y, Cuculich P, Zhang J, Desouza K, Vijayakumar R, Chen J, Faddis M, Lindsay B, Smith T, Rudy Y: **Noninvasive electroanatomic mapping of human ventricular arrhythmias with electrocardiographic imaging.** *Sci Transl Med* 2011, **3**(98):98ra84.

[156] Triedman J, Jolley M, Stinstra J, Brooks D, MacLeod R: **Predictive modeling of defibrillation using hexahedral and tetrahedral finite element models: recent advances**. *J. Electrocardiol.* 2008, **41**(6):483–486.

[157] Jolley M, Stinstra J, Tate J, Pieper S, Macleod R, Chu L, Wang P, Triedman J: **Finite element modeling of subcutaneous implantable defibrillator electrodes in an adult torso.** *Heart Rhythm. J.* 2010, **7**(5):692–698.

[158] Pfeifer B, Fischer G, Hanser F, Seger M, Hintermuller C, Modre-Osprian R, Trieb T, Tilg B: **Atrial and ventricular myocardium extraction using model-based techniques.** *Methods Inf Med* 2006, **45**:19–26.

[159] Cuculich P, Wang Y, Lindsay B, Faddis M, Schuessler R, RJ JD, Li L, Rudy Y: **Noninvasive characterization of epicardial activation in humans with diverse atrial fibrillation patterns.** *Circ.* 2010, **122**(14):1364–1372.

[160] Swenson D, Stinstra J, Burton B, Aras K, MacLeod R: **The effect of finite element mesh quality on electrical bidomain simulations**. In *Computers in Cardiology 2010.* Edited by Murray A 2010:(in press).

[161] Jolley M, Stinstra J, Pieper S, MacLeod R, Brooks D, Cecchin F, Triedman J: **A Computer Modeling Tool for Comparing Novel ICD Electrode Orientations in Children and Adults**. *Heart Rhythm. J.* 2008, **5**(4):565–572.

[162] MacLeod R, Shome S, Stinstra J, Punske B, Hopenfeld B: **Mechanisms of Ischemia-Induced ST-Segment Changes**. *J. Electrocardiol.* 2005, **38**:8–13.

[163] Johnston P, Kilpatrick D: **The effect of conductivity values on ST segment shift in subendocardial ischaemia**. *IEEE Trans Biomed. Eng.* 2003, **50**(2):150–158.

[164] Rudy Y, Ackerman M, Bers D, Clancy C, Houser S, London B, McCulloch A, Przywara D, Rasmusson R, Solaro R, Trayanova N, Wagoner DV, Varro A, Weiss J, Lathrop D: **Systems approach to understanding electromechanical activity in the human heart: a national heart, lung, and blood institute workshop summary.** *Circ.* 2008, **118**(11):1202–1211.

[165] Boissonnat JD, Oudot S: **Provably good sampling and meshing of surfaces**. *Graphical Models* 2005, **67**(5):405–451.

[166] Cheng SW, Dey TK, Ramos EA, Ray T: **Sampling and meshing a surface with guaranteed topology and geometry**. *SIAM J. Comput.* 2007, **37**(4):1199–1227.

[167] Cheng SW, Dey TK, Levine JA: **A practical Delaunay meshing algorithm for a large class of domains**. In *Proceedings of the 16th International Meshing Roundtable* 2007:477–494.

[168] Venditti DA, Darmofal DL: **Anisotropic grid adaptation for functional outputs: application to two-dimensional viscous flows**. *Journal of Computational Physics* 2003, **187**:22 – 46.

[169] Johnson C, MacLeod R, Ershler P: **A Computer Model for the Study of Electrical Current Flow in the Human Thorax**. *Computers in Biology and Medicine* 1992, **22**(3):305–323.

[170] Ideker RE, Wolf PD, Alferness C, Krassowska W, Smith WM: **Current concepts for selecting the location, size and shape of defibrillation electrodes**. *Pacing Clin Electrophysiol* 1991, **14**(2 Pt 1):227–40.

[171] Swenson D, Stinstra J, Burton B, Aras K, Healy L, , MacLeod R: **Evaluating the Effects of Border Zone Approximations with Subject Specific Ischemia Models**. In *World Congress on Med. Phys. and Biomed. Eng., Volume 25/IV.* Edited by Doessel O, Schlegel WC, Heidelberg: Springer 2009:1680–1683.

[172] Bordas R, Carpentieri B, Fotia G, Maggio F, Nobes R, Pitt-Francis J, Southern J: **Simulation of cardiac electrophysiology on next-generation high-performance computers**. *Philos Transact A Math Phys Eng Sci* 2009, **367**(1895):1951–69.

[173] Lloyd C, Hunter P, Nielsen P: **The CellML Model Repository**. *Bioinformatics* 2008, **24**(18):2122–2123.

[174] Sosa E, Scanavacca M, D'Avila A, Oliviera F, Ramires J: **Nonsurgical transthoracic Epicardial Ablation to Treat Recurrent of Ventricular Tachycardia**. *J. Am. Coll. Cardiol.* 2000, **35**:1442–1449.

[175] Jeong WK, Whitaker R: **A Fast Iterative Method For Eikonal Equations**. *SIAM J. Scientific Computing* 2009, **30**(5):2512–2534.

[176] Butson CR, Tamm G, Jain S, Fogal T, Kruger J: **Evaluation of Interactive Visualization on Mobile Computing Platforms for Selection of Deep Brain Stimulation Parameters**. *IEEE Trans Vis Comput Graph* 2012.

[177] Vadakkumpadan F, Arevalo H, Ceritoglu C, Miller M, Trayanova N: **Image-based estimation of ventricular fiber orientations for personalized modeling of cardiac electrophysiology.** *IEEE Trans. Med. Imag.* 2012, **31**(5):1051–1060.

[178] Latacha M, Memon N, Cuculich P, Hertel J, Wang Y, Rudy Y, Smith T: **Pathologic examination after epicardial ablation of ventricular tachycardia in cardiac sarcoidosis.** *Heart Rhythm. J.* 2010, **7**(5):705–707.

[179] Jolley M, Stinstra J, Tate J, MacLeod R, Triedman J, Wang P, Pieper S: **Modeling of Optimal Subcutanous ICD Lead Placement in Mixed Transvenous-Subcutaneous Systems,**. In *Proceedings of Heart Rhythm Society* 2012.

[180] Nielsen P, Grice IL, Smaill B, Hunter P: **Mathematical Model of geometry and fibrous structure of the heart**. *Am. J. Physiol.* 1991, **260**:H1365–H1378.

[181] Rodriguez B, Li L, Eason J, Efimov I, Trayanova N: **Differences between left and right ventricular chamber geometry affect cardiac vulnerability to electric shocks.** *Circ. Res.* 2005, **97**(2):168–175.

[182] Sachse F, Werner C, Meyer-Waarden K, Dossel O: **Development of a human body model for numerical calculation of electrical fields.** *Comput Med Imaging Graph* 2000, **24**(3):165–171.